Optimization of Harmonically Deforming Thin Airfoils and Membrane Wings for Optimum Thrust and Efficiency

William Paul Walker

Thesis submitted to the Faculty of the
Virginia Polytechnic Institute and State University
in partial fulfillment of the requirements for the degree of

Doctor of Philosophy
in
Aerospace Engineering

Mayuresh J. Patil, Chair
Robert A. Canfield
William J. Devenport
William H. Mason

May 2012
Blacksburg, Virginia

Keywords: Unsteady Aerodynamics, Deformable Airfoils, Membrane Aeroelasticity,
Aeroelastic Tailoring, Optimization

Optimization of Harmonically Deforming Thin Airfoils and Membrane Wings for Optimum Thrust and Efficiency

William Paul Walker

(ABSTRACT)

This dissertation presents both analytical and numerical approaches to optimizing thrust and thrust efficiency of harmonically deforming thin airfoils and membrane wings. A frequency domain unsteady aerodynamic theory for deformable thin airfoils, with Chebychev polynomials as the basis functions is presented. Stroke-averaged thrust and thrust efficiency expressions are presented in a quadratic matrix form. The motion and deformation of the airfoil is optimized for maximum thrust and efficiency. Pareto fronts are generated showing optimum deformation conditions (magnitude and phase) for various reduced frequencies and constraints. It is shown that prescribing the airfoil to deform in a linear combination of basis functions with optimal magnitude and phase results in a larger thrust as compared to rigid plunging, especially at low reduced frequencies. It is further shown that the problem can be constrained significantly such that thrust is due entirely to pressure with no leading edge suction, and associated leading edge separation.

The complete aeroelastic system for a membrane wing is also optimized. The aerodynamic theory for deformable thin airfoils is used as the forcing in a membrane vibration problem. Due to the nature of the two dimensional theory, the membrane vibration problem is reduced to two dimensions via the Galerkin method and nondimensionalized such that the only terms are nondimesional tension, mass ratio and reduced frequency. The maximum thrust for the membrane wing is calculated by optimizing the tension in the membrane so that the the aeroelastic deformation due to wing motion leads to optimal thrust and/or efficiency. A function which describes the optimal variation of spanwise tension along the chord is calculated. It is shown that one can always find a range of membrane tension for which the flexible membrane wings performs better than the rigid wing. These results can be used in preliminary flapping wing MAV design.

Contents

List of Figures

List of Tables

Nomenclature

a_0	rigid body plunging of membrane
a_1	rigid body pitching of membrane
b	semichord
C_T	thrust coefficient
$C(k)$	Theodorsen's function
$F(k)$	real component of Theodorsen's Function
$G(k)$	imaginary component of Theodorsen's function
h_i	real airfoil shape coefficient
$H(k)$	Hankel function
$\left[H_{Tavg}\right]$	thrust Hessian
$\left[H_{Savg}\right]$	structural work Hessian
i	imaginary number
$J(k)$	Bessel function of first kind
K	stiffness matrix
k	reduced frequency
L	lift
M	pitching moment (or mass matrix)
p	pressure
q_x	nondimensional chordwise tension
q_y	nondimensional spanwise tension
S	leading edge suction

s	span length
S_x	chordwise prestress
S_y	spanwise prestress
S_{xy}	shear prestress
t	time
T	total thrust
T_i	Chebychev polynomials
T_P	thrust due to pressure
T_{LES}	thrust due to leading edge suction
T_{avg}	stroke-averaged thrust
T_{osc}	complex thrust amplitude
$\left[T_M\right]$	thrust matrix (complex form)
t_w	wing thickness
u	free stream velocity
W	membrane deformation
w	nondimensional membrane deformation
W_s	work done by structural motion
W_{Savg}	stroke-averaged work done by structural motion
W_T	energy contributing to thrust
W_{Tavg}	stroke-averaged work contributing to thrust
W_w	energy transfered to the wake
X	x location
x	nondimensional x location
y	nondimensional y location
Y	y location
$Y(k)$	Bessel function of second kind
z_i	membrane orthogonal polynomial
Γ	circulation

η	thrust efficiency
λ	Lagrange multiplier
ϕ	velocity potential
ρ_a	air density
ρ_w	wing density
σ	mass ratio
τ	nondimensional time
ω	frequency

Chapter 1

Introduction

1.1 Motivation

Micro Air Vehicles (MAVs) are a growing area of research in recent years. MAVs are a versatile type of aircraft because of small size. Flapping wing MAVs are similar to birds and insects, and are highly maneuverable. The aerodynamics of flapping wing aircraft is highly unsteady. Furthermore, flapping wings undergo high frequency oscillations resulting in significant deformations in addition to the prescribed rigid-body kinematics. Understanding the physics behind the aeroelastic system of flapping wings will help in the design of flapping wing MAVs.

Analytical, frequency-domain, unsteady aerodynamics theory, such as those of Theodorsen[1] and Garrick[2], have proven quite useful in understanding aeroelastic stability and thrust generation, as well as in the preliminary design of maneuverable aircraft. However, Theodorsen and Garrick only modeled thin airfoils undergoing rigid body motion in inviscid flow. Inviscid potential flow theories will not accurately model flows at low Reynolds numbers or flows which have significant viscous effects, but they do help in increasing fundamental understanding of the unsteady aerodynamic flow and aeroelasticity of flapping wing MAVs. Furthermore, potential flow theory can serve as a check for verifying other more complex/computational codes and methods used in design. Extensions of these un-

steady aerodynamic theories to deformable airfoils has been done previously including work by Peters[3, 4] and Walker and Patil[5]. These unsteady deformable thin airfoil theories are helpful in further understanding the unsteady aerodynamics behind flapping wing MAV's.

Flapping wing MAV's, by nature, require powerful and efficient thrust generation from the wings while also maintaining lift. It is advantageous to design the wings on flapping wing MAVs to generate as much thrust as possible, as efficiently as possible. Optimizing the unsteady deformable thin airfoil theory gives conditions where a deforming wing generates maximum thrust and/or efficiency. However, optimizing only the aerodynamic system gives magnitude and phase of deformation shapes required for maximum thrust and efficiency conditions. In realistic systems deformation is not prescribed, but a result of the flapping motion. The stiffness of membrane wings is primarily responsible for the deformation of the wings while undergoing flapping motion. These resulting deformations are not necessarily deformations which would lead to a large thrust or efficiency. Therefore the complete aeroelastic system must be considered to obtain realistic designs.

The aeroelastic system is composed of a membrane vibration model coupled with the aerodynamic forcing from the unsteady deformable thin airfoil theory. Since the deformation is a result of the aerodynamic forcing from flapping and the inertial effects from the mass of the wing, optimizing the aeroelastic system for maximum thrust and/or efficiency requires tailoring the mass and stiffness properties of the wing to lead to deformations that generate maximum thrust and/or efficiency. Aeroelastic tailoring of a flapping membrane wing provides a method for preliminary design of flapping wing MAVs to operate at high thrust and/or efficiency conditions. This will lead to improving the performance of flapping MAVs and will be a very useful tool in MAV design.

1.2 Objectives

The aim of the current research is to develop a practical tool for preliminary MAV design. The focus of the work is on investigating the properties of a flapping membrane wing that

lead to maximum stroke-averaged thrust at high efficiency. Optimization of MAV wings is required to achieve this goal. The optimization problem can be approached from two perspectives: the aerodynamic system and the aeroelastic system. In the aerodynamic system route the stroke-averaged thrust is calculated for a prescribed harmonically deforming airfoil parameterized by the magnitude and phase of the deformation shapes and rigid body motion of the airfoil. Stroke-averaged thrust in the aeroelastic system is a function of the deformations that result from the prescribed rigid body motion, mass, and stiffness. Optimization of the aerodynamic system can give the deformation required to achieve maximum stroke-averaged thrust. Optimization of the aeroelastic system can give the structural properties of the wing required for the wing to deform in such a way as to yield maximum stroke-averaged thrust. Both optimization problems can provide insight into designing a flexible flapping wing for high thrust and efficiency.

In order to design a flapping wing for maximum stroke-averaged thrust at high efficiency, optimization of both the aerodynamic and aeroelastic systems need to be investigated. The aerodynamic system is based on potential flow aerodynamics and therefore cannot model separation. Constrained optimization of the aerodynamic system is required to obtain results within a realistic flow regime. The magnitude of the deformation should be constrained to give results where separation does not occurs on the airfoil. However, in potential flow theory for a thin airfoil, there is a singularity at the leading edge which would result in separation at the leading edge. Therefore a second constraint is needed to avoid leading edge singularity/separation. Maximum thrust and efficiency are of importance in MAV design and so constrained aerodynamic optimization is required for:

- Maximum stroke-averaged thrust
- Maximum thrust efficiency
- Maximum stroke-averaged thrust and thrust efficiency (multi objective)

The pure aerodynamic problem provides useful results for MAV wing design. However the aeroelastic system should also investigated. In general, airfoil/wing deformations

are not prescribed, only the rigid body flapping motion (plunge and pitch) can be prescribed. Therefore the aeroelastic system must be considered to design the wing structure that generates maximum stroke-averaged thrust when flapping. The aeroelastic system consists of the general form of the membrane vibration equation with the pressure from the aerodynamic model as the forcing. The three dimensional membrane vibration problem can be reduced to two dimensions because the aerodynamic theory is only two dimensions. This can be done via the Galerkin method assuming the membrane vibrates in the first mode in the spanwsie direction. The reduced membrane equation can be further reduced to a multi degree of freedom system (MDOF) with the assumed modes method.

Aeroelastic optimization is required for maximum stroke-averaged thrust with the design space consisting of the tensions in the membrane. Optimization can be conducted on a single degree of freedom system to show the physical nature of the problem and conduct parametric studies. A MDOF system needs to be optimized to allow a larger design space where the spanwise tension can vary along the chord. Similar to the aerodynamic system there are limits to the aeroelastic system. The tensions should be constrained to always be positive. Secondly, aeroelastic instabilities should be avoided. Therefore a constraint should be placed on the stiffness to ensure that the aeroelastic system does not encounter aeroelastic divergence.

Chapter 2

Literature Survey

Designing MAV wings capable of producing high thrust and efficiency by flapping requires theory which models the aeroelastic system of flapping membrane wings. Optimization of the aeroelastic system is the procedure by which a good preliminary design can be generated for a MAV wing. This work requires the development of unsteady aerodynamic theories capable of modeling the forcing on a deformable wing, a vibrating membrane model which uses the aerodynamic theory as forcing and optimization techniques to obtain the best solution. Previous work has been conducted by a variety of researchers in all of the aforementioned areas.

2.1 Unsteady Aerodynamics

Unsteady aerodynamic theories have been developed for many years for a variety of uses. The aerodynamics theory developed by Theodorsen[1] is based on potential flow for the lift and pitching moment on a pitching and plunging thin airfoil with a flap. The theory assumes small perturbations and harmonic motion. An analytical solution was obtained which gives the loads on the airfoil in terms of the kinematics and Theodorsen's function. Theodorsen was able to show that reduced frequency was the correct measure of the unsteadiness of the flow because Theodorsen's function is solely a function of reduced frequency.

Garrick[2] extended Theodorsen's theory and derived an expression for the propulsive force on an oscillating thin airfoil. Garrick approached the problem in two different ways; conservation of energy and direct calculation of forces. He used conservation of energy to write the propulsive energy in terms of the structural energy and energy of the wake. The propulsive force was also calculated directly by calculating the leading edge suction on a thin airfoil, based on the work of von Kármán and Burgers[6]. Garrick showed through this solution that harmonic plunging will always lead to a positive propulsive force.

Wagner[7] investigated the lag in the lift generation for an airfoil which is suddenly started from rest. Wagner's function models the effect of the wake on the lift of a thin airfoil starting from rest. Küssner[8] investigated the similar problem of an airfoil entering a gust. Garrick[9] investigated the relationship of Wagner's and Küssner's functions with Theodorsen's function.

The work of Theordorsen[1], Garrick[2], Wagner[7], and Küssner[8] approached specific flow situations. The problem of an airfoil in non-uniform motion was addressed by von Kármán and Sears[10]. This theory derived the formulae for lift and pitching moment for a general non-uniform motion, but in a non-closed form result. Their theory shows the lift and pitching moment each to be a sum of three components, quasi-steady lift, apparent mass, and wake vorticity contribution. The equations for lift and pitching moment were applied to specific flow situations and shown to match theories by Theodorsen, Wagner, and Küssner. Sears later applied Heaviside's operators to obtain more convenient results of this general theory[11].

Isaacs[12] derived a solution for the lift on an airfoil in a non constant free-stream, and investigated in particular the case of a rotary wing aircraft in forward flight[13]. However, Isaacs did not account for the downward motion of the wake. Loewy[14] investigated the problem of a rotary wing in hover. He showed that the expressions for lift and pitching moment are similar to those obtained by Theodorsen. Theodorsen's function was replaced by another function (Loewy's function) which was calculated assuming two dimensional flow on the blades and a layered wake. Greenberg[15] developed an extension to Theodorsen theory

to account for a non-constant free-stream, as Isaacs did. However, Greenberg assumed the wake to be sinusoidal, as with Theodorsen theory. He showed, via a numerical example, that the use of the sinusoidal wake compared well to Isaacs' theory.

There has been investigation into relating these unsteady airloads methods to the aerodynamics of bird and insect wings. Zbikowski[16] obtained a solution for unsteady flow on a pitching and plunging wing taking into account a non-constant free-stream, similar to Greenberg's work. This solution was given in several different forms, including time and frequency domains. The wake length could be expressed as a function of time, allowing for a more general form of the solution to the problem investigated by Wagner. Azuma and Okamoto[17] extended Theodorsen theory to be applicable to corrugated wing shapes (modeled as a set of connected flat plates).This work was applied to dragonfly wings. Patil[18] presented a relation between thrust generation and aeroelastic flutter using energy transfer. He showed that there are three distinct energy transfer modes: (i) a drag producing flutter mode, (ii) a damped thrust producing mode, and (iii) a damped drag producing mode.

Ansari, Zbikowski and Knowles[19] developed an unsteady aerodynamic model for flapping wings in hover, similar to insects. The nonlinear unsteady aerodynamic model is derived with the same method as Theodorsen[1]. The flow around a two dimensional airfoil is modeled as flow around a circle with the Joukowski conformal mapping transformation. The quasi-steady and unsteady components of the flow are derived separately, utilizing the principle of superposition for a complete solution. The model is converted to a quasi-three dimensional model with blade element theory. Separation from both the leading and trailing edges is modeled because insect like flapping flight undergoes very high angles of attack, and so the leading edge vortex separation must be considered. The resulting equations for the aerodynamic forcing are an exact inviscid model but are not closed form requiring a numerical method to solve the equations. Moreover, the forces are broken up into four basic parts: quasi-steady, apparent mass, wake induced and wake components. It was shown that insect flapping flight was the optimum method for propulsion of a MAV designed for indoor use.

Later work by Ansari, Zbikowski and Knowles[20] presents the implementation and validation of the aerodynamic theory developed. The equations for the aerodynamic loads are solved via a numerical time marching simulation because the equations are not closed form. The wing and free moving wake are modeled as point vortices and the evolution of the wake is tracked. The numerical results are validated with flow visualization and experimental data. The flow field was shown to match well with the flow visualization and the aerodynamic forces matched well with the experimental data.

Unsteady aerodynamic theories for deformable wings have been investigated as well. Peters[3] developed an airloads theory for a deformable wing of arbitrary shape with a general form of freestream velocity. The airloads theory allows for an arbitrary airfoil shape in the form of the Chebychev polynomials. The airloads theory is coupled with an inflow model (which accounts for the effect of the wake) to form a complete unsteady aerodynamic model. The inflow model depends on the type of flow considered including 2D[21] and 3D models[22].

An unsteady deformable thin airfoil theory similar to Peters was developed by Walker and Patil[5] based of the work of Theodorsen[1] and Garrick[2]. The lift, pitching moment and stroke-averaged thrust for a two dimensional thin airfoil deforming harmonically in a free stream was presented. The deformation was determined by the Chebychev polynomials. The stroke-averaged thrust is shown in a quadratic matrix form. The results were verified with Peters[3, 4].

An extension to the unsteady aerodynamic theory of von Kármán and Sears[10] was developed by Johnston, Mason and Han[23]. They extended the three lift components identified by von Kármán and Sears (quasi-steady, apparent mass, and wake-induced) to be applicable to deformable airfoils. The deformation was described by two quadratic curves with arbitrary coefficients allowing for the airfoil to take a variety different shapes. The aerodynamic forces are analyzed for deformed airfoils in several configurations.

An unsteady aerodynamics method for deformable airfoils derived using only the velocity singularity points was developed by Mateescu and Abdo[24]. Their theory presents the aerodynamic forces in terms of velocity singularities at the leading edge and ridges, which

are defined as points where the boundary conditions change. Any general deformable shape can be modeled with this theory provided enough linear segments are used. This simple and efficient technique generated results which compared well to Theodorsen[1] for the case of a rigid airfoil and the case of a harmonically oscillating flap.

Work by Glegg and Devenport investigates the problem of unsteady loading on an airfoil with thickness[25]. Their work uses conformal mapping to map any desired airfoil shape, including a flat plate. The forces are calculated with the Blasius theorem. Robert Jones investigated the unsteady aerodynamics of a wing with finite span[26]. Jones' work comprised of correcting the angle of attack for the downwash velocity generated by three dimensional effects. The problem of unsteady aerodynamics of compressible flows was investigated by Hernandes and Soviero[27].

2.2 Aerodynamic Optimization

In order to generate suitable thrust from flapping, the proper combination of magnitude and phase of each deformation shape is required. Walker and Patil[5] showed that the magnitude of each shape and the phase angles between them have a very large contribution to the value of thrust. The same results were shown by Garrick[2] for the case of pitching and plunging only. These results were validated in water tunnel experiments by Anderson et al.[28]. Heathcote and Gursul[29] later found via water tunnel experiments that a peak in thrust occurred at a particular value of phase angle between pitch and plunge. Therefore optimization of the stroke-averaged thrust using the magnitude and phase of the deformation shapes as design variables is required. Several researchers have investigated this type of optimization problem.

Optimization of flapping wings has been investigated by Tuncer and Kaya[30]. Their work involved finding maximum thrust and propulsive efficiency for a single flapping wing. Reynolds average Navier-Stokes (RANS) was used to model the aerodynamics around a NACA0012 airfoil undergoing pitch and plunge motions. Numerical optimization was used to find optimum conditions for thrust and propulsive efficiency. The design variables included

magnitude of pitch and plunge motions and the phase angle between them. No constraints were applied to the problem to restrict the motion. This is because the viscosity, stall and dynamic stall modeled by the RANS aerodynamics constrained the motion such that the problem had an optimum thrust.

Optimization of the trajectory of motion and the airfoil shape was conducted by Lee and Liou[31]. The motion and shape were parameterized such that the shape and trajectory were found which yielded the maximum thrust. RANS was used to model the aerodynamics. The optimization showed that there exists a periodic, but not sinusoidal trajectory which gives optimum thrust, which is larger than the thrust generated by the sinusoidal trajectory.

Later work work by Lee and Liou used a different parameterization scheme which allowed for non-harmonic trajectories, which can be observed in nature[32]. The trajectories considered involved a one degree of freedom motion, which consisted of plunge only, and a three degree of freedom motion, which used pitching and forward and aft motions. It was shown that non-harmonic trajectories can give a larger thrust than harmonic trajectories for the same efficiency. However it was not shown that the maximum propulsive efficiency increased over the harmonic trajectories with sinusoidal motion.

Much previous work uses RANS aerodynamics and other numerical schemes. While there is good use in these, a closed form solution is quite useful. Primarily, the computational cost of CFD problems is very high. By properly restricting the problem to stay within valid regimes of ideal flow, a quick valid solution for optimum thrust and thrust efficiency is possible.

2.3 Aeroelasticity

By nature, flapping wings are deformable, which is why deformable wing aerodynamics is required for optimization. However, in realistic situations these deformations are not prescribed, but due to the aerodynamic forcing. Therefore the complete aeroelastic system must be considered to get realistic optimization results. Aeroelastic analyses of membrane wings

has been done previously.

The effect of the addition of quadratic camber in the form of the second Chebychev polynomial has been investigated by Murua, Palacios and Peiró[33]. The aeroelastic system was an extension to the classical two degree of freedom system to include harmonic camber. Peters unsteady airloads theory was used to model the aerodynamics of the deformable airfoil. Flutter and divergence speeds were determined via typical V-g analysis. It was shown that a one degree of freedom system consisting of camber alone will lead to flutter. Further, the flutter occurs at one reduced frequency and was shown to be due to interaction between the shed wake and the camber motion. Two and three degree of freedom systems consisting of the addition of pitch, plunge, and both were also investigated. It was shown that certain situations occur where the camber leads to flutter at lower velocities than the rigid body case.

Similar work on membrane aeroelasticity was done by Knight, Lucey and Shaw[34]. Their work investigated the membrane aeroelasticity problem as applied to a soft top convertible roof. The aerodynamics for this situation involves flow over the top of the membrane, but a constant pressure with a velocity of zero on the lower surface of the membrane. The leading and trailing edges of the membrane are attached to a rigid plate, which the airflow is moving over. This fundamental difference in modeling will result in a system with no shed wake since no trailing edge exists for a Kutta condition to be applied. The structural motion considered only the vertical deformation. The aerodynamics and structural motion were modeled numerically. The model allowed for an initial slackness to be present in the roof, yielding a no flow deflection due to the weight of the membrane. Results showed that variation of material properties changed the deflection of the membrane in the same flow conditions, however every case tested was stable.

Membrane wing aeroelasticity with nonlinear structural dynamic models has been analyzed by LaBryer and Attar[35]. Their work involved developing numerical techniques for efficiently and correctly solving membrane aeroelasticity problems where the structural dynamics is highly nonlinear. The aeroelasticty of a string was investigated and it was shown

that situations where the structural dynamics is slightly nonlinear compared well with the finite difference solution and was much faster. However cases where the structural dynamics was highly nonlinear exhibited a large amount of subharmonics in the response and the solution method diverged.

An unsteady aerodynamic theory and corresponding aeroelastic analysis of a flexible airfoil was derived and analyzed by Gaunaa[36]. The aerodynamic theory was derived for an airfoil undergoing arbitrary motion. The theory was verified by simplifying the problem to harmonic motion and matching the results with those of Theodorsen[1] and Garrick[2]. It was also shown that the theory was applicable to vertical gust and was also verified with the work of Sears[37]. It was shown that a plunging flexible airfoil sees a decrease in thrust and an increasing in efficiency as the stiffness is decreased. It was also determined that predictions of camberline elasticity on typical fixed wing airplanes and wind turbines show that rigid airfoil theory is adequate for design.

Numerical simulations of three dimensional aeroelasticity of membrane wings was conducted by Lian and Shyy[38]. Their work involved investigating membrane wing aeroelasticity for fixed wing MAVs. The membrane wing studied consisted of chordwise battons which contribute to the stiffness of the wing, however the skin was still made of a flexible material and therefore small vibrations were still occurring. The structural motion was modeled by a finite element solver and the aerodynamics was modeled by a Navier-Stokes solver. The structural and aerodynamic solvers were coupled through the moving boundary technique and time synchronization. This technique involves interpolation/extrapolation of the CFD mesh after the computation of the structural deformation. Rigid body cases were investigated for comparison purposes. It was shown that the membrane wing vibrated even in a steady free stream, which matches experimental results or the same wing. It was also shown that the membrane wing resulted in comparable lift to the rigid body case, however due to the flexibility of the membrane, cases exist where the camber became large enough to slightly increase the lift over the rigid case.

Three dimensional aeroelastic analysis of membrane wings has also been investigated

by Banerjee and Patil[39]. The aerodynamics was modeled using the unsteady vortex lattice method and the structure model solved with the assumed modes method. The aerodynamics was verified with two a dimensional vortex panel method and the doublet lattice method. A wing undergoing harmonic plunging was analyzed at various values of membrane presstress and frequency of oscillation. The case of a wing starting from rest was also investigated. For the case of an airfoil starting from rest it was shown that larger membrane prestress resulted in smaller deformations and therefore smaller lift and drag. For the case of an airfoil undergoing harmonic plunge it was shown that decreasing the membrane prestress increased the deformations and in turn increased the lift and thrust generated by the wing. Furthermore, the flexibility of the wing was shown to have a significant effect on the thrust.

Aeroelasticity of membrane wings in response to gust loading has been investigated. Harmonic oscillation and gust response of a deformable airfoil was investigated by Grishanina and Shklyarchuk[40]. The unsteady aerodynamics was modeled for arbitrary motion using a series of transverse gusts. The unsteady aerodynamic model of gusts developed by Küssner[8] was used. The aeroelastic system was also analyzed where the airfoil deformation shapes from the aerodynamic theory were the modeshapes. Aeroelastic instabilities (divergence and flutter) were determined for an airfoil and an airfoil with an aileron.

Gust response of a chordwise flexible airfoil was also analyzed by Berci, Toropov, Hewson and Gaskell[41]. The wing chordwise flexibility is modeled with an Euler-Bernoulli beam and is coupled with the spanwise flexibility with vertical and torsional springs located on the elastic axis. The aerodynamic loads are modeled with Peters state-space unsteady aerodynamic model[3]. It was shown that the flexible airfoil experiences lower divergence and flutter speeds with respect to the rigid airfoil with the same aerodynamic and structural properties. Furthermore, it was shown that the flexible airfoil resulted in smaller displacement of the vertical spring and larger displacement of the torsional spring. Therefore the chordwise flexible wing exhibits less spanwise displacement and more twist as compared to the chordwise rigid wing.

Experimental and theoretical work on flexible membrane airfoils was investigated by

Greenhalgh, Curtiss and Smith[42]. Multiple membranes were tested at various prestresses as well as membranes with excess length. As excess length increased, the angle of attack when separation occurred decreased. Furthermore depending on the excess length, negative angles of attack can generate positive lift, but flutter was observed in this regime. The theoretical approach presented was shown to be in good agreement with the experimental results.

Several researchers have investigated the viscous aerodynamics of membrane wings. Gulcat studied the thrust generation of a flexible plunging thin airfoil[43]. It was shown that at low Reynolds numbers the viscous forces overcome the leading edge suction forces to generate a net force in the drag direction. However the opposite is true at higher Reynolds numbers. The flexibility of the airfoil was shown to prevent separation because the net angle of attack at the leading edge was decreased due to the deformation caused by the plunging motion. Furthermore, the net propulsive force increased for the flexible airfoil.

Smith and Shyy analyzed the viscous aerodynamics of membrane wings in steady, laminar flow[44]. The aerodynamics was modeled numerically with the Navier-Stokes equations rather than the classical potential based analysis. It was shown that the numerical simulation of the aeroelastic membrane wing problem in a steady flow using the Navier-Stokes equations was significantly different than potential theory at Reynolds numbers near $2x10^3 - 10^4$. Therefore, at low Reynolds number near the MAV flight regime, potential flow solutions may be inadequate.

Numerical simulations of membrane wing aeroelasticity in viscous flows was investigated by Pederzani and Haj-Hariri[45]. Simulations were performed for cases where the leading and trailing edge were fixed and where only the leading edge was fixed. They showed that flexible airfoils are more efficient than rigid airfoils. Furthermore the output power and input power both increased over the rigid airfoil case. The rise in efficiency was shown to be due to the output power increasing more than the input power when chordwise flexibility is added. It was further shown that heavier airfoils are capable of generating more thrust and are more efficient than lighter ones.

Work conducted by Shyy et al. investigates the aerodynamics of airfoils with thickness

at low Reynolds numbers for MAV applications[46]. Airfoils with a flexible upper surface are compared to rigid airfoils. The vortex panel code XFOIL was modified to analyze airfoils where the upper surface is a membrane and the lower surface is rigid. It was shown that in an oscillating free stream the flexible upper surface provided better performance than the rigid profile. Therefore properties of flexible airfoils can be chosen to improve performance over rigid airfoils. Their results were close to the zero thickness membrane analysis done by Shyy ans Smith[47].

2.4 Aeroelastic Optimization

The deformations generated by the aerodynamics and inertial effects resulting from flapping do not necessarily lead to high thrust, if thrust at all. Optimization of the aeroelastic system is required to obtain a suitable design for a MAV wing. Aeroelastic optimization of wings has been investigated previously. Kaya, Tuncer, et al.[48] conducted numerical gradient based optimization of an aeroelastic flapping wing in a biplane configuration. Their work found conditions for maximum thrust with the aerodynamics modeled with RANS. The design variables were also pitch and plunge amplitude and the phase angle between them. Further work by Kaya, Tuncer, et al.[49] using the same optimization techniques and aerodynamics model found conditions for maximum thrust and propulsive efficiency both. Their results were compared with a single flapping airfoil and it was shown that maximum thrust is larger for a biplane configuration.

A psuedo-analytical approach to the aeroelastic optimization problem has been conducted by Stanford and Beran[50]. Their work investigated unsteady aeroelastic phenomena of flow around a nonlinear shell. Derivation of the analytical design derivatives of the aeroelastic system is presented and several studies were performed via numerical gradient based optimization techniques to give results for several cases. The wing was modeled as a flat plate in three dimensions. The structural model was a nonlinear shell model computed via the Lagrangian approach. The wing structure was broken into triangular finite elements.

The aerodynamics is modeled with an unsteady vortex lattice method (UVLM). The model was validated with the results from Heathcote et al.[29]. Three optimization examples were conducted. The first example was a plunging wing propulsion problem. The thickness distribution was tailored to generate a maximum cycle-averaged thrust without out increasing the overall wing mass. The resulting optimal thickness distribution gave a wing shape where the mass was less than the uniform thickness plate, showing that the mass constraint is not active for this case. The second example was minimizing the amplitude of Limit Cycle Oscillation (LCO) without increasing the overall wing mass. It was shown in this optimization the mass constraint becomes active in order to reduce the amplitude of LCO. The third example was optimizing the thickness distribution for passive gust load alleviation. The mass constraint was inactive for this example, however the peak lift seen in one cycle was reduced.

Similar work in optimization with the use of analytic sensitivities was conducted by Maute, Nikbay and Farhat. They present an analytic sensitivity analysis of the aeroelastic problem and apply it the the optimization of three dimensional wings[51]. Maute, Lesoinne and Farhat present the complete aeroelastic optimization methodology of a system with both aerodynamic and structural variables. The aerodynamic loads were modeled using a finite volume approximation of the Euler equations and the structure was modeled by finite elements. Later work by Maute, Nikbay and Farhat extends the work from Maute, Lesoinne and Farhat to nonlinear aeroelastic systems.

Different approaches to the optimization of membrane wings have been conducted by Lian, Shyy and Haftka[52]. Their work presented a shape optimization of a membrane wing for MAVs. The optimization maximized the lift to drag ratio of a rigid fixed wing MAV with battons. The design variables consisted of the vertical location of the membrane at six locations of the wing. While the optimization was done for a rigid wing MAV, it was shown that optimization of a rigid wing shape can improve a flexible wing with the same geometry. The improvement of the flexible wing was attributed to reduced form drag and better pressure distributions on the wing.

Purely numerical approaches to aeroelastic optimization have been conducted. Nikbay,

Öncü and Aysan present a methodology and code for aeroelastic optimization with high-fidelity commercially available software[53]. The aerodynamics was modeled with FLUENT using GAMBIT to generate the CFD mesh. The geometry was modeled with CATIA. Abaqus was used to model the structure. Numerical optimization was conducted for several example systems with various variables and constraints.

Chapter 3

Aerodynamic Theory

The deformable unsteady airloads theory used in this research was developed by Walker and Patil[5]. The theory is based on the earlier theories of Theodorsen[1] and Garrick[2] for harmonic motion of thin airfoils without thickness in an inviscid, incompressible flow. Non harmonic motion is not considered in this theory. The thin airfoil is modeled as flow on a circle mapped to a flat plate via the Joukowski conformal mapping. A boundary condition of no flow through the surface of the airfoil in the mapped domain is enforced. The derivation of the aerodynamic theory is presented in this chapter.

3.1 Mathematical Preliminaries

Consider a thin deformable airfoil undergoing harmonic rigid body motion and deformation as shown in Figure 3.1. The airfoil motion/deformation is defined by a general function $w(x,t)$, where w is the non dimensional position of the airfoil as a function of x, which is the non dimensional chordwise coordinate. The semichord b is used for nondimensionalization. $x = -1$ represents the leading edge, while $x = 1$ represents the trailing edge. The airfoil motion/deformation is written in terms of components corresponding to different motions including plunge, pitch, and different forms of deformation. The Chebychev polynomials, shown in Figure 3.2, were chosen for this research and are

$$\begin{aligned} T_0(x) &= 1 \\ T_1(x) &= x \\ T_{n+1}(x) &= 2xT_n(x) - T_{n-1}(x) \end{aligned} \tag{3.1}$$

and satisfy the orthogonality condition,

$$\int_{-1}^{1} T_n(x)T_m(x)w_C(x)dx = \begin{cases} 0 & n \neq m \\ \pi & n = m = 0 \\ \frac{\pi}{2} & n = m \neq 0 \end{cases} \tag{3.2}$$

where $w_C(x)$ is the weighting function and is

$$w_C(x) = \frac{1}{\sqrt{1-x^2}} \tag{3.3}$$

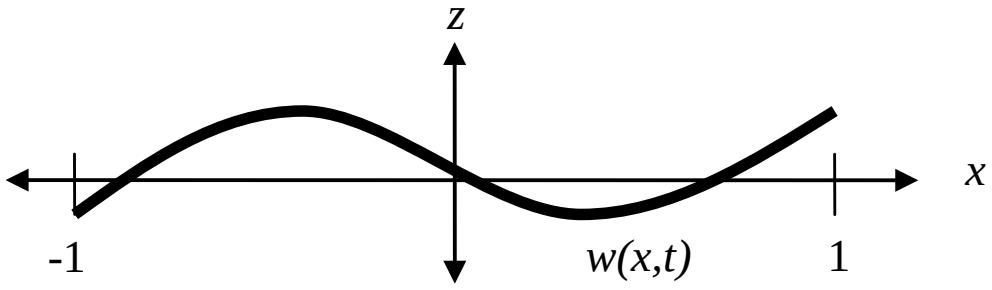

Figure 3.1: Airfoil motion/deformation

The first Chebychev polynomial is a constant, which represents plunge (positive up). The second polynomial is a linear function, which represents angle of attack or pitch (positive nose down). Likewise, the third polynomial is quadratic and represents camber (curved up). The general deformation shape, shown in Figure 3.1, in terms of the Chebychev polynomials

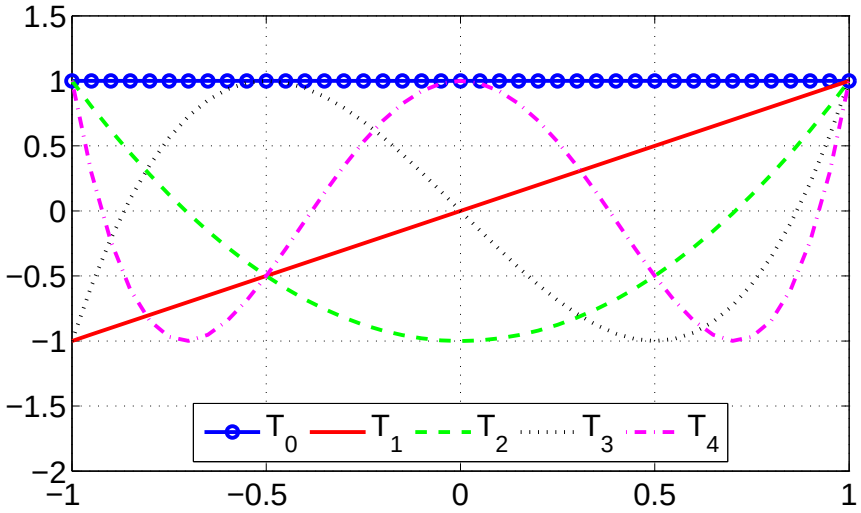

Figure 3.2: Chebychev Polynomials

is

$$w(x,t) = \sum_{n=1}^{\infty} h_n(t) T_n(x) \tag{3.4}$$

The formulation presented can be used with as many polynomials as desired, however the final result for only the first 5 are derived here for compactness.

The Joukowski conformal mapping function is used to map a circle centered at the origin to a flat plate. The mapping function maps all the points outside of the circle to a location outside the flat plate. The points inside the circle are mapped to locations outside the flat plate, but on a different Riemann surface. The points on the circle are mapped directly onto the flat plate[54]. The mapping is

$$x + iw = X + iW + \frac{a^2}{X + iW} \tag{3.5}$$

3.2 Lift and Pitching Moment Derivation

The aerodynamic forces are formulated from flow consisting of two parts, a noncirculatory flow and a circulatory flow. The noncirculatory flow satisfies the no penetration boundary condition. The circulatory flow satisfies the Kutta condition without disturbing the no penetration boundary condition.

3.2.1 Noncirculatory Flow

The no penetration boundary condition is satisfied by a noncirculatory flow consisting of a sheet of sources and sinks. Lets first consider a source of strength 2ϵ at a point (X_1, W_1) and a sink of strength -2ϵ at $(X_1, -W_1)$ in the unmapped plane, which leads to the potential

$$\phi_{source/sink} = \frac{\epsilon}{2\pi} \log \frac{(X - X_1)^2 + (W - W_1)^2}{(X - X_1)^2 + (W + W_1)^2} \tag{3.6}$$

The velocity potential expression becomes only a function of X and X_1 when Eq. 3.6 is restricted to the upper surface of the circle with $W = \sqrt{1 - X^2}$.

$$\phi_{source/sink} = \frac{\epsilon}{2\pi} \log \frac{(X - X_1)^2 + (\sqrt{1 - X^2} - \sqrt{1 - X_1^2})^2}{(X - X_1)^2 + (\sqrt{1 - X^2} + \sqrt{1 - X_1^2})^2} \tag{3.7}$$

Constraining the equation to points only on the circle is helpful because these locations map directly to the airfoil. Therefore Eq. 3.7 is the velocity potential for the source/sink pair on the upper surface of both the circle and the flat plate. The velocity potential for a sheet of source/sink pairs on the flat plate is calculated by applying the Joukowski transformation, Eq. 3.5, and is

$$\phi = \frac{b}{2\pi}\int_{-1}^{1} \epsilon(x,t)\log\frac{(x-x_1)^2+(\sqrt{1^2-x^2}-\sqrt{1^2-x_1^2})^2}{(x-x_1)^2+(\sqrt{1^2-x^2}+\sqrt{1^2-x_1^2})^2}dx_1 \tag{3.8}$$

where, $\epsilon\,(x,t)$, is the strength of the sheet. Note that in the mapped domain, the source/sink sheet is not a circle (with thickness), but a flat plate (zero thickness). This is due to the nature of the Joukowski conformal mapping. Furthermore it should be stated that this flow is not a doublet sheet.

Approaching the surface of the source/sink sheet, the velocity due to the source/sink pair is perpendicular to the surface, and the magnitude is equal to the strength of the source[55]. To preserve the no penetration boundary condition, the velocity generated by the source/sink sheet plus the component of the free stream velocity normal to the airfoil surface must be equal to the local velocity due to motion of the airfoil. Assuming small disturbances, the strength of the source/sink sheet for a generalized airfoil shape is

$$\epsilon(x,t) = u\frac{\partial w}{\partial x} + b\frac{\partial w}{\partial t} \tag{3.9}$$

Substituting the deformation expansion, Eq. 3.4, into the above equation and then substituting the source strength into the equation for the noncirculatory potential, Eq. 3.8, we have

$$\phi_{NC} = \sum_{n=1}^{N}\left(h_n\phi_{h_n} + \dot{h}_n\phi_{\dot{h}_n}\right) \tag{3.10}$$

The expressions for the components of the velocity potential are given in Table 3.1. It can be seen that the velocity potential function s share a similar form with a common term.

The linearized form of Bernoulli's equation gives the pressure difference between the upper and lower surface as

Table 3.1: Velocity potential functions

$\phi_{h_0} = 0$	$\phi_{\dot{h}_0} = -b^2\sqrt{1-x^2}$
$\phi_{h_1} = -ub\sqrt{1-x^2}$	$\phi_{\dot{h}_1} = -\frac{b^2}{2}x\sqrt{1-x^2}$
$\phi_{h_2} = -2ubx\sqrt{1-x^2}$	$\phi_{\dot{h}_2} = \frac{2b^2}{3}\left(1-x^2\right)\sqrt{1-x^2}$
$\phi_{h_3} = -ub(4x^2-1)\sqrt{1-x^2}$	$\phi_{\dot{h}_3} = b^2x(1-x^2)\sqrt{1-x^2}$
$\phi_{h_4} = -4ubx\left(2x^2-1\right)\sqrt{1-x^2}$	$\phi_{\dot{h}_4} = \frac{4b^2}{15}\left(6x^2-1\right)\left(1-x^2\right)\sqrt{1-x^2}$

$$p_L - p_U = 2\rho_a\left(\frac{u}{b}\frac{\partial\phi_U}{\partial x} + \frac{\partial\phi_U}{\partial t}\right) \tag{3.11}$$

The lift (positive up) and pitching moment (positive nose down) about the midchord due to the noncirculatory component of the flow (for the first five shapes) are

$$\begin{aligned} L_{NC} &= b\int_{-1}^{1}(p_L - p_U)dx = -\pi\rho_a b^2\left[u\dot{h}_1 + b\ddot{h}_0 - \frac{b}{2}\ddot{h}_2\right] \\ M_{NC} &= b^2\int_{-1}^{1}(p_L - p_U)xdx = -\pi\rho_a b^2\left[-u^2h_1 + \frac{b^2}{8}\ddot{h}_1 - ub\dot{h}_0 + ub\dot{h}_2 - \frac{b^2}{8}\ddot{h}_3\right] \end{aligned} \tag{3.12}$$

3.2.2 Circulatory Flow

The circulatory flow is developed using a vortex sheet on the body and in the wake. Assuming small disturbances the wake is distributed along the x-axis and moves downstream at the free stream velocity.

Lets consider a pair of point vortices, one outside the circle in the wake at X_0 and the other of opposite strength at the image position inside the circle, $1/X_0$ as shown in Figure 3.3. These vortices represent the shed circulation and the bound circulation; and the locations are chosen to not disturb the no penetration boundary condition. Note that these vortices will map the same location in the mapped plane, but on different Riemann surfaces.

The velocity potential for the vortex pair in the unmapped plane is

$$\phi_{\Gamma_0} = \frac{\Gamma}{2\pi}\left[\tan^{-1}\left(\frac{W}{X - X_0}\right) - \tan^{-1}\left(\frac{W}{X - \frac{1}{X_0}}\right)\right] \tag{3.13}$$

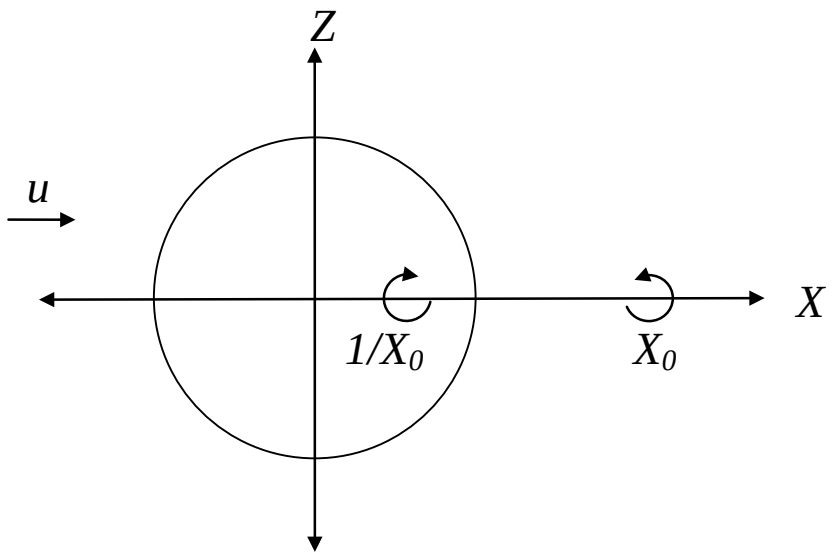

Figure 3.3: Vortex locations

The velocity potential for the vortex pair in the mapped plane is

$$\phi_{\Gamma_0} = -\frac{\Gamma}{2\pi}\tan^{-1}\left[\frac{\sqrt{1-x^2}\sqrt{x_0-1}}{1-xx_0}\right] \tag{3.14}$$

The wake convects with the flow at velocity u, which leads to

$$\frac{\partial x_0}{\partial t} = \frac{u}{b} \tag{3.15}$$

$$\frac{\partial \phi}{\partial t} = \frac{\partial \phi}{\partial x_0}\frac{\partial x_0}{\partial t} = \frac{\partial \phi}{\partial x_0}\frac{u}{b} \tag{3.16}$$

Substituting the above equation into the Bernoulli equation, Eq. 3.11, we have

$$\Delta p_{\Gamma_0} = \frac{2\rho_a u}{b}\left[\frac{\partial \phi}{\partial x} + \frac{\partial \phi}{\partial x_0}\right] \tag{3.17}$$

The pressure difference due to a vortex pair is

$$\Delta p_{\Gamma_0} = -\frac{\rho_a u \Gamma}{\pi b}\left[\frac{x_0 + x}{\sqrt{1-x^2}\sqrt{x_0^2-1}}\right] \tag{3.18}$$

Integrating the pressure difference along the chord gives the lift and pitching moment for the vortex pair as

$$L_{C_0} = -\rho_a u \Gamma \frac{x_0}{\sqrt{x_0^2-1}} \tag{3.19}$$

$$M_{C_0} = \frac{\rho_a u b \Gamma}{2}\left\{\sqrt{\frac{x_0+1}{x_0-1}} - \frac{x_0}{\sqrt{x_0^2-1}}\right\} \tag{3.20}$$

Now lets consider a complete wake. Using $\Gamma = \gamma_w\left(x_0, t\right) b dx_0$, the velocity potential, circulatory lift and pitching moment become

$$\phi_\Gamma = -\frac{b}{2\pi}\int_1^\infty \tan^{-1}\left[\frac{\sqrt{1-x^2}\sqrt{x_0^2-1}}{1-xx_0}\right]\gamma_w\left(x_0, t\right) dx_0 \tag{3.21}$$

$$L_C = -\rho_a u b \int_1^\infty \frac{x_0}{\sqrt{x_0^2 - 1}} \gamma_w \left(x_0, t\right) dx_0 \tag{3.22}$$

$$M_C = \frac{\rho_a u b^2}{2} \int_1^\infty \left\{ \sqrt{\frac{x_0 + 1}{x_0 - 1}} - \frac{x_0}{\sqrt{x_0^2 - 1}} \right\} \gamma_w \left(x_0, t\right) dx_0 \tag{3.23}$$

The magnitude of the circulation, $\gamma_w \left(x_0, t\right)$, is determined by the Kutta condition. This is enforced by ensuring no infinite velocities at the trailing edge, $x = 1$.

$$\frac{\partial}{\partial x} \left(\phi_\Gamma + \sum_{n=0}^{N-1} \left(\phi_{h_n} h_n + \phi_{\dot{h}_n} \dot{h}_n \right) \right)_{x=1} = finite \tag{3.24}$$

The velocity potential expressions for for the first 5 shapes are differentiated and evaluated at $x = 1$ resulting in

$$\frac{1}{2\pi} \int_1^\infty \sqrt{\frac{x_0 + 1}{x_0 - 1}} \gamma_w \left(x_0, t\right) dx_0 = u h_1 + b \dot{h}_0 + 2 b \dot{h}_1 + 2 u h_2 + 3 u h_3 + 4 u h_4 = Q \tag{3.25}$$

The right hand side of Eq. 3.25 is a function of the airfoil motion, denoted as Q[1]. Using this in the load equations (Eq. 3.22 and Eq. 3.23), the circulatory lift and pitching moment are

$$L_C = -2\pi \rho_a u b Q \frac{\int_1^\infty \frac{x_0}{\sqrt{x_0^2 - 1}} \gamma_w \left(x_0, t\right) dx_0}{\int_1^\infty \sqrt{\frac{x_0 + 1}{x_0 - 1}} \gamma_w \left(x_0, t\right) dx_0} \tag{3.26}$$

$$M_C = \pi \rho_a u b^2 Q \left[\frac{\int_1^\infty \frac{x_0}{\sqrt{x_0^2-1}} \gamma_w \left(x_0, t\right) dx_0}{\int_1^\infty \sqrt{\frac{x_0+1}{x_0-1}} \gamma_w \left(x_0, t\right) dx_0} - 1 \right] \tag{3.27}$$

Through this point in the derivation nothing has been assumed about the time dependence of the airfoil motion. Assuming harmonic motion allows for a solution to the ratio of integrals in Eqs. 3.26 and 3.27. The harmonic motion can be represented as given below where $\bar{h}_n$ are complex numbers representing the magnitude and phase of each airfoil motion shape.

$$h_n \left(t\right) = \bar{h}_n e^{i\omega t} \tag{3.28}$$

The wake vortex sheet strength is also oscillatory, and is written in terms of the reduced frequency, $k = \frac{\omega b}{u}$, and the complex magnitude of oscillation of the circulation, $\bar{\gamma}_w$

$$\gamma_w \left(x, t\right) = \bar{\gamma}_w e^{i\omega\left(t - \frac{x}{u}\right)} = \bar{\gamma}_w e^{i(\omega t - kx)} \tag{3.29}$$

The ratio of integrals in the circulatory loading expressions is denoted by C, and was shown by Theodorsen to be purely a function of the reduced frequency, k[1].

$$\begin{aligned} C &= \frac{\int_1^\infty \frac{x_0}{\sqrt{x_0^2-1}} \gamma_w \left(x_0, t\right) dx_0}{\int_1^\infty \sqrt{\frac{x_0+1}{x_0-1}} \gamma_w \left(x_0, t\right) dx_0} = \frac{\bar{\gamma}_w e^{i\omega t} b \int_1^\infty \frac{x_0}{\sqrt{x_0^2-1}} e^{-ikx_0} dx_0}{\bar{\gamma}_w e^{i\omega t} b \int_1^\infty \sqrt{\frac{x_0+1}{x_0-1}} e^{-ikx_0} dx_0} \\ &= \frac{\int_1^\infty \frac{x_0}{\sqrt{x_0^2-1}} e^{-ikx_0} dx_0}{\int_1^\infty \sqrt{\frac{x_0+1}{x_0-1}} e^{-ikx_0} dx_0} = C\left(k\right) \end{aligned} \tag{3.30}$$

This ratio of integrals, known as Theodorsen's function, takes the form of Hankel

functions[54].

$$C(k) = F(k) + iG(k) = \frac{H_1^{(2)}(k)}{H_1^{(2)}(k) + iH_0^{(2)}(k)} \tag{3.31}$$

The Hankel functions in Eq. 3.31 are defined by a complex combination of Bessel functions of the first and second kind.

$$H_n^{(2)}(k) = J_n(k) - iY_n(k) \tag{3.32}$$

Replacing the ratio of integrals with Theodorsen's function, the magnitude and phase of the circulatory lift and pitching moment can be written in the complex form

$$\bar{L}_C = -2\pi\rho_a ub\bar{Q}C(k) \tag{3.33}$$

$$\bar{M}_C = \pi\rho_a ub^2\bar{Q}[C(k) - 1] \tag{3.34}$$

where $\bar{Q}$ is a complex number representing the magnitude and phase of the airfoil motion defined by

$$Q = \bar{Q}e^{i\omega t} \tag{3.35}$$

3.2.3 Complete Lift and Pitching Moment Expressions

The complete lift and pitching moment expressions are given below in Tables 3.2 and 3.3. The tables are broken into three columns representing the lift and pitching moment due to each static shape, the velocity of each shape, and the acceleration of each shape. The lift force components in Table 3.2 show how each airfoil motion/deformation contributes to the lift. Moreover, the lift terms with Theodorsen's function, $C(k)$, are the circulatory components and the moment terms with $C(k) - 1$ are the circulatory components. The static airfoil deformation, the first column of Table 3.2, are only circulatory forces. This is expected because there are no accelerations to contribute to the noncirculatory flow. The plunge location has no effect on the lift. However, the second column shows the plunge velocity contributes to lift in the same form as a static angle of attack because a constant plunge velocity is analogous to a static angle of attack. The pitch velocity contributes a circulatory lift term as well as a noncirculatory lift term. The third column shows that only the plunge and quadratic camber accelerations lead to a lift, and these terms are noncirculatory.

The components of the pitching moment about the midchord in Table 3.3 show similar results as the lift. However, it is more difficult to see the difference between circulatory and noncirculatory terms since the pitching moment terms due to circulation contain $C(k) - 1$. As expected, the pitching moment is zero for static plunge and the plunge velocity resembles the static angle of attack term. These results are verified with Peters' theory[3, 4].

Table 3.2: Lift force components

	$1 * ()$	$ik * ()$	$-k^2 * ()$
$\bar{h}_0$	0	$-2\pi\rho_a ub^2 C(k)$	$-\pi\rho_a b^3$
$\bar{h}_1$	$-2\pi\rho_a bu^2 C(k)$	$-\pi\rho_a ub^2 (C(k)+1)$	0
$\bar{h}_2$	$-4\pi\rho_a bu^2 C(k)$	0	$\frac{1}{2}\pi\rho_a b^3$
$\bar{h}_3$	$-6\pi\rho_a bu^2 C(k)$	0	0
$\bar{h}_4$	$-8\pi\rho_a bu^2 C(k)$	0	0

Table 3.3: Pitching moment components

	$1 * ()$	$ik * ()$	$-k^2 * ()$
$\bar{h}_0$	0	$\pi\rho_a u b^3 C(k)$	0
$\bar{h}_1$	$\pi\rho_a u^2 b^2 C(k)$	$\frac{1}{2}\pi\rho_a u b^3 (C(k)-1)$	$-\frac{1}{8}\pi\rho_a b^4$
$\bar{h}_2$	$2\pi\rho_a u^2 b^2 (C(k)-1)$	$-\pi\rho_a u b^3$	0
$\bar{h}_3$	$3\pi\rho_a u^2 b^2 (C(k)-1)$	0	$\frac{1}{8}\pi\rho_a b^4$
$\bar{h}_4$	$4\pi\rho_a u^2 b^2 (C(k)-1)$	0	0

3.2.4 Complete Pressure Expression

The expression for pressure difference derived from Bernoulli for noncirculatory flow is given as Eq. 3.11. The pressure difference for the circulatory flow due to the vortex pair in Figure 3.3 is given in Eqs. 3.11 and 3.18. The total pressure is the sum of the pressure due to the noncirculatory flow and the circulatory flow for the wake vortex sheet and is

$$p_L - p_U = 2\rho_a \left(\frac{u}{b}\frac{\partial \phi_{U_{NC}}}{\partial x} + \frac{\partial \phi_{U_{NC}}}{\partial t} - \frac{u}{2\pi}\int_1^\infty \frac{x_0 + x}{\sqrt{1-x^2}\sqrt{x_0^2-1}}\gamma_w(x_0,t)\,dx_0 \right) \tag{3.36}$$

where $\phi_{U_{NC}}$ is given by Eq. 3.10. The total pressure can be written in the complex form as

$$\begin{aligned}
\Delta\bar{p}(x,k) = \frac{(x-1)}{15\sqrt{1-x^2}} \big(& 15C(k)(2i\bar{h}_0 k + \bar{h}_1(2+ik) + 4\bar{h}_2 + 6\bar{h}_3 + 8\bar{h}_4) - 30\bar{h}_0 k^2 x \\
& -30\bar{h}_0 k^2 - 15\bar{h}_1 k^2 x^2 - 15\bar{h}_1 k^2 x + 60i\bar{h}_1 kx + 45i\bar{h}_1 k - 20\bar{h}_2 \big(k^2(x-1)(x+1)^2 \\
& -6ikx(x+1) - 6x - 3\big) - 30\bar{h}_3 k^2 x^4 - 30\bar{h}_3 k^2 x^3 + 30\bar{h}_3 k^2 x^2 + 30\bar{h}_3 k^2 x \\
& +240i\bar{h}_3 kx^3 + 240i\bar{h}_3 kx^2 - 60i\bar{h}_3 kx - 60i\bar{h}_3 k + 360\bar{h}_3 x^2 + 360\bar{h}_3 x - 48\bar{h}_4 k^2 x^5 \\
& -48\bar{h}_4 k^2 x^4 + 56\bar{h}_4 k^2 x^3 + 56\bar{h}_4 k^2 x^2 - 8\bar{h}_4 k^2 x - 8\bar{h}_4 k^2 + 480i\bar{h}_4 kx^4 + 480i\bar{h}_4 kx^3 \\
& -240i\bar{h}_4 kx^2 - 240i\bar{h}_4 kx + 960\bar{h}_4 x^3 + 960\bar{h}_4 x^2 - 120\bar{h}_4 \big)
\end{aligned} \tag{3.37}$$

where k is reduced frequency and $C(k)$ is Theodorsen's function.

The magnitude of the pressure can be written in terms of the real and imaginary parts of the h_i's like the thrust and is

$$\begin{aligned}
\Delta\bar{p}(x) =& \frac{\rho_a u^2}{15\sqrt{1-x^2}} \{48ih_{4im}k^2x^6 + 48h_{4re}k^2x^6 + 30ih_{3im}k^2x^5 + 30h_{3re}k^2x^5 \\
&+480h_{4im}kx^5 - 480ih_{4re}kx^5 - 104ih_{4im}k^2x^4 - 104h_{4re}k^2x^4 - 960ih_{4im}x^4 \\
&-960h_{4re}x^4 + 240h_{3im}kx^4 - 240ih_{3re}kx^4 + 15ih_{1im}k^2x^3 + 15h_{1re}k^2x^3 \\
&-60ih_{3im}k^2x^3 - 60h_{3re}k^2x^3 - 360ih_{3im}x^3 - 360h_{3re}x^3 - 720h_{4im}kx^3 \\
&+720ih_{4re}kx^3 + 30h_0k^2x^2 + 64ih_{4im}k^2x^2 + 64h_{4re}k^2x^2 + 960ih_{4im}x^2 \\
&+960h_{4re}x^2 + 60h_{1im}kx^2 - 60ih_{1re}kx^2 - 300h_{3im}kx^2 + 300ih_{3re}kx^2 \\
&-15ih_{1im}k^2x - 15h_{1re}k^2x + 30ih_{3im}k^2x + 30h_{3re}k^2x - 30ih_{1im}x - 30h_{1re}x \\
&+270ih_{3im}x + 270h_{3re}x - 30ih_0kx + 240h_{4im}kx - 240ih_{4re}kx - 30h_0k^2 \\
&-8ih_{4im}k^2 - 8h_{4re}k^2 - 120ih_{4im} - 120h_{4re} - 45h_{1im}k + 45ih_{1re}k + 60h_{3im}k \\
&-60ih_{3re}k + 15(4h_{2im} - 4ih_{2re} + 6h_{3im} - 6ih_{3re} + 8h_{4im} - 8ih_{4re} \\
&+h_{1im}(ik+2) + 2h_0k + h_{1re}(k-2i))(-iF(x-1) + G(x-1) + ix) \\
&+20ih_{2im}\left(-6x^2 - 6ik\left(x^2-1\right)x + k^2\left(x^2-1\right)^2 + 3\right) \\
&+20h_{2re}\left(-6x^2 - 6ik\left(x^2-1\right)x + k^2\left(x^2-1\right)^2 + 3\right)\}
\end{aligned} \tag{3.38}$$

where F and G are components of Theodorsen's function $C(k) = F + iG$.

3.3 Thrust Derivation

The thrust consists of two components, the component of the pressure which acts in the free stream direction and the leading edge suction.

$$T = T_{LES} + T_P \tag{3.39}$$

The component of the thrust due to pressure T_P is the net pressure multiplied by the local slope.

$$T_P = b\int_{-1}^{1}(p_L - p_U)\frac{\partial y}{\partial x}dx = \sum_{n=0}^{N} P_n h_n \tag{3.40}$$

where,

$$P_n = b\int_{-1}^{1}(p_L - p_U)\frac{\partial T_n}{\partial x}dx \tag{3.41}$$

In the complex form, the magnitude and phase of the generalized loads, $\bar{P}_n$, are

$$\begin{aligned}
\bar{P}_0 &= 0 \\
\bar{P}_1 &= L = \pi\rho_a u^2 b\left(-2C(k)\bar{h}_1 - 4C(k)\bar{h}_2 - 6C(k)\bar{h}_3 - 8C(k)\bar{h}_4 - 2ikC(k)\bar{h}_0 - \right. \\
&\quad \left. ik\bar{h}_1 - ikC(k)\bar{h}_1 + k^2\bar{h}_0 - \frac{1}{2}k^2\bar{h}_2\right) \\
\bar{P}_2 &= 4\frac{M}{b} = \pi\rho_a u^2 b\left(4C(k)\bar{h}_1 - 8\bar{h}_2 + 8C(k)\bar{h}_2 - 12\bar{h}_3 + 12C(k)\bar{h}_3 - 16\bar{h}_4 + \right. \\
&\quad \left. 16C(k)\bar{h}_4 + 4ikC(k)\bar{h}_0 - 2ik\bar{h}_1 + 2ikC(k)\bar{h}_1 - 4ik\bar{h}_2 + \frac{1}{2}k^2\bar{h}_1 - \frac{1}{2}k^2\bar{h}_3\right) \\
\bar{P}_3 &= \pi\rho_a u^2 b\left(-6C(k)\bar{h}_1 + 12\bar{h}_2 - 12C(k)\bar{h}_2 - 18C(k)\bar{h}_3 - 24C(k)\bar{h}_4 - 6ikC(k)\bar{h}_0 + \right. \\
&\quad \left. 3ik\bar{h}_1 - 3ikC(k)\bar{h}_1 - 6ik\bar{h}_3 + \frac{1}{2}k^2\bar{h}_2 - \frac{1}{2}k^2\bar{h}_4\right) \\
\bar{P}_4 &= \pi\rho_a u^2 b\left(8C(k)\bar{h}_1 - 16\bar{h}_2 + 16C(k)\bar{h}_2 + 24C(k)\bar{h}_3 - 32\bar{h}_4 + 32C(k)\bar{h}_4 + \right. \\
&\quad \left. 8ikC(k)\bar{h}_0 - 4ik\bar{h}_1 + 4ikC(k)\bar{h}_1 - 8ik\bar{h}_4^- + \frac{1}{2}k^2\bar{h}_3\right)
\end{aligned} \tag{3.42}$$

The thrust due to leading edge suction is

Table 3.4: Leading edge suction velocities

	$1 * ()$	$ik * ()$	$-k^2 * ()$
$\bar{h}_0$	0	$\sqrt{2}bC(k)$	0
$\bar{h}_1$	$\sqrt{2}uC(k)$	$\frac{\sqrt{2}}{2}b\left(C(k)-1\right)$	0
$\bar{h}_2$	$2\sqrt{2}u\left(C(k)-1\right)$	0	0
$\bar{h}_3$	$3\sqrt{2}uC(k)$	0	0
$\bar{h}_4$	$4\sqrt{2}u\left(C(k)-1\right)$	0	0

$$T_{LES} = \pi\rho_a b S^2 \tag{3.43}$$

The leading edge suction (S) comes from the vorticity at the leading edge. Referring to Eq. 3.24, the velocity at the leading edge becomes infinite. The leading edge velocity approaches infinity in a functional form given by $1/\sqrt{1+x}$ as shown by von Kármán and Burgers[6].

$$-2\frac{\partial}{\partial x}\left(\phi_\Gamma + \sum_{n=0}^{N-1}\left(\phi_{h_n}h_n + \phi_{\dot{h_n}}\dot{h_n}\right)\right)_{x=-1} = \frac{2S}{\sqrt{1+x}} \tag{3.44}$$

Using the relationships between $C(k)$, $\bar{Q}$, and $\partial\phi_\Gamma/\partial x$, the expression for leading edge suction velocity (S) in the complex form is

$$\bar{S} = \frac{\sqrt{2}}{2}\left(2C(k)-1\right)\bar{Q} - \left[\frac{\partial}{\partial x}\left(\sum_{i=0}^{N-1}\left(\phi_{h_i}\bar{h}_i + ik\phi_{\dot{h_i}}\bar{h}_i\right)\right)\frac{\sqrt{1+x}}{b}\right]_{x=-1} \tag{3.45}$$

The resulting leading edge suction velocities due to the first five motions/deformations are given in Table 3.4.

Thrust is quadratic function of sinusoids and is

$$T = T_{avg} + \bar{T}_{osc} e^{2i\omega t} \tag{3.46}$$

Using the complex form of the leading edge suction, Eq. 3.45, and pressure terms, Eq. 3.42, the average thrust is

$$T_{avg} = \frac{1}{2}\mathrm{Re}\left[\pi\rho_a b\bar{S}\bar{S}^* + \sum_{n=0}^{N} \bar{P}_n \bar{h}_n^*\right] \tag{3.47}$$

Evaluating Eq. 3.47, the thrust due to the rigid body motion terms, $\bar{h}_0$ and $\bar{h}_1$, match Garrick's solution[2]. The deformation terms also result in thrust terms and these results matched exactly with Peters' unsteady airloads theory[4].

3.4 Numerical Results

This section is focused on presenting numerical results for various cases based on the airloads derivation. Expressions for the amplitude and phase of lift and pitching moment relative to the motion are given. A detailed study into how both thrust components contribute to the thrust for various cases is presented.

3.4.1 Lift and Pitching Moment

Consider representing the harmonic motion/deformation in the form of Eq. 3.28. The values $\bar{h}_n$ are complex numbers used to represent the magnitude and phase of each motion. The complex form of lift and pitching moment for harmonic motion can be written

$$\begin{aligned} L &= \bar{L}e^{i\omega t} \\ M &= \bar{M}e^{i\omega t} \end{aligned} \tag{3.48}$$

The values $\bar{L}$ and $\bar{M}$ are complex numbers used to represent the phase and magnitude of lift and pitching moment. Using Tables 3.2 and 3.3, $\bar{L}$ and $\bar{M}$ can be evaluated and is presented in Table 3.5.

Table 3.5: Lift and pitching moment amplitude and phase terms

	$\bar{L}$	$\bar{M}$
$\bar{h_0}$	$-\pi\rho_a b u^2 \left(k^2 - i2kC(k)\right)$	$i\pi\rho_a u^2 b^2 kC(k)$
$\bar{h_1}$	$-\pi\rho_a b u^2 \left(2C(k) + ik + ikC(k)\right)$	$\pi\rho_a u^2 b^2 \left(C(k) - ik + i\frac{k}{2} + \frac{k^2}{8}\right)$
$\bar{h_2}$	$-4\pi\rho_a b u^2 \left(C(k) + \frac{k^2}{8}\right)$	$2\pi\rho_a u^2 b^2 \left(C(k) - 1 - i\frac{k}{2}\right)$
$\bar{h_3}$	$-6\pi\rho_a b u^2 C(k)$	$3\pi\rho_a u^2 b^2 \left(C(k) - 1 - \frac{k^2}{24}\right)$
$\bar{h_4}$	$-8\pi\rho_a b u^2 C(k)$	$4\pi\rho_a u^2 b^2 \left(C(k) - 1\right)$

The results in the table above are plotted for each motion/deformation. Observing the entire range of reduced frequency is done by changing the abscissa to $k/(k+1)$. Therefore when this value is zero, k is zero, when it is 0.5, k is 1, and when it is 1, k is infinity. The lift and pitching moment are nondimensionalized by $\rho_a b u^2$ and $\rho_a b^2 u^2$ respectively. Figures 3.4 and 3.5 show the magnitude of lift and pitching moment. The magnitudes are normalized by $k^2 + 1$ because lift and pitching moment grow infinite on the order of k^2. The phase of the lift and pitching moment relative to the airfoil motion change with $C(k)$. Figures 3.6 and 3.7 below show the phase of lift and pitching moment for each of the first five airfoil motions as a function of reduced frequency.

At the point when reduced frequency reaches $k \approx 0.2$, the phase shift due to $C(k)$ is maximum and as k approaches infinity, this phase shift approaches zero. For large reduced frequencies, the noncirculatory terms become large, and the phases shift is dominated by the noncirculatory flow. The plunge and pitch motion very easily show the effect Theodorsen's function has on the phase shift. The phase of the lift lags 90° with the plunge motion initially and at low reduced frequencies the phase lag increases further as reduced frequency increases. Once the noncirculatory terms in the lift expression become more prominent, the imaginary part of the lift expression becomes insignificant and the lift becomes in phase with the plunge motion. All the airfoil motion types considered show the same trends, which are due to the

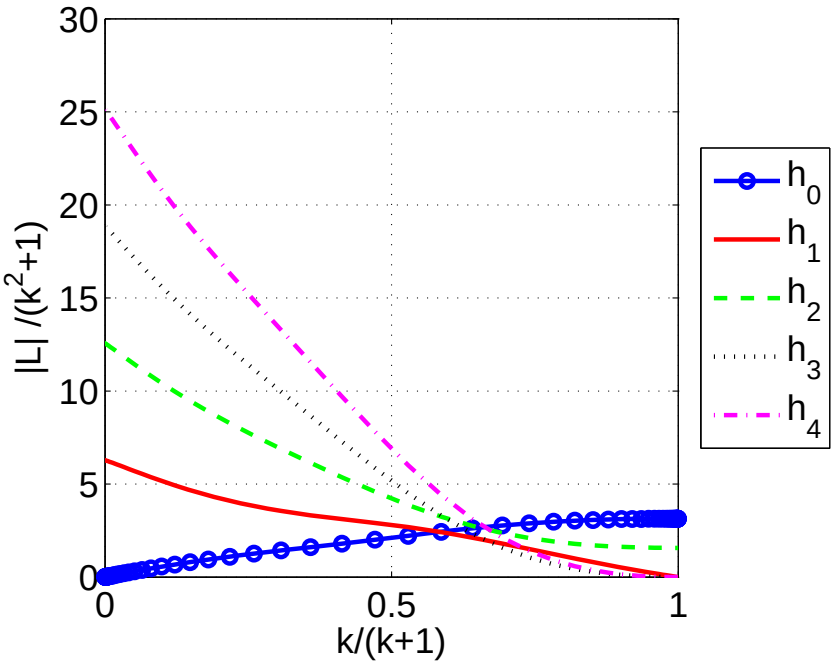

Figure 3.4: Lift magnitude

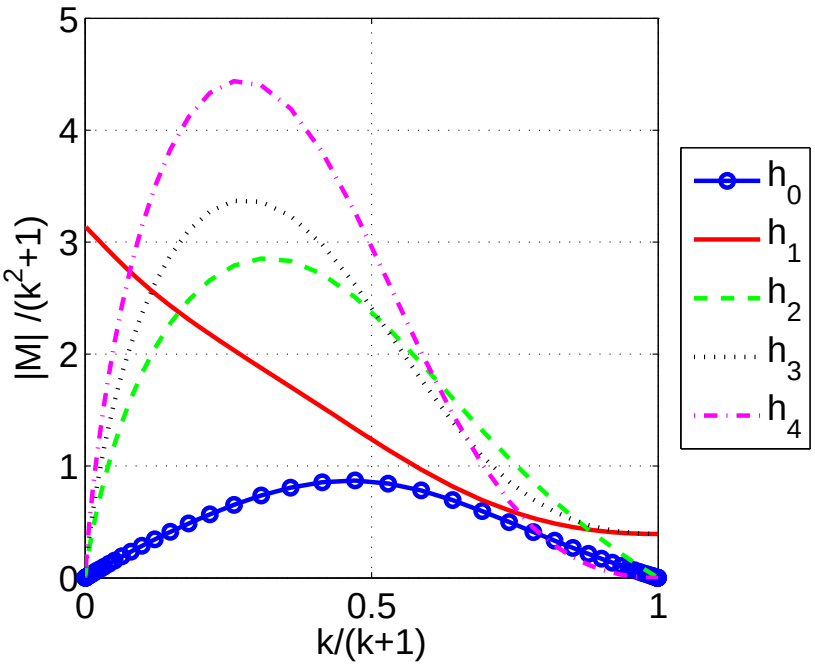

Figure 3.5: Pitching moment magnitude

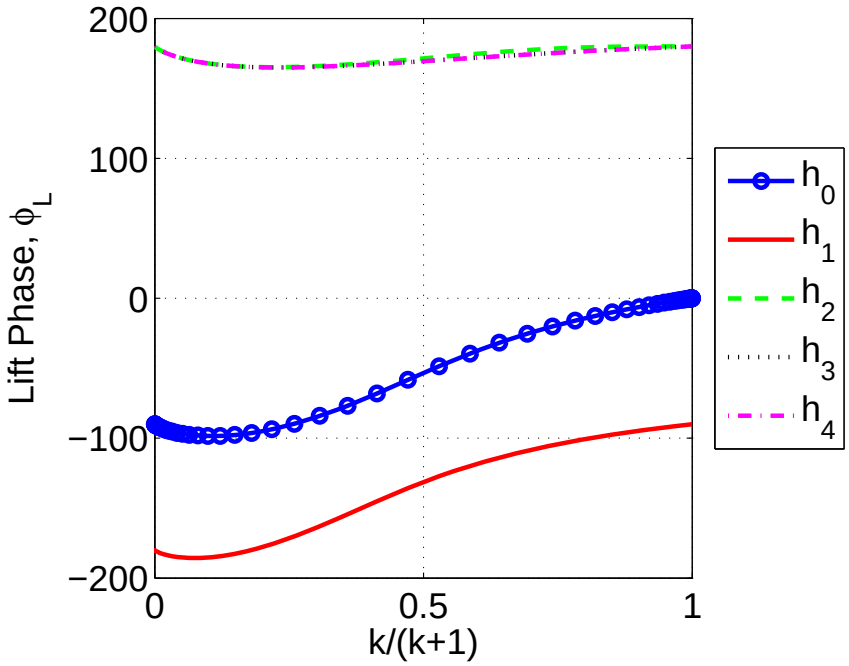

Figure 3.6: Lift phase

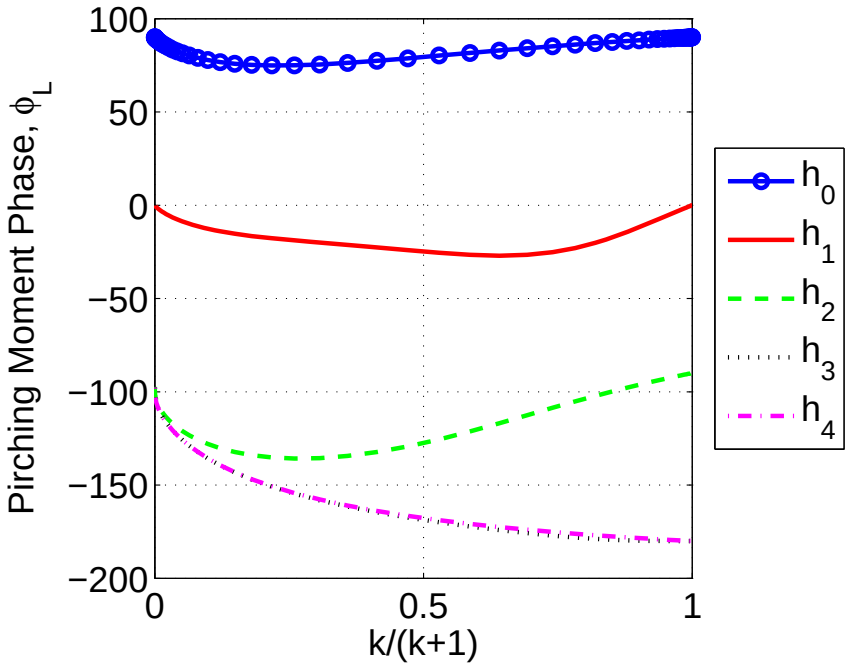

Figure 3.7: Pitching moment phase

noncirculatory terms getting very large at high reduced frequency. The h_3 term in Figure 3.6 directly coincides with the h_4 curve and cannot be seen clearly.

3.4.2 Thrust

For harmonic motion/deformation, the lift and pitching moment oscillate at the same frequency as the motion and with zero offset because they are linear. The average thrust is a purely quadratic term and thus oscillates at twice the frequency about an offset. Since thrust is a quadratic expression there are cross coupling terms.

Eq. 3.47 can be used to calculate the average thrust from the complex form of the intermediate linear results. The complete expression for the average thrust is lengthy and thus we start with the motion in only one degree of freedom. The expressions for the individual airfoil motions are much shorter due to the absence of coupled terms. The thrust due to the first five airfoil motions is

$$\begin{aligned}
T_{h_0} &= \bar{h}_0 \bar{h}_0^* k^2 \pi \rho_a u^2 b \left(F^2 + G^2\right) \\
T_{h_1} &= \bar{h}_1 \bar{h}_1^* \pi \rho_a u^2 4b \left(\left(k^2+4\right) F^2 - 2\left(k^2+2\right) F + k^2 - 2Gk + G^2\left(k^2+4\right)\right) \\
T_{h_2} &= \bar{h}_2 \bar{h}_2^* 4\pi \rho_a u^2 b \left(F^2 - F + G^2\right) \\
T_{h_3} &= \bar{h}_3 \bar{h}_3^* 9\pi \rho_a u^2 b \left(F^2 - F + G^2\right) \\
T_{h_4} &= \bar{h}_4 \bar{h}_4^* 16\pi \rho_a u^2 b \left(F^2 - F + G^2\right)
\end{aligned} \tag{3.49}$$

where, $C(k) = F + iG$. For the plunge only case, the thrust is always positive as expected. The thrust due to the other four airfoil shapes may be positive or negative based on the reduced frequency. Figure 3.8 shows the thrust force coefficient due to a unit value of each of the first five motions individually. The thrust is a function of the square of the reduced frequency, and in order to show the entire range of reduced frequency, the thrust coefficient is divided by $k^2 + 1$ where the thrust coefficient is

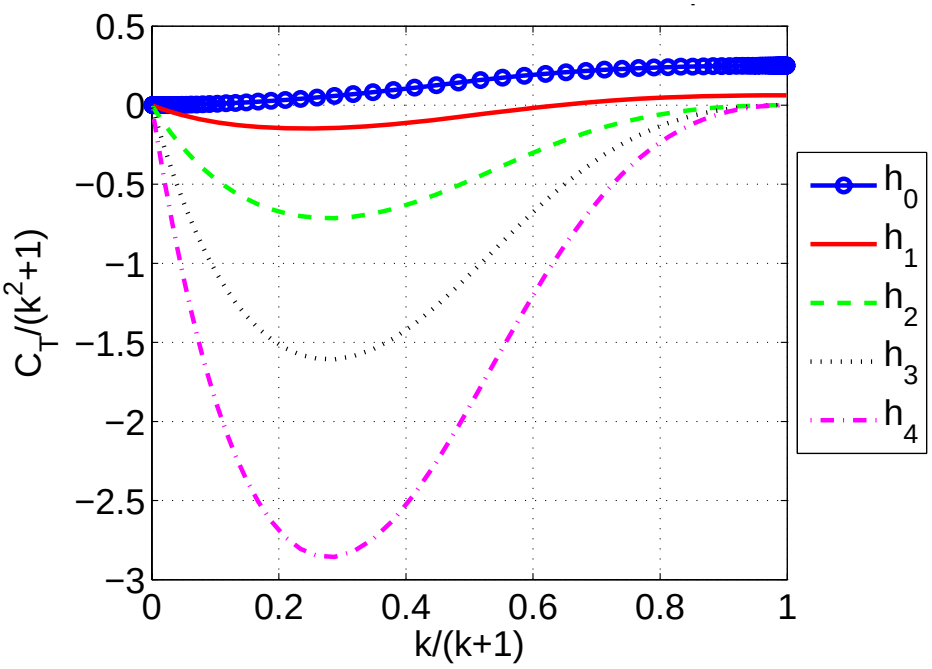

Figure 3.8: Thrust coefficient due to the first 5 deformation shapes

$$C_T = \frac{T_{avg}}{\rho_a u^2 b} \tag{3.50}$$

Figure 3.8 shows that plunge is the only motion which produces significant thrust. However, this shape along with the other shapes have cross coupling terms which can lead to added thrust depending on the phase of the additional motion relative to the plunge motion. The sensitivity of the thrust to small addition of various other terms at different phases to a pure unit plunge motion is

$$S_{C_{T_n}} = \left.\frac{\partial C_T}{\partial h_n}\right|_{h_0=1, h_i=0 \text{ for } i>=1} \tag{3.51}$$

Figures 7(a) through 7(d) show the sensitivity of pure plunge thrust to other motions. It is seen from Figure 3.9 that the addition of pitch motion can change the thrust generated by

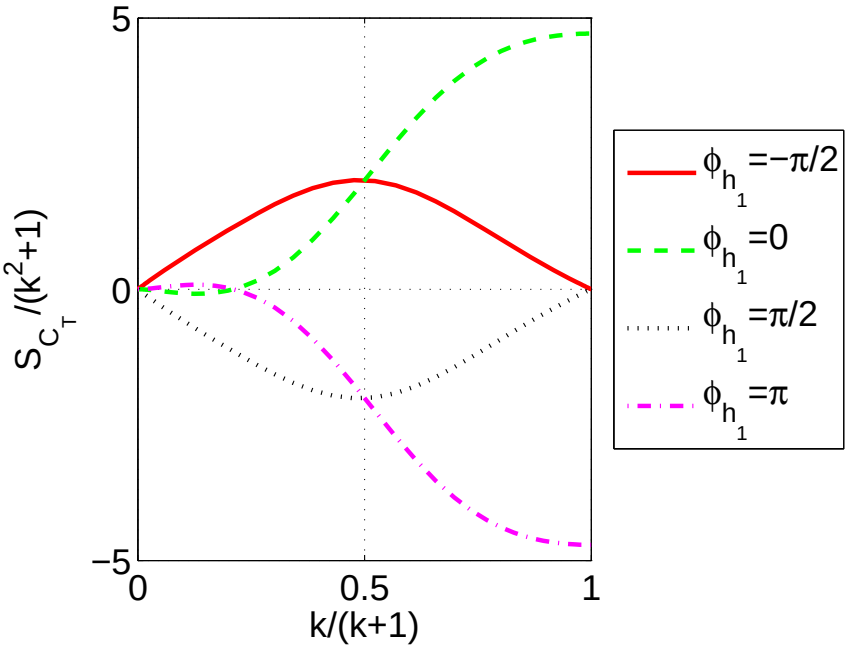

Figure 3.9: Sensitivity of thrust coefficient due to h_1 calculated at $h_0 = 1$

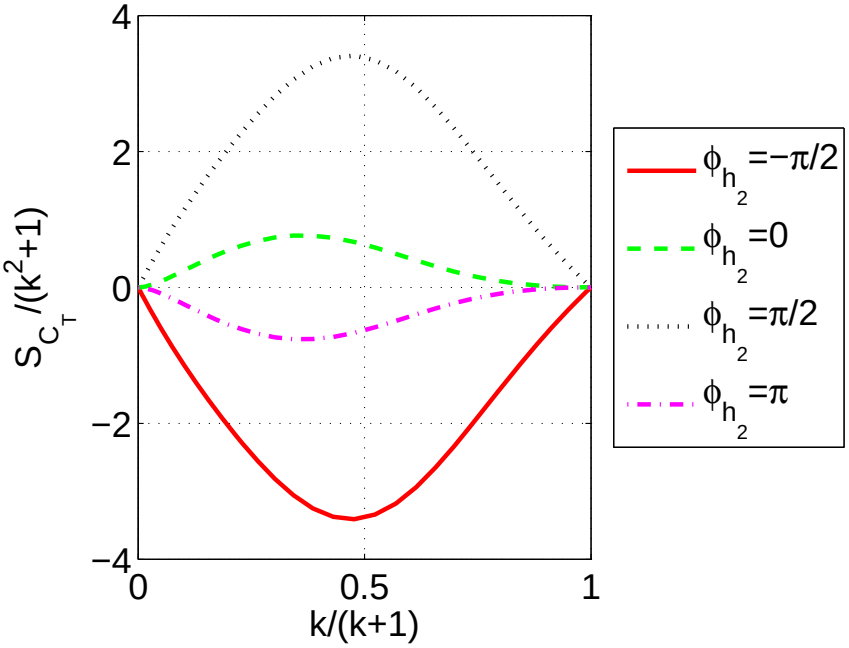

Figure 3.10: Sensitivity of thrust coefficient due to h_2 calculated at $h_0 = 1$

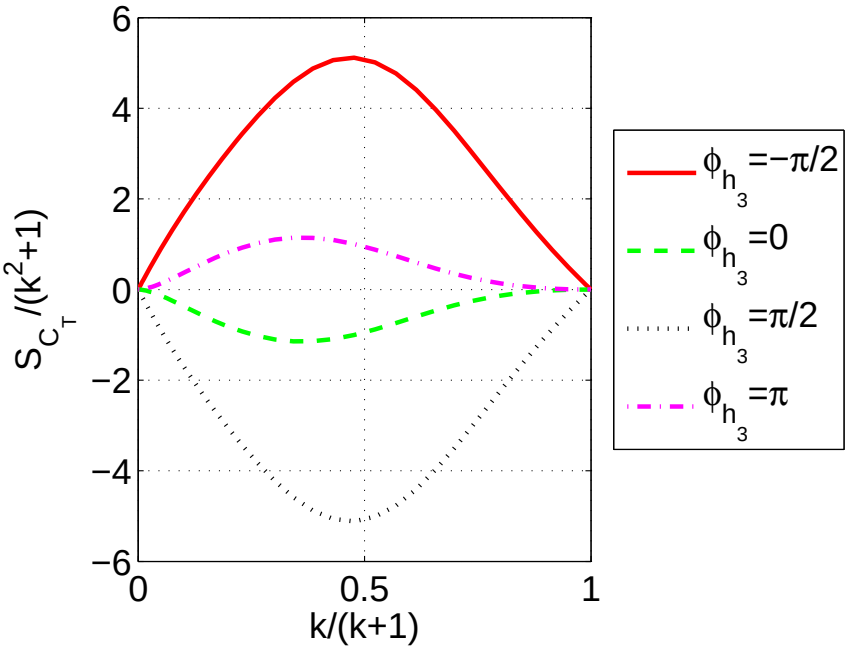

Figure 3.11: Sensitivity of thrust coefficient due to h_3 calculated at $h_0 = 1$

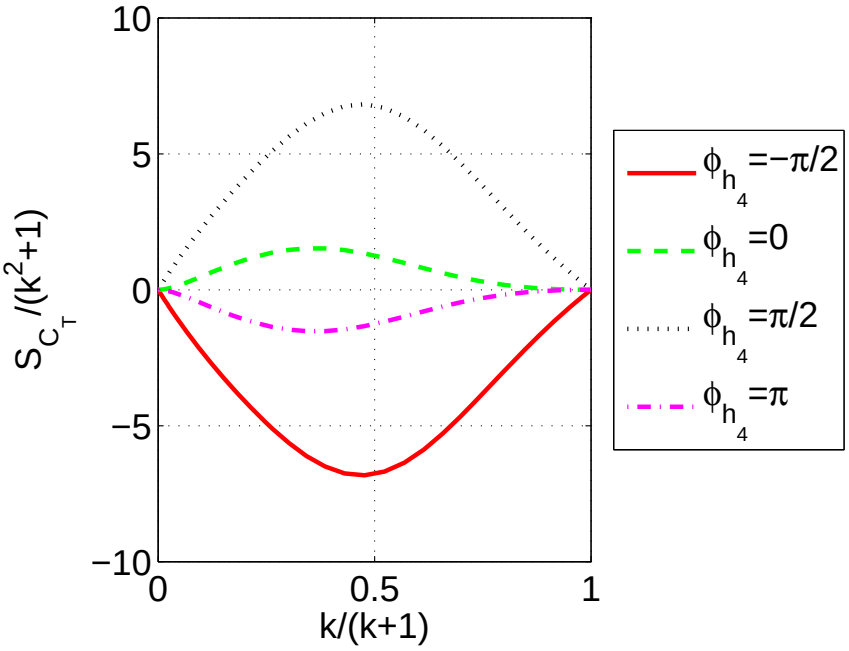

Figure 3.12: Sensitivity of thrust coefficient due to h_4 calculated at $h_0 = 1$

pure plunge. At low reduced frequencies, a phase lag of $\pi/2$ increases the thrust significantly over plunge alone, while a phase lead of π leads to a smaller increase in thrust. A phase lead of $\pi/2$ decreases the thrust in the same manner as a phase lag of $\pi/2$ increases thrust. The motion in phase with plunge leads to a drag similar to the thrust generated by a phase lead of π. For $k/(k+1) > 0.2$, the pitch motion phase lead of π relative to the plunge motion leads to a decrease rather than an increase in thrust, while in phase motion leads to an increase. As reduced frequency increases beyond $k/(k+1) > 0.5$, the pitch motion in phase with plunge produces a larger increase in thrust than a $\pi/2$ phase lag, while a phase lead of π gives a larger decrease in thrust than a phase lead of $\pi/2$. The results are dependent on which contribution to the thrust is dominant, the leading edge suction or the pressure component.

Figures 3.10 through 3.12 show the effect of adding of h_2, h_3, and h_4 motions to plunge. The phase of h_2 and h_4 motions have an opposite, but similar effect on the thrust as the addition of h_1 motion. For h_2 and h_4 at all reduced frequencies, a phase lead of $\pi/2$ leads to an increase in thrust over plunge, while a phase lag of $\pi/2$ leads to a decrease in thrust. In phase motion leads to an increase in thrust over plunge which is smaller than a $\pi/2$ phase lead, while a phase lead of π leads to a decrease in thrust over plunge which is smaller than a $\pi/2$ phase lag. The h_3 shape has an opposite effect to the h_2 and h_4 shapes. A phase lead of $\pi/2$ leads to a decrease in thrust while a phase lag of $\pi/2$ leads to an increase in thrust at all frequencies. In phase motion leads to a decrease in thrust over plunge which is smaller than a $\pi/2$ phase lead, while a phase lead of π leads to an increase in thrust over plunge which is smaller than a $\pi/2$ phase lag.

Further study shows that combinations of airfoil shapes without plunge, result in drag at low frequencies for every case. However, the combinations with h_1 become positive for larger reduced frequencies. Airfoil shape combinations without h_0 or h_1, result in drag at all frequencies.

The complete coupled equation for average thrust can also be put into the reduced frequency form like the lift and pitching moment in Table 3.5. The average thrust is

$$T_{avg} = \pi \rho_a u^2 b \frac{1}{2} \mathrm{Re}\left(\left\{ \bar{h}_i \right\} \left[T_M \right] \left\{ \bar{h}_i \right\}^T \right) \tag{3.52}$$

where the vector $\left\{ \bar{h}_i \right\}$ is

$$\left\{ \bar{h}_i \right\} = \left\{ \bar{h}_0 \quad \bar{h}_1 \quad \bar{h}_2 \quad \bar{h}_3 \quad \bar{h}_4 \right\} \tag{3.53}$$

and the components of T_M are

$$\begin{aligned}
T_{M_{11}} &= -2C(k)C(k)^T k^2 \\
T_{M_{12}} &= k(k - C(k)(C(k)^T - 1)(k - 2i)) \\
T_{M_{13}} &= 4iC(k)C(k)^T k \\
T_{M_{14}} &= 6iC(k)(C(k)^T - 1)k \\
T_{M_{15}} &= 8iC(k)C(k)^T k
\end{aligned}$$

$$\begin{aligned}
T_{M_{21}} &= C(k)^T k(k - C(k)(k - 2i)) \\
T_{M_{22}} &= \frac{k(-k + C(k)^T(k - 2i) - 2i) - C(k)(C(k)^T - 1)(k - 2i)^2}{2} \\
T_{M_{23}} &= \frac{k^2 + 4iC(k)C(k)^T k - 4iC(k)^T k + 8C(k)C(k)^T}{2} \\
T_{M_{24}} &= 3i(C(k)^T - 1)(C(k)(k - 2i) - k) \\
T_{M_{25}} &= 4C(k)^T(C(k)(ik + 2) - ik)
\end{aligned}$$

$$
\begin{aligned}
T_{M_{31}} &= 4i(C(k)-1)C(k)^T k \\
T_{M_{32}} &= \frac{4C(k)(C(k)^T-1)(ik+2)+C(k)^T(-4ik-8)-k(k-4i)}{2} \\
T_{M_{33}} &= 8(C(k)-1)C(k)^T-4ik \\
T_{M_{34}} &= \frac{k^2+24C(k)(C(k)^T-1)-24C(k)^T+24}{2} \\
T_{M_{35}} &= 16(C(k)-1)C(k)^T
\end{aligned}
$$

$$
\begin{aligned}
T_{M_{41}} &= 6iC(k)C(k)^T k \\
T_{M_{42}} &= 3C(k)(C(k)^T-1)(ik+2) \\
T_{M_{43}} &= -\frac{k^2-24C(k)C(k)^T+24}{2} \\
T_{M_{44}} &= 6(3C(k)(C(k)^T-1)-ik) \\
T_{M_{45}} &= \frac{k^2+48C(k)C(k)^T}{2}
\end{aligned}
$$

$$
\begin{aligned}
T_{M_{51}} &= 8i(C(k)-1)C(k)^T k \\
T_{M_{52}} &= 4i(k+C(k)(C(k)^T-1)(k-2i)-C(k)^T(k-2i)) \\
T_{M_{53}} &= 16(C(k)-1)C(k)^T \\
T_{M_{54}} &= -\frac{k^2-48C(k)(C(k)^T-1)+48C(k)^T}{2} \\
T_{M_{55}} &= 8(4(C(k)-1)C(k)^T-ik)
\end{aligned}
$$

Realizing each component of the vector $\left\{\bar{h}_i\right\}$ contains two variables which represent magnitude and phase, a more appropriate representation of the system in matrix form would be a 9x9 matrix. Plunge, h_0 needs only one variable as it it the reference for which the phases of each deformation shape are relative to. The vector $\left\{h_i\right\}$ is now

$$\left\{h_i\right\} = \begin{Bmatrix} h_{0re} \\ h_{1re} \\ h_{1im} \\ h_{2re} \\ h_{2im} \\ h_{3re} \\ h_{3im} \\ h_{4re} \\ h_{4im} \end{Bmatrix} \tag{3.54}$$

where the average thrust is

$$T_{avg} = \frac{1}{2}\pi\rho_a u^2 b \left\{h_i\right\}^T \left[H_{Tavg}\right] \left\{h_i\right\} \tag{3.55}$$

The thrust function is entirely quadratic and therefore when written in this form, the matrix $\left[H_{Tavg}\right]$ is the Hessian of the thrust function. The components of the thrust Hessian are

$$H_{Tavg_{11}} = 2F^2k^2 + 2G^2k^2$$
$$H_{Tavg_{12}} = H_{Tavg_{21}} = 2kF^2 - kF - Gk^2 + 2G^2k$$
$$H_{Tavg_{13}} = H_{Tavg_{31}} = F^2k^2 + G^2k^2 - Fk^2 + \frac{k^2}{2} + Gk$$
$$H_{Tavg_{14}} = H_{Tavg_{41}} = 4kF^2 - 2kF + 4G^2k$$
$$H_{Tavg_{15}} = H_{Tavg_{51}} = 2Gk$$
$$H_{Tavg_{16}} = H_{Tavg_{61}} = 6kF^2 - 3kF + 6G^2k$$
$$H_{Tavg_{17}} = H_{Tavg_{71}} = 3Gk$$
$$H_{Tavg_{18}} = H_{Tavg_{81}} = 8kF^2 - 4kF + 8G^2k$$
$$H_{Tavg_{19}} = H_{Tavg_{91}} = 4Gk$$

$$H_{Tavg_{22}} = \frac{k^2F^2}{2} + 2F^2 - k^2F - 2F + 2G^2 + \frac{G^2k^2}{2} + \frac{k^2}{2} - Gk$$
$$H_{Tavg_{23}} = H_{Tavg_{32}} = 0$$
$$H_{Tavg_{24}} = H_{Tavg_{42}} = 4F^2 - 4F + 4G^2 - Gk$$
$$H_{Tavg_{25}} = H_{Tavg_{52}} = -2kF^2 + 3kF - 2G^2k - k$$
$$H_{Tavg_{26}} = H_{Tavg_{62}} = 6F^2 - 6F + 6G^2 - \frac{3Gk}{2}$$
$$H_{Tavg_{27}} = H_{Tavg_{72}} = -3kF^2 + \frac{9kF}{2} - 3G^2k - \frac{3k}{2}$$
$$H_{Tavg_{28}} = H_{Tavg_{82}} = 8F^2 - 8F + 8G^2 - 2Gk$$
$$H_{Tavg_{29}} = H_{Tavg_{92}} = -4kF^2 + 6kF - 4G^2k - 2k$$

$$H_{Tavg_{33}} = \frac{k^2F^2}{2} + 2F^2 - k^2F - 2F + 2G^2 + \frac{G^2k^2}{2} + \frac{k^2}{2} - Gk$$
$$H_{Tavg_{34}} = H_{Tavg_{43}} = 2kF^2 - 3kF + 2G^2k + k$$
$$H_{Tavg_{35}} = H_{Tavg_{53}} = 4F^2 - 4F + 4G^2 - Gk$$
$$H_{Tavg_{36}} = H_{Tavg_{63}} = 3kF^2 - \frac{9kF}{2} + 3G^2k + \frac{3k}{2}$$
$$H_{Tavg_{37}} = H_{Tavg_{73}} = 6F^2 - 6F + 6G^2 - \frac{3Gk}{2}$$
$$H_{Tavg_{38}} = H_{Tavg_{83}} = 4kF^2 - 6kF + 4G^2k + 2k$$
$$H_{Tavg_{39}} = H_{Tavg_{93}} = 8F^2 - 8F + 8G^2 - 2Gk$$

$$H_{Tavg_{44}} = 8F^2 - 8F + 8G^2$$
$$H_{Tavg_{45}} = H_{Tavg_{54}} = 0$$
$$H_{Tavg_{46}} = H_{Tavg_{64}} = 12F^2 - 12F + 12G^2$$
$$H_{Tavg_{47}} = H_{Tavg_{74}} = 0$$
$$H_{Tavg_{48}} = H_{Tavg_{84}} = 16F^2 - 16F + 16G^2$$
$$H_{Tavg_{49}} = H_{Tavg_{94}} = 0$$

$$H_{Tavg_{55}} = 8F^2 - 8F + 8G^2$$
$$H_{Tavg_{56}} = H_{Tavg_{65}} = 0$$
$$H_{Tavg_{57}} = H_{Tavg_{75}} = 12F^2 - 12F + 12G^2$$
$$H_{Tavg_{58}} = H_{Tavg_{85}} = 0$$
$$H_{Tavg_{59}} = H_{Tavg_{95}} = 16F^2 - 16F + 16G^2$$

$$H_{Tavg_{66}} = 18F^2 - 18F + 18G^2$$
$$H_{Tavg_{67}} = H_{Tavg_{76}} = 0$$
$$H_{Tavg_{68}} = H_{Tavg_{86}} = 24F^2 - 24F + 24G^2$$
$$H_{Tavg_{69}} = H_{Tavg_{96}} = 0$$

$$H_{Tavg_{77}} = 18F^2 - 18F + 18G^2$$
$$H_{Tavg_{78}} = H_{Tavg_{87}} = 0$$
$$H_{Tavg_{79}} = H_{Tavg_{97}} = 24F^2 - 24F + 24G^2$$

$$H_{Tavg_{88}} = 32F^2 - 32F + 32G^2$$
$$H_{Tavg_{89}} = H_{Tavg_{98}} = 0$$
$$H_{Tavg_{99}} = 32F^2 - 32F + 32G^2$$

where F and G are components of Theodorsen's function $C(k) = F + iG$.

Chapter 4

Aerodynamic Optimization

This chapter presents the optimization techniques used to optimize the aerodynamic system for maximum stroke-averaged thrust and thrust efficiency. The work done by the structure and the work contributing to thrust are presented in quadratic matrix form. Constraints on the motion magnitude, leading edge suction and thrust efficiency (for multi-objective optimization) are presented and the full constrained optimization problem is posed. The stroke-averaged thrust, Eq. 3.55 is optimized with the design space consisting of the vector $\left\{h_i\right\}$.

4.1 Energy and Efficiency

Along with maximizing thrust, maximizing thrust efficiency is also desirable. Thrust efficiency is defined as the work contributing to thrust divided by the total work required to move the airfoil. Thus thrust efficiency is

$$\eta = \frac{W_T}{W_s} \tag{4.1}$$

Thrust is harmonic, but Eq. 3.55 is average thrust, which is not. The values of work done by the structure and energy contributing to thrust can be calculated as the average of the

work done over one oscillation. The work done by the structural motion is the integral over one oscillation of the power required, which is the product of the velocity and aerodynamic force. Thus,

$$W_s = b^2 \int_0^T \int_{-1}^{1} \Delta p(x,t) \frac{\partial w(x,t)}{\partial t} dx dt \tag{4.2}$$

where T is the period of oscillation, $w(x,t)$ is the airfoil shape defined by Eq. 3.4, and $\Delta p(x)$ is the pressure difference. Using the complex form of deformation, $h_i = \bar{h}_i e^{i\omega t}$, the motion and pressure difference are

$$\frac{\partial w}{\partial t} = i\omega \bar{w} e^{i\omega t} \tag{4.3}$$

$$\Delta p = \Delta \bar{p}(x) e^{i\omega t} \tag{4.4}$$

where $i\omega\bar{w}$ and $\Delta\bar{p}(x)$ are complex functions of chordwise location representing the amplitude and phase of the motion and the pressure difference along the chord. Using this formulation, the average work done by the structure can be calculated as

$$W_{Scomplex} = \frac{b^2}{2} \mathrm{Re} \left(\int_{-1}^{1} \Delta \bar{p}(x) (i\omega \bar{y})^* dx \right) \tag{4.5}$$

where $()^*$ is a complex conjugate and the pressure difference is given in Eq. 3.38.

The work done by the structure is calculated from Eq. 4.5, and can be written in the quadratic matrix form just like the thrust and is

$$W_{Savg} = \frac{1}{2}\pi\rho_a u^3 b \left\{h_i\right\}^T \left[H_{Savg}\right] \left\{h_i\right\} \tag{4.6}$$

The components of the structural work Hessian are

$$\begin{aligned}
H_{WSavg_{11}} &= 4Fk^2 \\
H_{WSavg_{12}} &= H_{WSavg_{21}} = 2Gk + k^2 \\
H_{WSavg_{13}} &= H_{WSavg_{31}} = 2Fk - 2Gk^2 \\
H_{WSavg_{14}} &= H_{WSavg_{41}} = 4Gk \\
H_{WSavg_{15}} &= H_{WSavg_{51}} = 4Fk \\
H_{WSavg_{16}} &= H_{WSavg_{61}} = 6Gk \\
H_{WSavg_{17}} &= H_{WSavg_{71}} = 6Fk \\
H_{WSavg_{18}} &= H_{WSavg_{81}} = 8Gk \\
H_{WSavg_{19}} &= H_{WSavg_{91}} = 8Fk
\end{aligned}$$

$$\begin{aligned}
H_{WSavg_{22}} &= -2Gk + k^2 - Fk^2 \\
H_{WSavg_{23}} &= H_{WSavg_{32}} = 0 \\
H_{WSavg_{24}} &= H_{WSavg_{42}} = -2Gk \\
H_{WSavg_{25}} &= H_{WSavg_{52}} = 2k - Fk \\
H_{WSavg_{26}} &= H_{WSavg_{62}} = -3Gk \\
H_{WSavg_{27}} &= H_{WSavg_{72}} = 3k - 3Fk \\
H_{WSavg_{28}} &= H_{WSavg_{82}} = -4Gk \\
H_{WSavg_{29}} &= H_{WSavg_{92}} = 4k - 4Fk
\end{aligned}$$

$$
\begin{aligned}
H_{WSavg_{33}} &= -2Gk + k^2 - Fk^2 \\
H_{WSavg_{34}} &= H_{WSavg_{43}} = -2k + 2Fk \\
H_{WSavg_{35}} &= H_{WSavg_{53}} = -2Gk \\
H_{WSavg_{36}} &= H_{WSavg_{63}} = -3k + 3Fk \\
H_{WSavg_{37}} &= H_{WSavg_{73}} = -3Gk \\
H_{WSavg_{38}} &= H_{WSavg_{83}} = -4k + 4Fk \\
H_{WSavg_{39}} &= H_{WSavg_{93}} = -4Gk
\end{aligned}
$$

$$
H_{WSavg_{4-9,4-9}} = 0
$$

The energy contributing to the thrust over one oscillation is

$$
W_T = \int_0^T T(t) u dt \tag{4.7}
$$

where u is the free stream velocity. Therefore, the work done by thrust can also be written in the quadratic matrix form

$$
W_{Tavg} = T_{avg} u = \frac{1}{2} \pi \rho_a u^3 b \left\{ h_i \right\}^T \left[H_{Tavg} \right] \left\{ h_i \right\} \tag{4.8}
$$

The energy transferred to the wake is shown by conservation of energy to be

$$
W_T = W_s + W_w \tag{4.9}
$$

The thrust efficiency is the ratio of energy contributing to thrust to energy generated by the structural motion. This value ranges from 0 to 1 in a thrust producing region, and therefore has a maximum. Mathematically, thrust efficiency can have other values in drag producing regions of the domain as shown by Patil, but it does not represent efficiency of thrust production anymore[18]. Using the quadratic matrix forms of the work terms, the thrust efficiency can be written in matrix form as

$$\eta = \frac{\left\{h_i\right\}^T \left[H_{Tavg}\right] \left\{h_i\right\}}{\left\{h_i\right\}^T \left[H_{WSavg}\right] \left\{h_i\right\}} \tag{4.10}$$

4.2 Optimization

Consider the thrust function, Eq. 3.55. The maximum thrust is found by setting the gradient of the function equal to zero.

$$\nabla T_{avg} = 0 \;\rightarrow\; \pi \rho_a u^2 b \left[H_{Tavg}\right] \left\{h_i\right\}_{maxT} = 0 \tag{4.11}$$

where $\left\{h_i\right\}_{maxT}$ is the vector which yields a maximum value of average thrust. The Hessian is not singular and thus the only possible solution is $h_{i_{maxT}} = 0$. Furthermore, the Hessian is positive indefinite and thus there is neither a finite maximum or minimum. This is obvious by inspection of the components in the thrust equation. The derivation of the deformable thin airfoil theory utilized a small disturbance assumption to linearize the equations. Thus for a given relative magnitude of h_i, as the overall magnitude of deformation increases, the magnitude of thrust increases quadratically and therefore no maximum exists.

However, a maximum can be found by constraining the system by restricting the motion. A motion constraint is reasonable because the theory itself relies on the assumption of small disturbances. Furthermore, in actual MAV systems, the kinematics will constrain

the total amplitude of motion. The unsteady thin airfoil theory also assumes an inviscid theory. The effects of viscosity will lead to flow separation at large motion/deformations which the unsteady thin airfoil theory cannot model. Ideally, a constraint on the pressure gradient is desirable. However, exact closed form solutions for boundary layer theory do not exist outside of simple situations such as steady flow on flat plates and wedges. Here a leading edge suction constraint is used to address leading edge separation.

4.2.1 Magnitude Constraint

Using a total motion/deformation magnitude constraint is a good way of constraining the motion to fit within a small disturbance assumption. Since the h_i's are nondimensionalized by the semichord, b, the constraint is

$$\sum_{i=1}^{N} h_i^2 \leq 1 \tag{4.12}$$

or in matrix form,

$$\left\{h_i\right\}^T \left\{h_i\right\} \leq 1 \tag{4.13}$$

This constraint is restricts the root mean square deformation to be equal to the semichord. Hence, it gives us optimum values of thrust per 'unit' non-dimensional deformation/motion.

As stated previously, the magnitude of the thrust increases quadratically with the magnitude of motion. Therefore, the maximum thrust with this constraint will occur as a vertex in the design space. Consequently, the constraint may be written as an equality.

$$m(h_i) = \left\{h_i\right\}^T \left\{h_i\right\} - 1 \tag{4.14}$$

The maximum thrust is found by generating the Lagrangian and solving the system of equations generated by setting its gradient to zero. The Lagrangian is

$$L(h_i, \lambda_m) = \frac{1}{2}\pi\rho_a u^2 b \left\{h_i\right\}^T \left[H_{Tavg}\right] \left\{h_i\right\} - \lambda_m m(h_i) \tag{4.15}$$

where λ_m is the Lagrange multiplier for the motion constraint. Setting the gradient of the Lagrangian equal to zero results in

$$\begin{aligned} \pi\rho_a u^2 b \left[H_{Tavg}\right] \left\{h_i\right\} - \lambda_m \left\{h_i\right\} = 0 \\ \left\{h_i\right\}^T \left\{h_i\right\} - 1 = 0 \end{aligned} \tag{4.16}$$

The first equation above is an eigenvalue problem.

$$\nabla L_h(h_i, \lambda_m) = \left[\pi\rho_a u^2 b \left[H_{Tavg}\right] - \lambda_m I\right] \left\{h_i\right\} = 0 \tag{4.17}$$

where ∇L_h is the gradient with respect to the vector h_i and not the Lagrange multiplier and I is the identity matrix. The problem has nine principle directions defined by the nine eigenvectors, with magnitudes given by the nine eigenvalues. The direction which results in the largest eigenvalue is the maximum. Therefore, the motion required to generate the maximum thrust is the eigenvector corresponding to the largest eigenvalue. It should be noted that the eigenvector is scaled by the motion constraint, which is 1 for this case.

4.2.2 Efficiency Constraint

A high value of thrust is essential, however for a flapping wing aircraft, the efficiency is also important. The maximum thrust may not occur at a desirable efficiency. The thrust efficiency, Eq. 4.1, can be optimized using the same technique. However, as the thrust

efficiency approaches 1, the thrust approaches zero as outlined in Patil[18]. While a maximum efficiency may not be useful, a point between maximum efficiency and maximum thrust may be desirable. Therefore generating a Pareto front for thrust and efficiency will be useful. This can be done by forcing the efficiency to be a certain value and optimizing the thrust. This is accomplished by using an efficiency constraint. The problem with two Lagrange multipliers is no longer an eigenvalue problem. However, a solution can easily be found using a numerical method such as Newton-Raphson. The problem of an efficiency constraint without a magnitude constraint is not a well posed problem and is not considered. The efficiency where the maximum thrust occurs can be calculated using Eq. 4.1. Therefore the analytic solution for the maximum thrust provides a good initial guess for a numerical method to generate a Pareto front. The efficiency constraint is

$$\eta(h_i, k) - \eta_{ref} = 0 \tag{4.18}$$

where η_{ref} is the required efficiency.

The efficiency constraint is written as

$$\eta(h_i) = \left\{h_i\right\}^T \left[\left[H_{Tavg}\right] - \eta_{ref}\left[H_{WSavg}\right]\right]\left\{h_i\right\} = 0 \tag{4.19}$$

The optimization problem can be written with two constraints in the same manner as with the magnitude constraint alone. The Lagrangian is given by

$$L(h_i, \lambda_m, \lambda_\eta) = \frac{1}{2}\pi\rho_a u^2 b\left\{h_i\right\}^T\left[H_{Tavg}\right]\left\{h_i\right\} - \lambda_m m(h_i) - \lambda_\eta \eta(h_i) \tag{4.20}$$

where λ_η is the Lagrange multiplier for the efficiency constraint. Once again the maximum is found by setting the gradient of the Lagrangian equal to zero, with the constraint equations

Eq. 4.14 and Eq. 4.19 being recovered as derivatives with respect to the Lagrange multipliers to give $N+2$ equations.

$$\begin{aligned}
&\pi\rho_a u^2 b\left[H_{Tavg}\right]\left\{h_i\right\} - \lambda_m\left\{h_i\right\} - \lambda_\eta\left[\left[H_{Tavg}\right] - \eta_{ref}\left[H_{WSavg}\right]\right]\left\{h_i\right\} = 0 \\
&\left\{h_i\right\}^T\left\{h_i\right\} - 1 = 0 \\
&\left\{h_i\right\}^T\left[\left[H_{Tavg}\right] - \eta_{ref}\left[H_{WSavg}\right]\right]\left\{h_i\right\} = 0
\end{aligned} \tag{4.21}$$

The solutions of Eq. 4.21 will generate a Pareto front by solving the system of equations for various values of reference efficiency, η_{ref}, and obtaining the maximum thrust. The Newton-Raphson method is used to solve the nonlinear system of equations.

4.2.3 Leading Edge Suction Constraint

Constraints need to be chosen in such a way that the assumptions used to derive the theory are not violated. Thus far a constraint on the pressure gradient was considered, but found to be impractical due to the complexity of the constraint itself and the lack of sufficient theory to model flow separation on a deforming thin airfoil. The motion has been constrained to be within a small disturbance assumption. However, for a thin leading edge, in general there still will be leading edge separation.

As shown in the pressure equation, Eq. 3.38, the pressure difference at the leading edge, $x = -1$, goes to infinity. Because of this, the gradient of the pressure difference goes to infinity as well. Therefore, flow separation will always occur at the leading edge unless the numerator of the pressure difference equation is also zero. Physically this is possible. Consider the flow around the leading edge of a flat plate. In a flow situation where the direction of the flow at the leading edge is not moving directly into the leading edge, the flow must curve around the leading edge of the airfoil. A thin airfoil has a small radius of curvature and thus the flow requires very high acceleration to move around the airfoil. This is what drives the pressure difference to infinity. If an airfoil with thickness was being

considered, the pressure difference would not be infinity, but go to some high value. Airfoils such as these can be modeled fairly well with the infinite pressure difference described by thin airfoil theory. However, since an airfoil without thickness is being considered, it is known that separation will occur at the leading edge and thus the constraint is necessary.

Now, consider the situation where locally near the leading edge the angle of attack and the flow direction are the same. In other words, the flow is moving directly into the airfoil. For this situation, the flow does not need to curve around the leading edge, and therefore will not separate. This occurs when the stagnation point is at the leading edge and there is no leading edge suction. Therefore a constraint applied to the deforming airfoil which makes the leading edge suction zero, would represent a flow situation with no leading edge separation. This flow situation makes the inviscid theory applicable to the situation where thrust is generated by pressure only.

Leading edge suction is proportional to the leading edge suction velocity S, a complex term, and when set equal to zero leads to two constraints. By setting the real and the imaginary parts of the leading edge suction to zero will result in a total of three constraints for thrust optimization and four constraints for the thrust/efficiency Pareto fronts. The leading edge suction given in Walker and Patil[5] can be written in matrix form as

$$\begin{aligned} \mathrm{Re}(S) &= \left\{h_i\right\}^T \left[S_{Re}\right] \\ \mathrm{Im}(S) &= \left\{h_i\right\}^T \left[S_{Im}\right] \end{aligned} \tag{4.22}$$

where the $\left[S_{Re}\right]$ and $\left[S_{Im}\right]$ matrices are

$$\left[S_{Re}\right] = \sqrt{2}u \begin{bmatrix} -Gk \\ F - \frac{1}{2}Gk \\ \frac{1}{2}(k - 2G - Fk) \\ 2(F-1) \\ -2G \\ 3F \\ -3G \\ 4(F-1) \\ -4G \end{bmatrix} \qquad \left[S_{Im}\right] = \sqrt{2}u \begin{bmatrix} Fk \\ G + \frac{1}{2}k(F-1) \\ F - \frac{1}{2}Gk \\ 2G \\ 2(F-1) \\ 3G \\ 3F \\ 4G \\ 4(F-1) \end{bmatrix} \tag{4.23}$$

The leading edge suction constraint is

$$\begin{aligned} S_{Re}(h_i) &= \left\{h_i\right\}^T \left[S_{Re}\right] = 0 \\ S_{Im}(h_i) &= \left\{h_i\right\}^T \left[S_{Im}\right] = 0 \end{aligned} \tag{4.24}$$

These two constraints are linear equality constraints and can be used to solve for two of the design variables in terms of the others. Furthermore since the constraints are homogeneous, a variable transformation can be used which reduces the number of variables by 2. This is done with a variable transformation. The reduced system will satisfy the leading edge suction constraints and therefore the optimization problem will be similar to the one without leading edge constraints but with two less design variables. Solving for h_1 and h_2 in terms of $h_3 - h_n$ results in,

$$\left\{h_i\right\} = \left[\bar{M}\right] \left\{g_i\right\} \tag{4.25}$$

where the vector, $\left\{g_i\right\}$ is of length $n-2$, and

$$\left[\bar{M}\right] = \begin{bmatrix} -\frac{F^2\left(k^2+4\right)-2Fk^2+G^2\left(k^2+4\right)-4Gk+k^2}{2k(2F^2+G(2G-k))} & \frac{k\left(F^2-F+G^2\right)}{2F^2+G(2G-k)} & 1 & 0 & 0 & 0 & 0 & 0 & 0 \\ \frac{2\left((F-1)^2k+G^2k-2G\right)}{k(2F^2+G(2G-k))} & -\frac{4\left(F^2-F+G^2\right)}{2F^2+G(2G-k)} & 0 & 1 & 0 & 0 & 0 & 0 & 0 \\ -\frac{4\left(F^2-F+G^2\right)}{k(2F^2+G(2G-k))} & \frac{4G}{2F^2+2G^2-Gk} & 0 & 0 & 1 & 0 & 0 & 0 & 0 \\ \frac{3\left(F^2-F+G^2\right)}{2F^2+G(2G-k)} & -\frac{6\left(F^2+G^2\right)}{2F^2+G(2G-k)} & 0 & 0 & 0 & 1 & 0 & 0 & 0 \\ -\frac{3}{k} & 0 & 0 & 0 & 0 & 0 & 1 & 0 & 0 \\ \frac{4\left((F-1)^2k+G^2k-2G\right)}{k(2F^2+G(2G-k))} & -\frac{8\left(F^2-F+G^2\right)}{2F^2+G(2G-k)} & 0 & 0 & 0 & 0 & 0 & 1 & 0 \\ -\frac{8\left(F^2-F+G^2\right)}{k(2F^2+G(2G-k))} & \frac{8G}{2F^2+2G^2-Gk} & 0 & 0 & 0 & 0 & 0 & 0 & 1 \end{bmatrix}^T \tag{4.26}$$

This variable transformation applied to the thrust optimization problem reduces the problem to

$$L(g_i, \lambda_m) = \frac{1}{2}\pi\rho_a u^2 b \left\{g_i\right\}^T \left[\bar{M}\right]^T \left[H_{Tavg}\right] \left[\bar{M}\right] \left\{g_i\right\} - \lambda_m \left\{g_i\right\}^T \left[\bar{M}\right]^T \left[\bar{M}\right] \left\{g_i\right\} \tag{4.27}$$

where ∇L_g is the gradient with respect to the vector g_i. The maximum thrust is obtained by taking the gradient of the Lagrangian which results in a generalized eigenvalue problem.

$$\nabla L_g(g_i, \lambda_m) = \frac{1}{2}\pi\rho_a u^2 b \left(\left[\bar{M}\right]^T \left[H_{Tavg}\right] \left[\bar{M}\right] - \lambda_m \left[\bar{M}\right]^T \left[\bar{M}\right]\right) \left\{g_i\right\} = 0 \tag{4.28}$$

The eigenvector, $\left\{g_i\right\}$, corresponding to the largest eigenvalue of the generalized eigenvalue problem can be transformed back into the motion, $\left\{h_i\right\}$, via Eq. 4.25, which generates a maximum thrust.

The problem of the leading edge suction constraint, magnitude constraint and efficiency constraint is given in the reduced space as

$$L(g_i, \lambda_m, \lambda_\eta) = \frac{1}{2}\pi\rho_a u^2 b \left\{g_i\right\}^T \left[H_{Tavg}\right] \left\{g_i\right\} - \lambda_m m(g_i) - \lambda_\eta \eta(g_i) \tag{4.29}$$

Once again the maximum is found by setting the gradient of the Lagrangian equal to zero,

$$\begin{aligned} &\pi\rho_a u^2 b \left[\bar{M}\right]^T \left[H_{Tavg}\right] \left[\bar{M}\right] \left\{g_i\right\} - \lambda_m \left[\bar{M}\right]^T \left[\bar{M}\right] \left\{g_i\right\} - \\ &\lambda_\eta \left[\bar{M}\right]^T \left[\left[H_{Tavg}\right] - \eta_{ref} \left[H_{WSavg}\right]\right] \left[\bar{M}\right] \left\{g_i\right\} \\ &\left\{g_i\right\}^T \left[\bar{M}\right]^T \left[\bar{M}\right] \left\{g_i\right\} - 1 = 0 \\ &\left\{g_i\right\}^T \left[\bar{M}\right]^T \left[\left[H_{Tavg}\right] - \eta_{ref} \left[H_{WSavg}\right]\right] \left[\bar{M}\right] \left\{g_i\right\} = 0 \end{aligned} \tag{4.30}$$

As with the case without the leading edge suction constraint, the problem resembles an eigenvalue problem with multiple eigenvalues. However, with the efficiency constraint it is not possible to reduce the space and once again the system of equations may be solved using the Newton-Raphson method. Using the analytic solution to the problem with the leading edge suction constraint and without the efficiency constraint provides a starting point for the Newton-Raphson method on the above system.

Chapter 5

Aerodynamic Optimization Results

The nonlinear system of equations for the magnitude constraint resulted in an eigenvalue problem as shown by Eq. 4.17. Therefore an analytic solution was found for that case. However, the efficiency constraint problems were solved using the Newton-Raphson method. Results were generated for cases with plunge and pitch, $\bar{h}_0 - \bar{h}_1$ ($h_1 - h_3$) through cases five shapes (plunge, pitch, and three deformations), $\bar{h}_0 - \bar{h}_4$ ($h_1 - h_9$). Verification of the results was done with numerical gradient based optimization. The sequential quadratic programming algorithm "active-set" in MATLAB's *fmincon* was used.

5.1 Thrust Optimization

The maximum achievable thrust within a magnitude constrained system is given in Figure 5.1. The thrust coefficient is normalized by the thrust coefficient for plunge only, denoted as C_{T0}. At low reduced frequencies it is obvious that the addition of any shapes leads to a large percent increase in thrust over plunge. At higher reduced frequencies, the maximum thrust does increase, but by a much smaller amount. The addition of $\bar{h}_2$ (quadratic camber) motion to pitch and plunge provides a significant increase in thrust between reduced frequencies of 0.25 and 2. The addition of more than one deformation shape beyond plunge/pitch provides a minimal benefit at all reduced frequencies.

It should be noted that the apparent exponential increase in each plot as reduced frequency approaches zero does not imply that the sensitivity of thrust to changes in each deformation shape is large at this point. The sensitivity of thrust to each shape actually approaches zero as reduced frequency approaches zero, as seen in Figures 3.9 through 3.12. The reason for the exponential increase shown in the optimization results below is because of the comparison to C_{T0}. As an example, consider the thrust for pitch and plunge divided by the thrust due to plunge only. As reduced frequency goes to zero, the components of Theodorsens function go to $F = 1$ and $G = 0$. Substituting these values in for F and G results in

$$\frac{C_T}{C_{T0}} = 1 + \frac{h_{1Re}}{2h_0} + \frac{h_{1Im}}{h_0 k} \tag{5.1}$$

and thus the limit of this function as k approaches zero is infinity.

The maximum achievable thrust for a system with a magnitude constraint and a leading edge suction constraint is shown in Figure 5.2. The thrust coefficient is again normalized by the thrust coefficient for plunge only motion without leading edge suction constraint. It should be noted that all the thrust due to pure plunge is caused by leading edge suction[2] and thrust due to pressure is only produced for motion shapes of $\bar{h}_1$ and above. As with the case of only a magnitude constraint, the addition of deformation shapes leads to an increase in the maximum thrust. The addition of enough shapes at low reduced frequencies makes it possible to generate thrust larger than plunge alone without the use of leading edge suction. This is a very useful result because it shows that more thrust than plunge only can be generated without leading edge separation.

The efficiency at which maximum thrust occurs is shown in Figures 5.3 and 5.4. The efficiency due to plunge motion changes from 100% at low reduced frequencies to 50% at high reduced frequencies. However, when the magnitude is constrained, the efficiency for maximum thrust approaches 50% with the addition of deformation shapes at all frequencies. When the magnitude and leading edge suction are constrained, the efficiency of pitch and

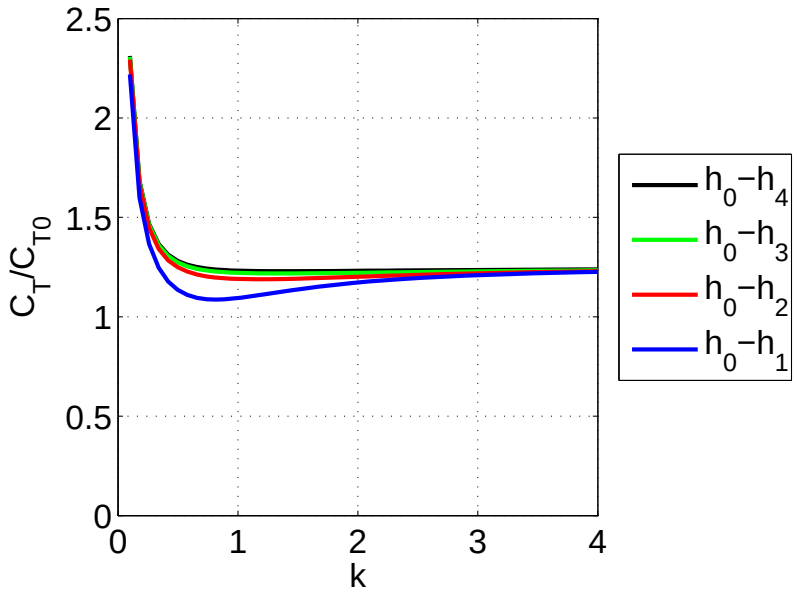

Figure 5.1: Maximum thrust with magnitude constraint

plunge motion is 50%. The addition of deformation shapes changes the efficiency slightly, but still appraoches 50% for high reduced frequencies.

Figures 5.1 and 5.2 show that increasing the design space to include more deformation shapes does increase the maximum thrust. However, the magnitude of the increase is not very large for higher reduced frequencies. The efficiency was not considered in the above results. It was seen that maximum thrust occurs at an undesirable efficiency. Thus, constraining the efficiency to be a specific value will result in much different increases in thrust as a function of reduced frequency.

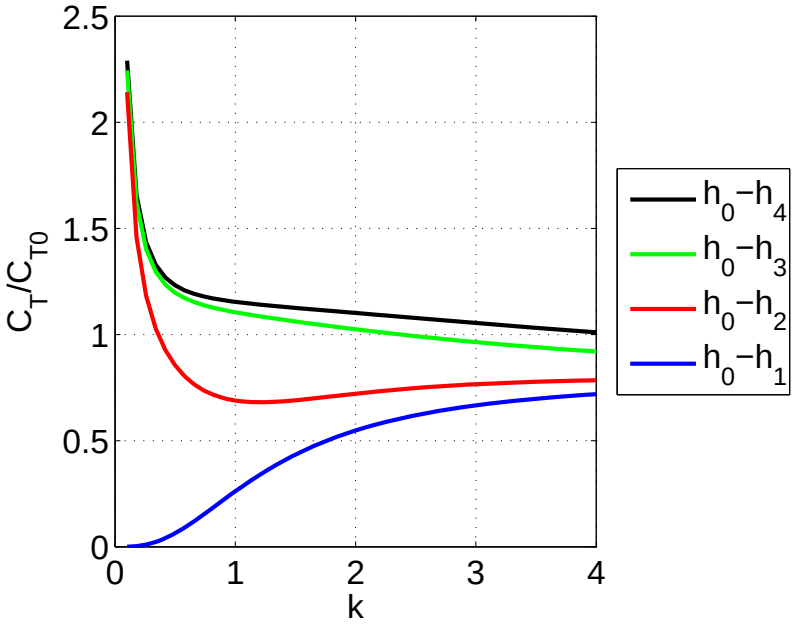

Figure 5.2: Maximum thrust with magnitude and leading edge suction constraint

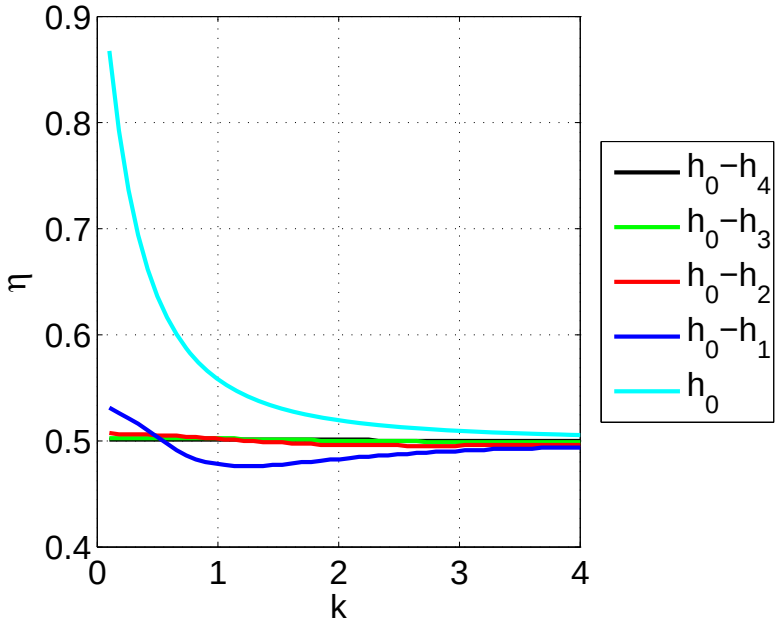

Figure 5.3: Efficiency of maximum thrust with magnitude constraint

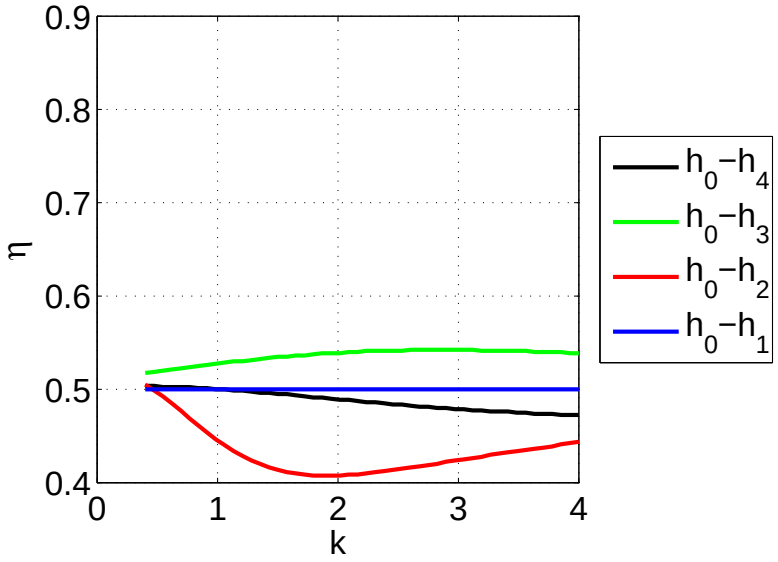

Figure 5.4: Efficiency of maximum thrust with magnitude and leading edge suction constraint

5.2 Thrust and Efficiency Optimization

The multi-objective optimization problem with thrust and efficiency metrics was solved numerically using the maximum thrust solution as the initial guess. The efficiency of the maximum thrust was typically around 50% for cases without as well as with leading edge suction constraint. Pareto fronts for thrust and efficiency were generated by constraining the efficiency and optimizing thrust. Figures 5.5 through 5.8 show Pareto fronts for four reduced frequencies with only a magnitude constraint, with Figure 5.6 representing the bird flight regime[56]. Each figure shows the change in the Pareto front by adding deformation shapes, with a point representing the thrust and efficiency of plunge only. The Pareto front is actually only the solid line, the Pareto optimal solution. However, points for maximum thrust at efficiencies below the efficiency for maximum thrust can be generated and shown. The dashed line represents the maximum thrust for constrained values of efficiency below that which maximum thrust occurs. For each case, the Pareto front with more design freedom lies above the Pareto front with less. This shows that by adding deformation shapes, the maximum thrust increases for a given efficiency and the maximum efficiency increases for a

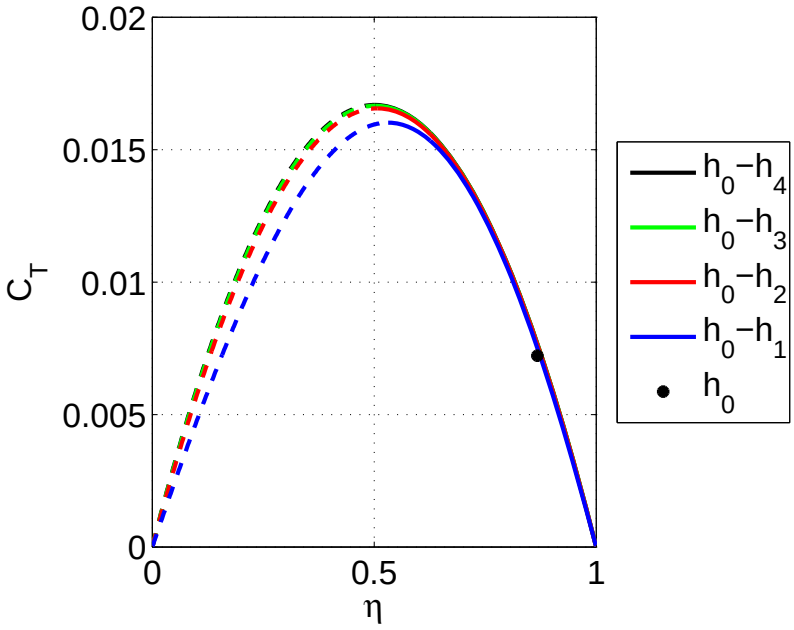

Figure 5.5: Pareto Front for $k = 0.01$ (Magnitude constraint only)

given thrust. As reduced frequency increases, the shape of the Pareto fronts becomes more of a bell shape which gets narrower at even higher reduced frequencies. This shows that by expanding the design space by adding a deformation shape variable, the maximum thrust increases by a very large amount for higher efficiencies, which is shown more clearly later in Figure 5.14.

Figures 5.9 through 5.12 show Pareto fronts generated for four reduced frequencies for the case of both a magnitude and a leading edge suction constraint. Each figure shows the change in the Pareto front by adding deformation shapes, with a point representing the thrust and efficiency of pitch and plunge only. Note that due to the two leading edge constraints and one magnitude constraint, we have no solution for just plunge and only one possible solution for pitch and plunge (with three design variables) which satisfies the constraint. Like the case of a magnitude constraint only, for each case, the Pareto front with more deformation design variables lies above the Pareto front with less. Again, this shows that by expanding the design space by adding deformation shape variables, the maximum thrust increases for a given efficiency and the maximum efficiency increases for a given thrust. However, the

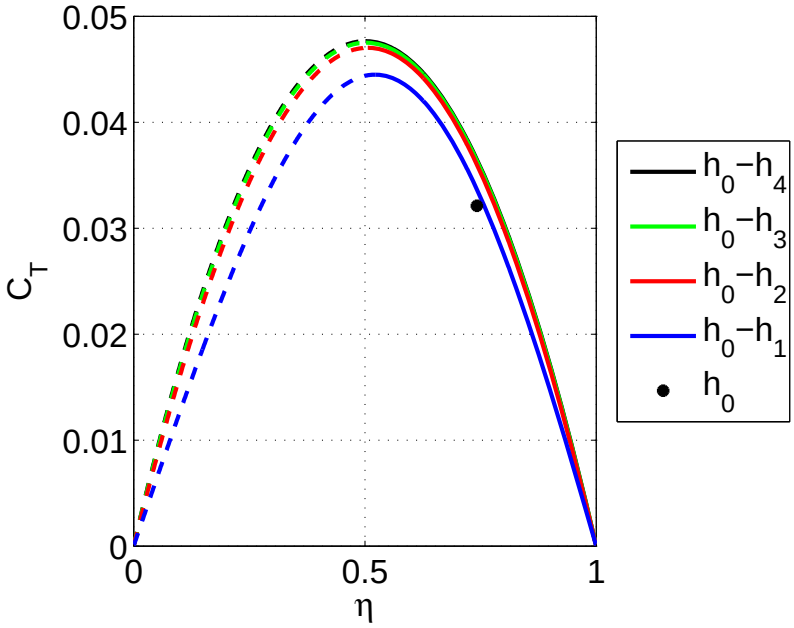

Figure 5.6: Pareto Front for $k = 0.25$ (Magnitude constraint only)

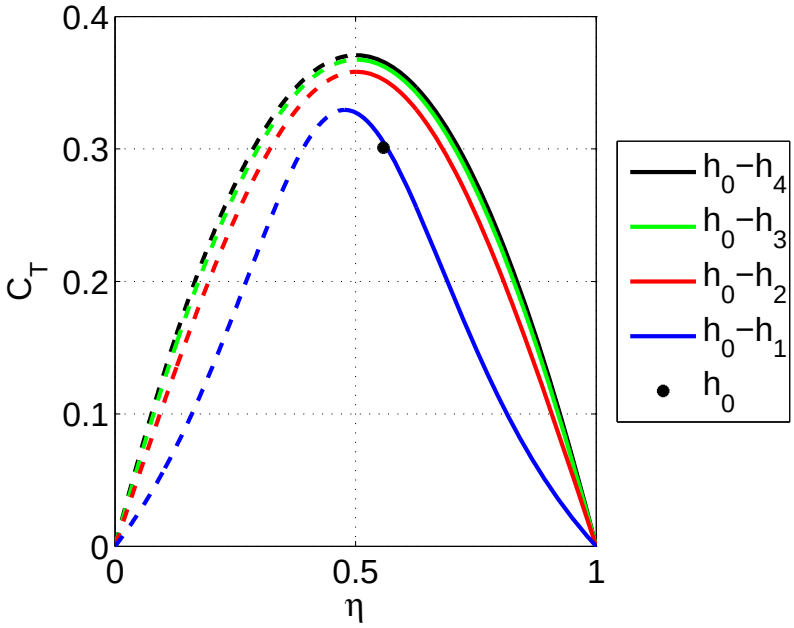

Figure 5.7: Pareto Front for $k = 1$ (Magnitude constraint only)

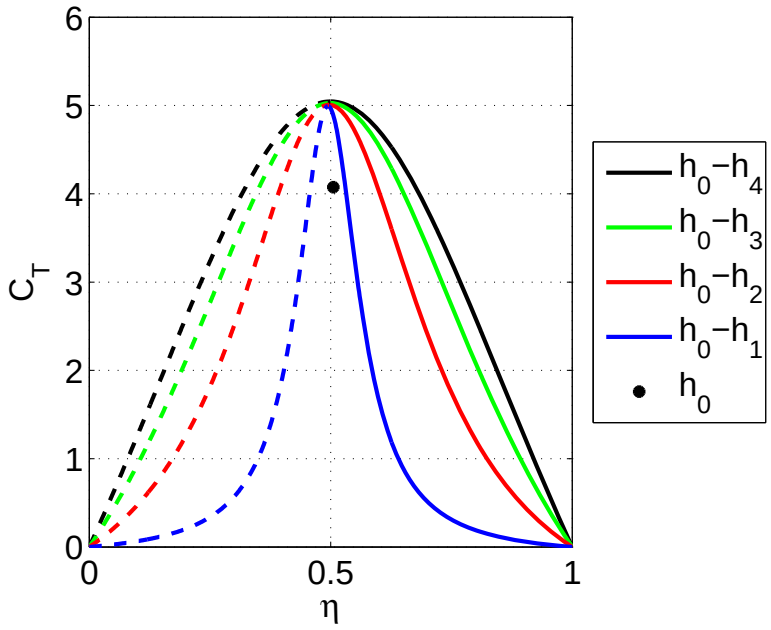

Figure 5.8: Pareto Front for $k = 4$ (Magnitude constraint only)

benefit of adding $\bar{h}_4$ results in a minimal improvement.

As reduced frequency increases, the shape of the Pareto fronts becomes more of a bell shape similar to the case of only a magnitude constraint. This shows that by adding one shape, the maximum thrust increases by a very large amount for high efficiencies, which is seen more clearly in Figure 5.15. However, the $\bar{h}_0 - \bar{h}_2$ Pareto front begins to have a maximum thrust occurring at a lower efficiency while the the $\bar{h}_0 - \bar{h}_3$ Pareto front begins to have a maximum thrust occurring at a higher efficiency.

The Pareto fronts show very useful data on the maximum thrust and efficiency possible, however an investigation of what is physically happening is important. Figure 5.13 shows the stroke-averaged work done by the structure, thrust, and the wake at a reduced frequency of $k = 4$ and a value of thrust equal to that generated by plunge at $k = 4$ as a function of the number of design variables. Essentially, this is showing how the three work terms change as one moves to the right from one Pareto front to the next for a single value of thrust. It can be seen that the total work done by the structure for an optimal solution is decreasing as the number of design variables (and efficiency) increases. Since the work due to

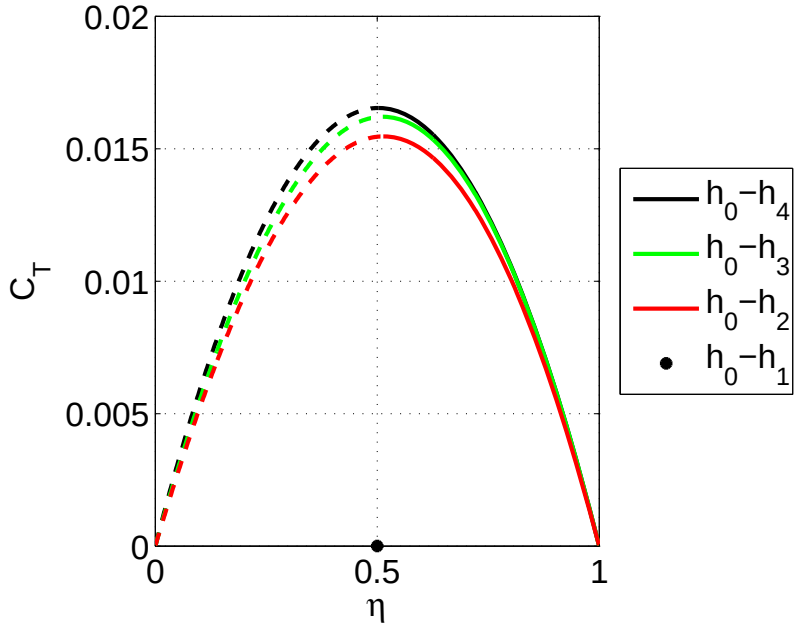

Figure 5.9: Pareto Front for $k = 0.01$ (Magnitude and leading edge suction constraint)

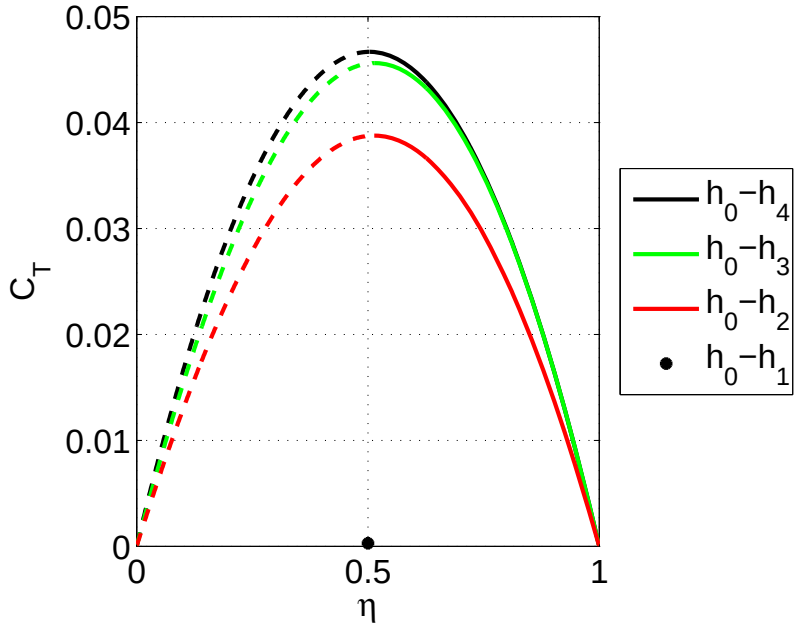

Figure 5.10: Pareto Front for $k = 0.25$ (Magnitude and leading edge suction constraint)

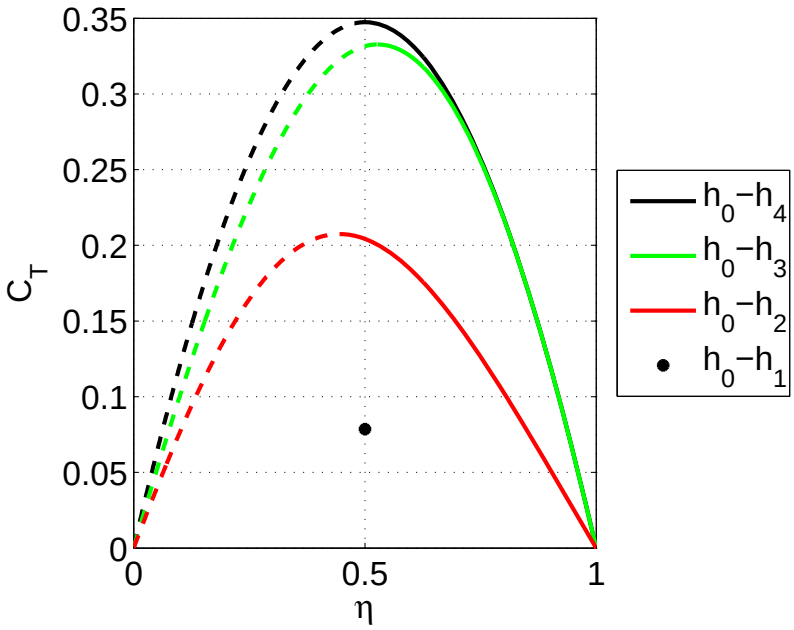

Figure 5.11: Pareto Front for $k = 1$ (Magnitude and leading edge suction constraint)

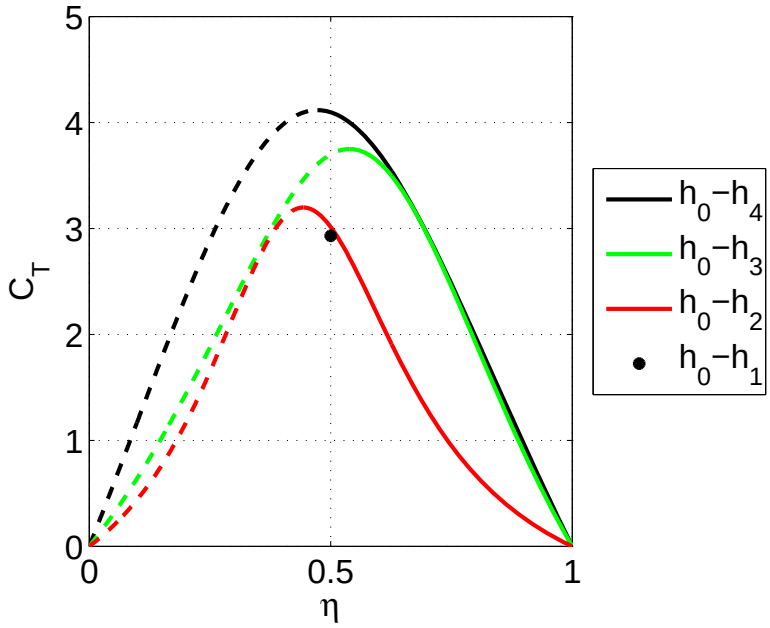

Figure 5.12: Pareto Front for $k = 4$ (Magnitude and leading edge suction constraint)

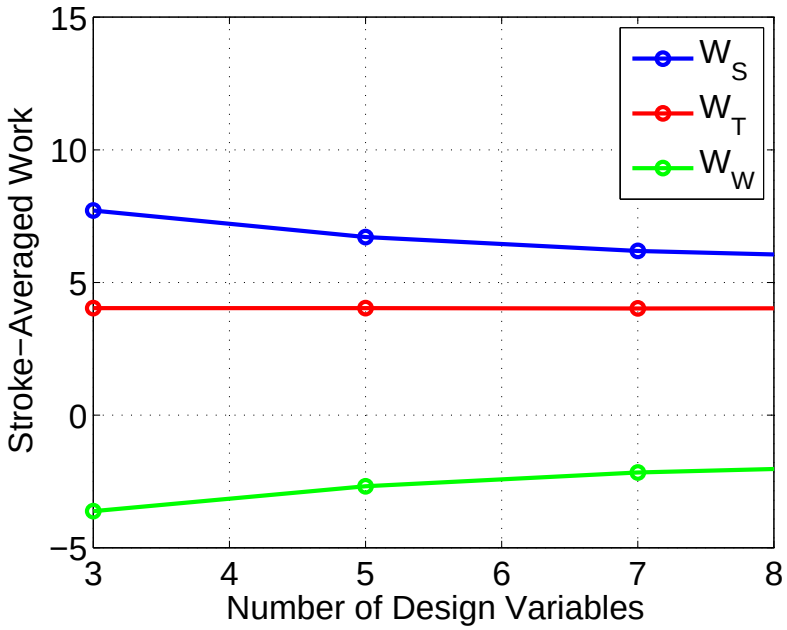

Figure 5.13: Stroke-averaged work for $T = T_{h_0}$ at $k = 4$

thrust must remain the same to maintain the same value of thrust, the only way to increase efficiency is to decrease the total work done by the structure. As a result, the magnitude of work contributing to the wake decreases, which is expected based on conservation of energy, Eq. 4.9. Therefore, it can be seen that to obtain maximum thrust at high efficiency, the total work done by the structure must decrease if maintaining the same value of thrust is desired.

Figure 5.14 shows the maximum thrust achievable when the efficiency is constrained to be 75% with no leading edge constraint. The magnitude of the thrust is less than the maximum, but the percent increase by adding just one shape is quite significant. Likewise, adding a third and fourth shape led to even more thrust. Constraining the efficiency to be 60%, 70%, 80% and 90% led to similar results.

Figure 5.15 shows the increase in maximum thrust at 75% efficiency when the leading edge suction is constrained. The results are similar to the magnitude constraint only case. There is no thrust due to pitch and plunge at 75% efficiency; it occurs at 50% efficiency. However, thrust can be generated with 75% efficiency for three or more shapes. The addition of $\bar{h}_3$ led to a significant increase in the maximum thrust, but adding $\bar{h}_4$ only increased the

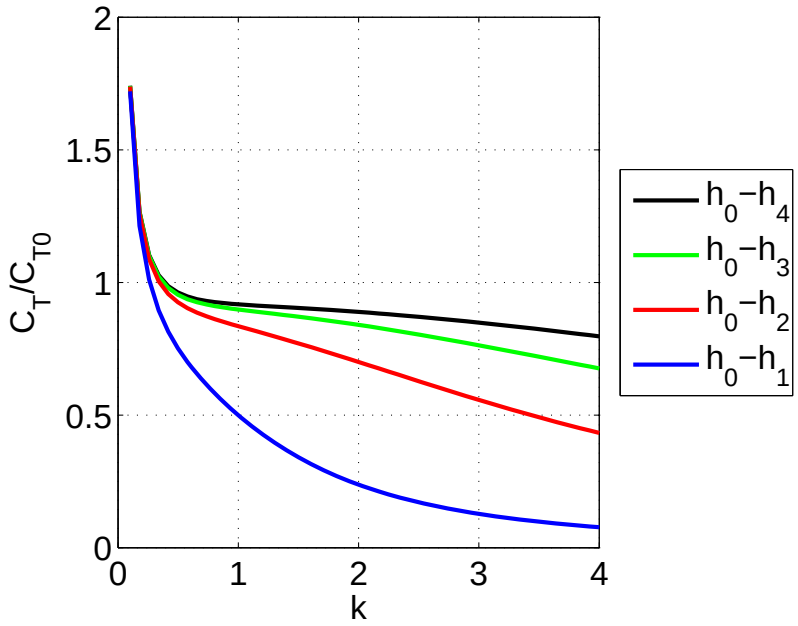

Figure 5.14: Thrust for $\eta = 75\%$ (Magnitude constraint)

thrust a minimal amount.

Figures 5.16 and 5.17 approach the problem from a different perspective. These figures show the maximum efficiency for a desired value of thrust. This could be very useful from a design perspective, showing the number of deformation shapes required to achieve the desired efficiency for given required thrust. Figure 5.16 shows the efficiency for the case of required thrust equal to half the thrust due to plunge only. The addition of deformation shapes leads to a significant increase in the efficiency achievable. The largest increase in efficiency occurs at low reduced frequencies.

As reduced frequency approaches zero, the efficiency approaches 100%. The efficiency for plunge only is shown by Garrick[2] to be $(F^2 + G^2)/F$. For reduced frequency of 0 the efficiency of plunge is 100% while for large reduced frequencies it approaches 50%. The efficiency for all shapes approaches 50% as well. This is more easily seen in the Pareto fronts shown in Figures 5.5 through 5.12.

Figure 5.17 shows the efficiency for the case of leading edge suction constraint. Similar to the magnitude only constraint, the addition of deformation shapes leads to an increase in

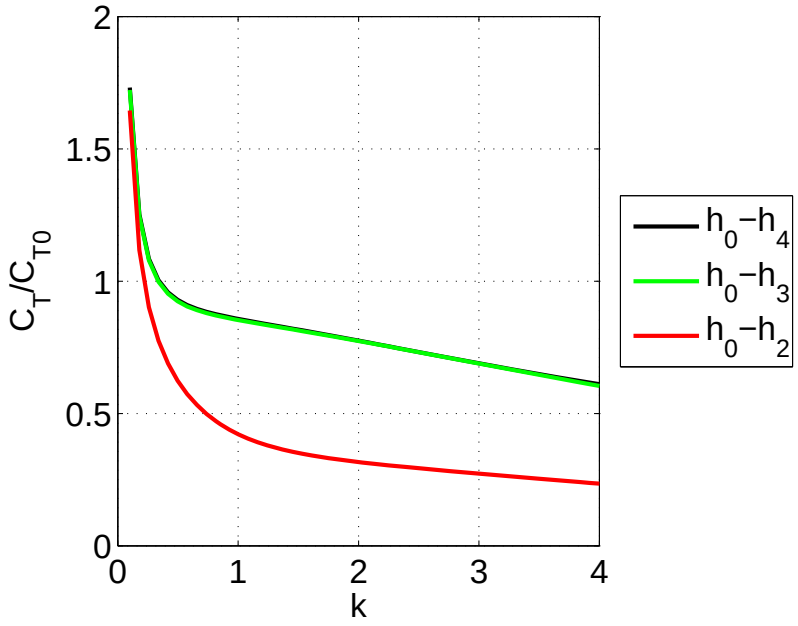

Figure 5.15: Thrust for $\eta = 75\%$ (Magnitude and leading edge suction constraint)

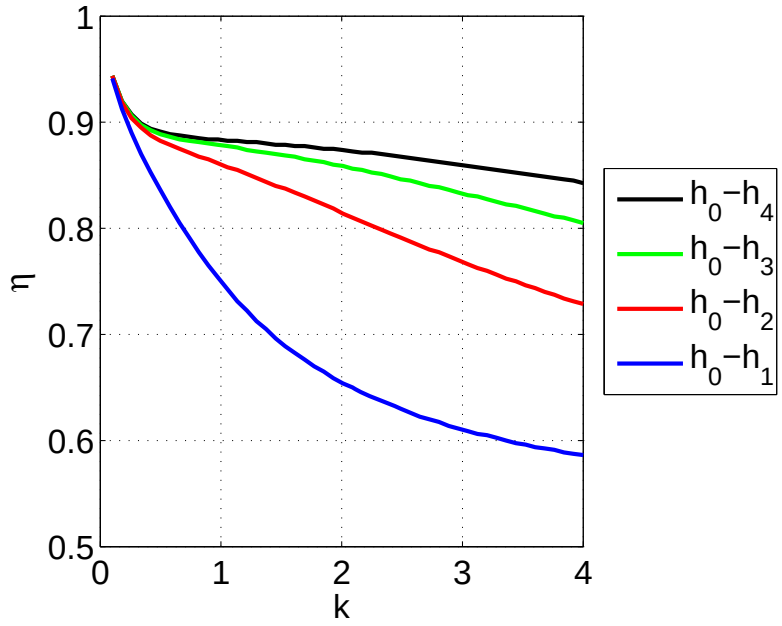

Figure 5.16: Efficiency for $T = T_{h_0}/2$ (Magnitude Constraint)

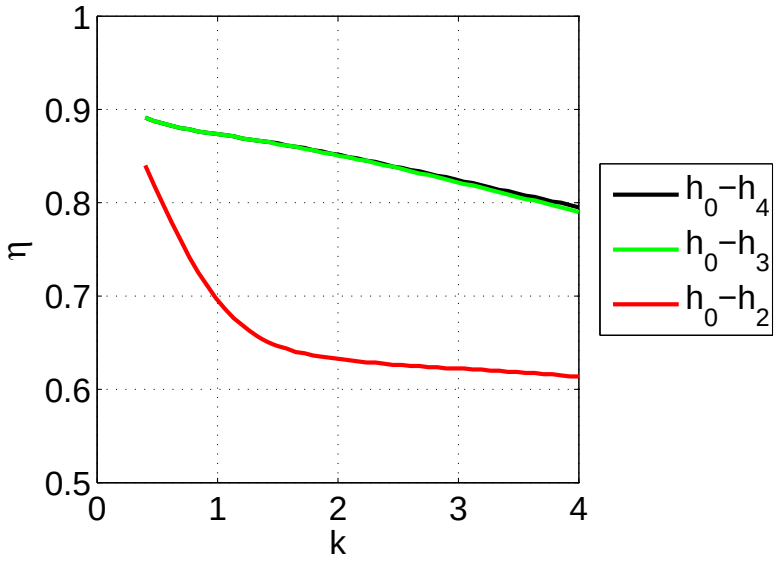

Figure 5.17: Efficiency for $T = T_{h_0}/2$ (Magnitude and leading edge suction constraint)

efficiency. Similar to the increase in thrust by adding deformation shapes, the addition of $\bar{h}_3$ leads to a significant increase in efficiency. However, the addition of $\bar{h}_4$ only leads to a minimal increase in efficiency. At low reduced frequencies, the percent increase is quite large because the efficiency of pitch and plunge only is 50%, and the maximum efficiency for zero reduced frequency is 100%. As reduced frequency approaches infinity, the efficiency for all shapes approaches 50%.

These multi-objective optimization results for thrust and efficiency show a very important result. Flapping wing MAV's that require a specific value of thrust for flight can increase the maximum achievable efficiency by allowing the wing to deform in more complex shapes. In other words allowing a wing deforming in quadratic camber to also deform with cubic and quartic camber can increase the efficiency given the correct magnitude and phase of the additional deformation shapes. Likewise, if a specific value of efficiency is required for flight, allowing the wing to deform in higher order camber shapes leads to more thrust.

5.3 Airfoil Shape and Pressure Distribution for Maximum Thrust

The maximum thrust for situations where the magnitude of the motion is constrained and where the leading edge suction is also constrained have been calculated. The shape of the airfoil is also important to discuss. The magnitude constraint was applied to the root mean square of the design variable. However, no constraint was placed on the gradient of the pressure. If the maximum thrust requires a shape with very large changes in pressure, flow separation will occur due to the large negative pressure gradient on the airfoil.

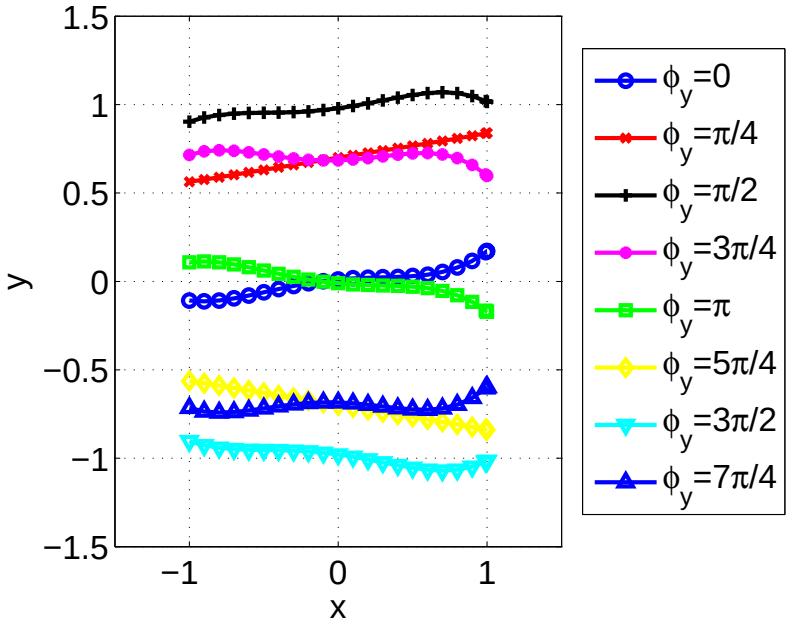

Figure 5.18: Airfoil Shape for ($k = 0.1$) (Magnitude constraint)

Figures 5.18 and 5.19 show the airfoil deformation shape and pressure distribution for maximum thrust at a reduced frequency of 0.1. The angle ϕ corresponds to the phase of the motion relative to the plunge over one oscillation. Therefore eight different instances of the airfoil shape are shown in each figure. The shape consists of mainly plunge with a small amount of pitching and deformation. Therefore, the maximum thrust is generated mostly by leading edge suction when only the magnitude of the motion is constrained. The

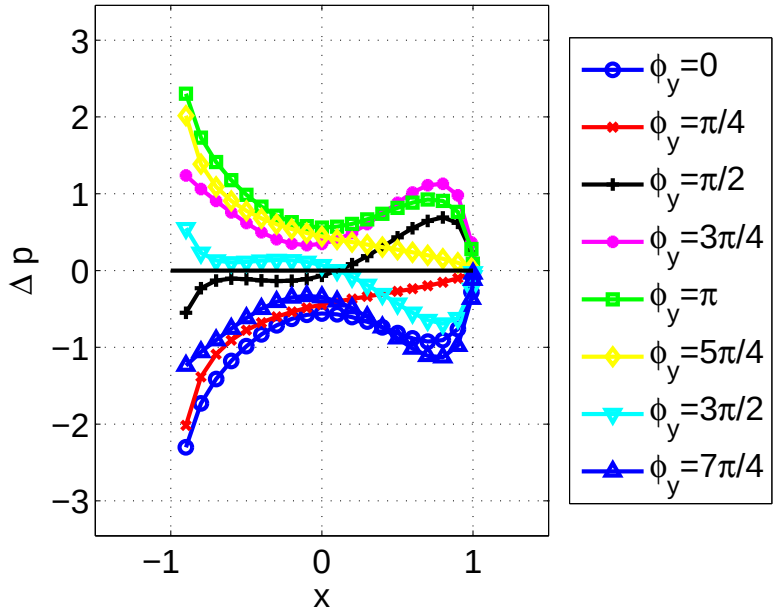

Figure 5.19: Pressure Distribution for ($k = 0.1$) (Magnitude constraint)

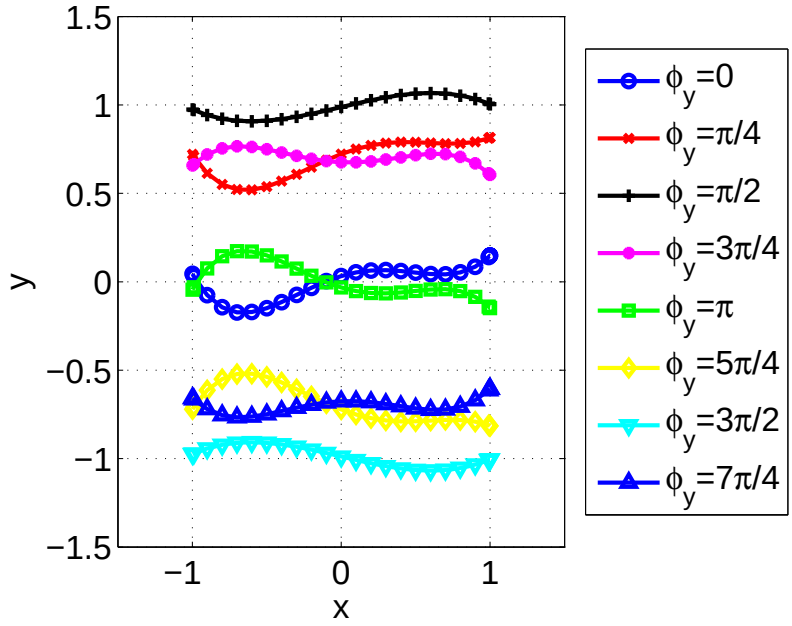

Figure 5.20: Airfoil Shape for ($k = 0.1$) (Magnitude and leading edge suction constraint)

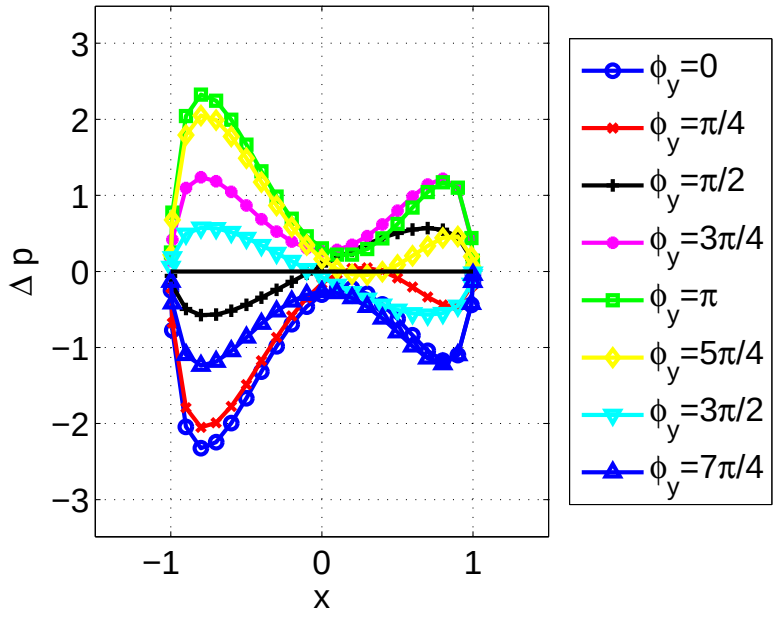

Figure 5.21: Pressure Distribution for ($k = 0.1$) (Magnitude and leading edge suction constraint)

pressure distribution shows that pressure approaches infinity at the leading edge and zero at the trailing edge (Kutta condition). This value of pressure shows that there will be leading edge separation, which violates the assumptions of the deformable thin airfoil theory.

However, Figures 5.20 and 5.21 show the deformation shape and pressure distribution for the maximum thrust when the leading edge suction is constrained. The deformation shape looks slightly different, but still consists of mainly plunge. This implies that the motion in addition to plunge produces a leading edge vorticity which is equal and opposite to the flow generated by plunge, while at the same time producing a thrust due to pressure. The pressure difference at the leading edge is zero, which means that the motion required to generate maximum thrust will not generate leading edge separation. However, there is a large negative pressure gradient generated which could lead to separation away from the leading edge. Accounting for this effect will require more advanced separation models.

Figures 5.22 through 5.25 show the same results for a high reduced frequency of 4. The deformation shape for the motion constraint shows results similar to the case of the reduced frequency of 0.1. However, the motion contains less plunge and more pitch and

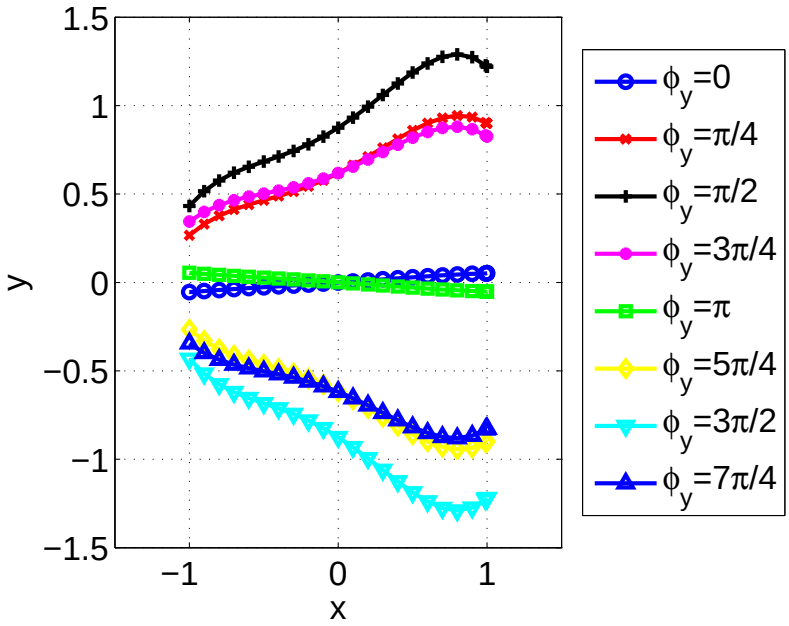

Figure 5.22: Airfoil Shape for ($k = 4$) (Magnitude constraint)

deformation. The phase of the pitch relative to the plunge is also different. This is a result of the phase changes due to $C(k)$ and k^2 terms in the thrust which comes from the lag in pressure and airfoil acceleration respectively. The airfoil shape for the case of both magnitude and leading edge suction constrained contains much more deformation. Also, the phase of the pitch motion relative to plunge is different. However, the pressure gradient is lower along the airfoil as compared to the case of reduced frequency of 0.1 in both cases. This is an interesting result because it shows that at larger reduced frequencies, there is a possibility that separation may not occur over much of the airfoil during most of the oscillation. The airfoil shape and pressure distribution results are similar when the efficiency is constrained to higher values.

It was shown that by constraining the deformation magnitude, a maximum thrust can be calculated. The maximum thrust increases by expanding the design space with more deformation shapes. A second constraint was placed on the thrust efficiency to generate a Pareto front for thrust and thrust efficiency. It was shown that adding higher order deformation shapes to the design space leads to an increase in the maximum thrust for a given

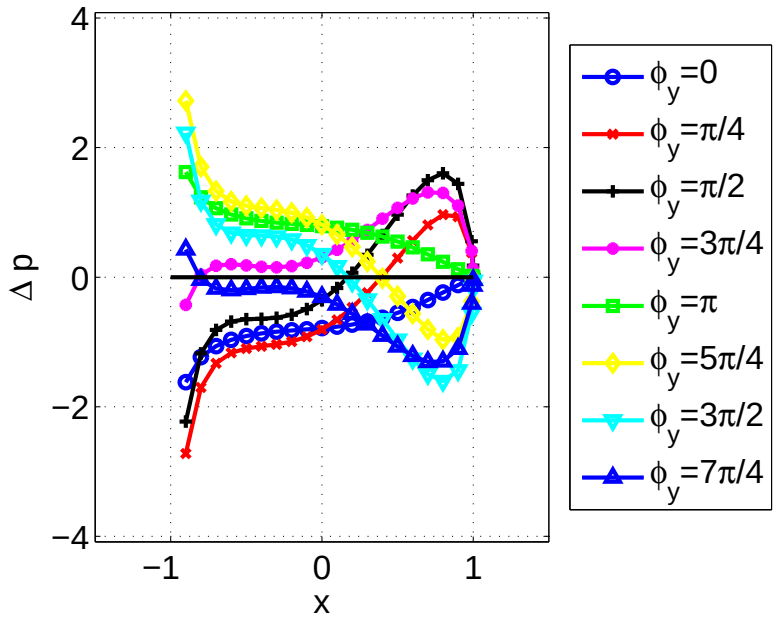

Figure 5.23: Pressure Distribution for ($k = 4$) (Magnitude constraint)

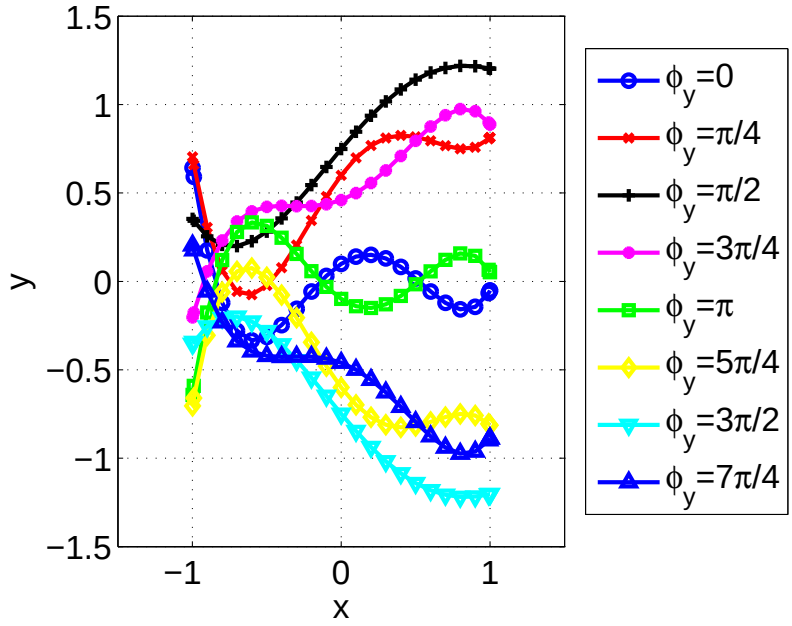

Figure 5.24: Airfoil Shape for ($k = 4$) (Magnitude and leading edge suction constraint)

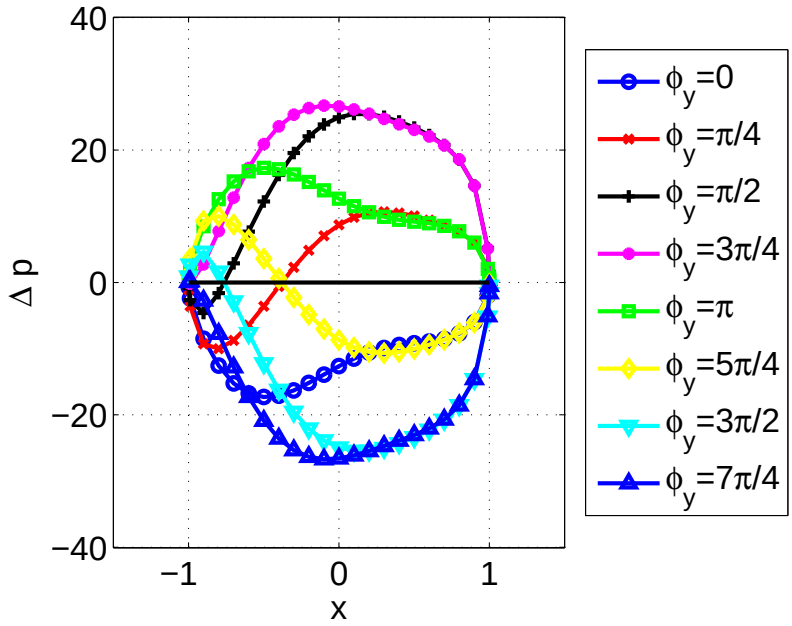

Figure 5.25: Pressure Distribution for ($k = 4$) (Magnitude and leading edge suction constraint)

efficiency and increase of efficiency for a given thrust. At high reduced frequencies, the Pareto fronts become like a bell shape, thus leading to very low maximum thrust, at high efficiencies.

A third constraint was used to constrain the leading edge suction. This allowed for the maximum thrust and efficiency to be found for a case where there was no leading edge suction. It was shown that using this constraint forced the pressure difference to be zero at the leading edge of the airfoil, ensuring no leading edge separation. Maximum thrust with this constraint was found to be smaller than, but on the order of the thrust obtained without this constraint.

The use of a magnitude constraint and a leading edge suction constraint gives results for flow situations which satisfy the assumptions used to derive the deformable thin airfoil theory. The results presented thus provide detailed airfoil shapes required to generate maximum thrust and efficiency for flapping wings without separation.

Chapter 6

Membrane Wing Aeroelasticity

The optimized wing deformation presented in Chapter 5 is a very useful design tool for MAV wings. However, deformations are not prescribed, but a result of the flapping motion. Optimizing the deformation shape only tells how the wing should deform to generate maximum stroke-averaged thrust, not how the wing should be designed. Flapping wing MAVs have thin lightweight wings, which behave as membranes. In a realistic system the properties of the membrane itself are the design variables. Therefore the development and optimization of the aeroelastic system is required to generate a feasible wing design. The aeroelastic system is derived using the unsteady deformable thin airfoil theory as forcing in a membrane vibration problem. The aerodynamic model is only two dimensional, however using a strip theory approximation, the the two dimensional forcing can be used in a three dimensional problem. The following sections derive the aeroelastic membrane vibration problem in two dimensions by assuming a modeshape in the spanwise direction and using a weighted residual method to reduce the problem to a two dimensional problem similar to a string vibration situation.

6.1 General Equations for Membrane Vibration

Consider a membrane wing in an airflow as shown in Figure 6.1. The membrane can be presstressed in spanwise, chordwise and shear directions. The deflection, $W(X, Y, t)$, is the

deformation which includes rigid body motion (pitch and plunge) along with the membrane deformation. The aerodynamic forcing, $\Delta P(X,Y,t)$, is effective load due to prescribed rigid body motion as well as membrane deformation. The equation of motion for this aeroelastic system is given as,

$$\begin{aligned}&\frac{\partial}{\partial X}\left[S_x(X,Y)\frac{\partial W(X,Y,t)}{\partial X}\right]+\frac{\partial}{\partial X}\left[S_{xy}(X,Y)\frac{\partial W(X,Y,t)}{\partial Y}\right]+\\&\frac{\partial}{\partial Y}\left[S_{xy}(X,Y)\frac{\partial W(X,Y,t)}{\partial X}\right]+\frac{\partial}{\partial Y}\left[S_y(X,Y)\frac{\partial W(X,Y,t)}{\partial Y}\right]+\\&\Delta P(X,Y,t)=\rho_w(X,Y)t_w(X,Y)\frac{\partial^2 W(X,Y,t)}{\partial t^2}\end{aligned} \tag{6.1}$$

where $\rho_w(X,Y)$ and $t_w(X,Y)$ are the density and thickness of the membrane, and $S_x(X,Y)$, $S_y(X,Y)$ and $S_{xy}(X,Y)$ are the normal and shear prestresses in the membrane. Eq. 6.1 is subject to the boundary conditions and initial conditions given as,

$$\begin{gathered}W(X,0,t)=0\quad W(X,s,t)=0\quad W(-b,Y,t)=0\quad W(b,Y,t)=0\\W(X,Y,0)=w_0\quad \frac{\partial W}{\partial t}(X,Y,0)=v_0\end{gathered} \tag{6.2}$$

The change in pressure, $\Delta P(X,Y,t)$, can be calculated using a strip theory approximation based on Eq. 3.37 from the two dimensional aerodynamic theory described in the earlier section. The strip theory assumption neglects three dimensional aerodynamic effects including interactions between various chordwise strips and tip effects.

Assuming there is no shear prestress, the chordwise prestress, $S_x(X,Y)$ is constant, the spanwise prestress is only a function of chord location, X, and the wing density and thickness are constant, the membrane vibration equation reduces to a much simpler form.

$$S_x\frac{\partial^2 W(X,Y,t)}{\partial X^2}+S_y(X)\frac{\partial^2 W(X,Y,t)}{\partial Y^2}+\Delta P(X,Y,t)=\rho_w t_w\frac{\partial^2 W(X,Y,t)}{\partial t^2} \tag{6.3}$$

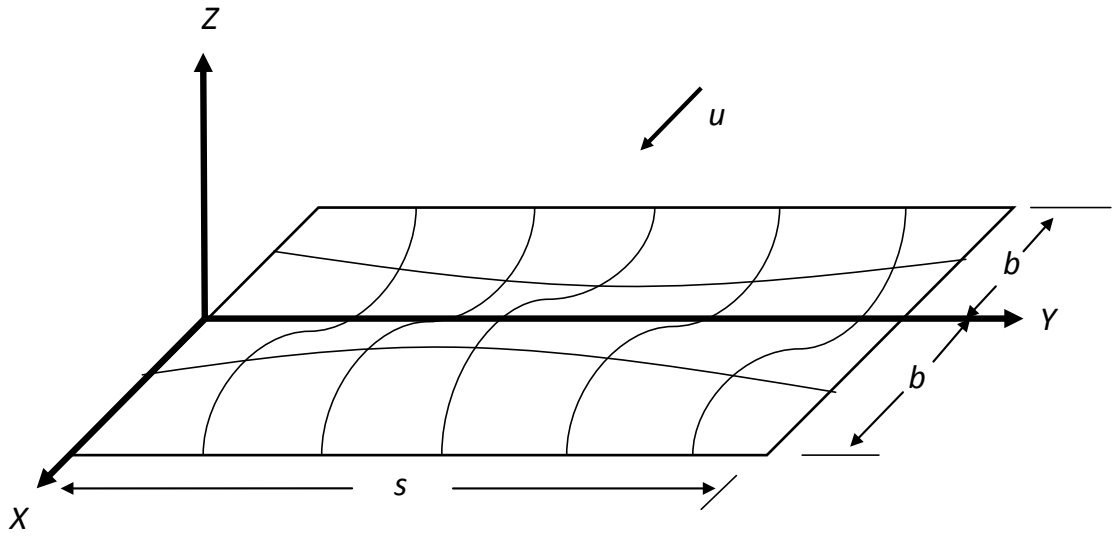

Figure 6.1: Membrane wing in air

These assumptions were made to pose the membrane vibration problem as a realistic two dimensional problem. The shear prestress was ignored to simplify the problem. The chordwise prestress would normally not vary with chord in a membrane. Varying the chordwise prestress as a function of span is not helpful because the aerodynamics will be approximated with strip theory. However, varying the spanwise prestress as a function of chord would result in interesting vibration response in the chordwise direction.

6.2 Reduction of Membrane Vibration Theory to Two Dimensions

The aeroelastic problem of Eq. 6.3 can be reduced to a much simpler form by assuming the form of the vibration response in the spanwise direction. By making such an assumption, the spanwise variable, Y, can be completely eliminated from the membrane problem. This will reduce the three dimensional membrane aeroelasticity problem to a two dimensional problem similar to string vibration.

Consider a wing with prescribed plunging and pitching. Let us discretize the mem-

brane deformation in spanwise direction using sinusoids. Furthermore, let us assume that only one spanwise shape is sufficient to represent the the spanwise deformation variation. The assumed wing motion including rigid body motion can be represented in the following form.

$$W(X,Y,t) = A_0(t) + A_1(t)X + W_D(X,t)\sin(\frac{\pi Y}{s}) \tag{6.4}$$

The aerodynamics from strip theory using this assumed modeshape will result in

$$\Delta P(X,Y,t) = \Delta P_R(X,t) + \Delta P_D(X,t)\sin(\frac{\pi Y}{s}) \tag{6.5}$$

where ΔP_D and ΔP_R are the pressure due to airfoil deformation and rigid body motion respectively.

Substituting the assumed solution and aerodynamics into the membrane vibration problem results in

$$\begin{aligned} S_x \sin(\frac{\pi Y}{s})\frac{\partial^2 W_D(X,t)}{\partial X^2} - \frac{\pi^2}{s^2}S_y(X)\sin(\frac{\pi Y}{s})W_D(X,t) + \Delta P_D(X,t)\sin(\frac{\pi Y}{s}) + \\ \Delta P_R(X,t) = \rho_w t_w \left(\frac{\partial^2 A_0(t)}{\partial t^2} + \frac{\partial^2 A_1(t)}{\partial t^2}X + \frac{\partial^2 W_D(X,t)}{\partial t^2}\sin(\frac{\pi Y}{s})\right) \end{aligned} \tag{6.6}$$

The spanwise variable can be eliminated using the weighted residual method. Using the assumed spanwise modeshape as the weight and integrating over the span results in

$$\begin{aligned}\int_0^s \Bigg[S_x \sin(\frac{\pi Y}{s}) \frac{\partial^2 W_D(X,t)}{\partial X^2} - \frac{\pi^2}{s^2} S_y(X) \sin(\frac{\pi Y}{s}) W_D(X,t) \\ + \Delta P_D(X,t) \sin(\frac{\pi Y}{s}) + \Delta P_R(X,t) \Bigg] \sin(\frac{\pi Y}{s}) dY \\ = \int_0^s \left[\rho_w t_w \left(\frac{\partial^2 A_0}{\partial t^2} + \frac{\partial^2 A_1}{\partial t^2} x + \frac{\partial^2 W_D(X,t)}{\partial t^2} \sin(\frac{\pi Y}{s}) \right) \right] \sin(\frac{\pi Y}{s}) dY\end{aligned} \tag{6.7}$$

The resulting equation looks exactly like the string vibration equation with one extra term.

$$\begin{aligned}S_x \frac{\partial^2 W_D(X,t)}{\partial X^2} - \frac{\pi^2}{s^2} S_y(X) W_D(X,t) + \Delta P_D(X,t) + \frac{4}{\pi} \Delta P_R(X,t) \\ = \rho_w t_w \frac{\partial^2 W_D(X,t)}{\partial t^2} + \frac{4 \rho_w t_w}{\pi} \left(\frac{\partial^2 A_0(t)}{\partial t^2} + \frac{\partial^2 A_1(t)}{\partial t^2} X \right)\end{aligned} \tag{6.8}$$

The reduced aeroelastic membrane equation can be further simplified by nondimensionalizing. Making substitutions of $X = xb$, $W_D = wb$, $A_0 = a_0 b$, $A_1 = a_1$, $\tau = \omega t$, $\Delta P(x,k) = \frac{1}{2} \rho_a u^2 \Delta p(x,k)$and dividing by $\rho_w t_w b \omega^2$, the equation becomes

$$\begin{aligned}\frac{S_x}{\rho_w t_w b^2 \omega^2} \frac{\partial^2 w(x,\tau)}{\partial x^2} - \frac{S_y(x)}{\rho_w t_w s^2 \omega^2} \pi^2 w(x,\tau) + \frac{1/2 \rho_a u^2}{\rho_w t_w b \omega^2} \Delta p_D(x,\tau) + \\ \frac{4}{\pi} \frac{1/2 \rho_a u^2}{\rho_w t_w b \omega^2} \Delta p_R(x,\tau) = \frac{\partial^2 w(x,\tau)}{\partial \tau^2} + \frac{4}{\pi} \left(\frac{\partial^2 a_0(\tau)}{\partial \tau^2} + \frac{\partial^2 a_1(\tau)}{\partial \tau^2} x \right)\end{aligned} \tag{6.9}$$

Now assume that the prescribed motion is harmonic with the reference frequency, ω. Since the problem is linear, the solution can be written

$$\begin{aligned} w(x,\tau) &= w(x)e^{i\tau} \\ a_0(\tau) &= \bar{a}_0 e^{i\omega t} = \bar{a}_0 e^{i\tau} \\ a_1(\tau) &= \bar{a}_1 e^{i\omega t} = \bar{a}_1 e^{i\tau} \end{aligned} \tag{6.10}$$

Now we can use the frequency domain aerodynamic model derived in the earlier section.

$$\Delta p(x,\tau) = \Delta\bar{p}(x,k)e^{i\tau} \tag{6.11}$$

Thus, the frequency-domain, nondimensional, aeroelastic membrane equation is

$$\begin{aligned} \bar{w} + q_x\frac{\partial^2\bar{w}}{\partial x^2} - \pi^2 q_y(x)\bar{w} + \frac{1}{\sigma k^2}\Delta\bar{p}_D(x,k,\bar{w}) \\ = -\frac{4}{\pi}\left(\frac{1}{\sigma k^2}\Delta\bar{p}_R(x,k,\bar{a}_0,\bar{a}_1) + \bar{a}_0 + \bar{a}_1 x\right) \end{aligned} \tag{6.12}$$

The nondimensional stiffness terms are

$$\begin{aligned} q_x &= \frac{S_x}{\rho_w t_w b^2\omega^2} \\ q_y(x) &= \frac{S_y(x)}{\rho_w t_w s^2\omega^2} \end{aligned} \tag{6.13}$$

which are related to the ratio of membrane natural frequencies to excitation frequency. For example, for constant q_y, we have $\frac{\omega_{mn}}{\omega} = \pi\sqrt{m^2 q_x + n^2 q_y}$, where ω_{mn} are the natural frequencies of a rectangular membrane.

σ is the mass ratio which is

$$\sigma = \frac{\rho_w t_w}{1/2 \rho_a b} \tag{6.14}$$

It should noted that this mass ratio is a product of nondimensionalizing the derived equations of motion. It is not the same mass ratio typically used in aeroelasticity. The relationship between the membrane wing mass ratio used in this work and the classic mass ratio is

$$\sigma = 2\pi\mu \tag{6.15}$$

where μ is the classic mass ratio.

6.3 Solution to Membrane Vibration Problem via the Assumed Modes Method

The most convenient solution technique is the assumed modes method. The assumed modes solution is

$$w(x,\tau) = \sum_{l=2}^{N-1} z_l(x) a_l(\tau) \tag{6.16}$$

where $z_l(x)$ are the assumed modeshapes, $a_l(\tau)$ are the magnitudes of each modeshape and N is the total number of assumed modeshapes including the two rigid modes. The membrane vibration problem now becomes

$$\sum_{l=2}^{N-1} z_l(x)\bar{a}_l + q_x \sum_{l=2}^{N-1} \frac{\partial^2 z_l(x)}{\partial x^2}\bar{a}_l - \pi^2 q_y(x) \sum_{l=2}^{N-1} z_l(x)\bar{a}_l + \frac{1}{\sigma k^2}\Delta\bar{p}_D(x,k,\bar{a}_l) = -\frac{4}{\pi}\left(\frac{1}{\sigma k^2}\Delta\bar{p}_R(x,k,\bar{a}_0,\bar{a}_1) + \bar{a}_0 + \bar{a}_1 x\right) \tag{6.17}$$

Using the Galerkin method the continuous system can be reduced to a series of coupled linear equations for $N-2$ assumed modeshapes. Using the assumed modeshape as the weight and choosing a functional form of the normalized spanwise tension, $q_y(x)$, the equation can be rewritten

$$\left(\left[M\right] - \left[K(q_x, q_y(x))\right] + \frac{1}{\sigma k^2}\left[P_D(k)\right]\right)\left\{\bar{a}\right\} = -\frac{4}{\pi}\left(\frac{1}{\sigma k^2}\left[P_R(k)\right] + \left[F_I\right]\right)\left\{\bar{a}\right\} \tag{6.18}$$

where the mass, stiffness and inertial forces are

$$\begin{aligned}
\left[M\right] &= \int_{-1}^{1} z_k(x) z_l(x) dx \\
\left[K\right] &= -\int_{-1}^{1} \left[q_x \frac{\partial^2 z_l(x)}{\partial x^2} z_k(x) - q_y(x)\pi^2 z_k(x) z_l(x)\right] dx \\
\left[F_I\right] &= \int_{-1}^{1} z_l(x) z_k(x) dx
\end{aligned} \tag{6.19}$$

where the indices range are $2 \leq k \leq N-1$, $2 \leq l \leq N-1$ and $0 \leq m \leq 1$, $\left[P_D\right]$ and $\left[P_R\right]$ give the generalized forces corresponding to the structural generalized coordinates due to deformation and rigid body motion respectively.

The pressure difference, Eq. 3.37, was derived in the frequency domain using the

Chebychev polynomials. However, these polynomials do not satisfy the boundary conditions given in Eq. 6.2. For structural representation we could use sinusoids as assumed modes but instead we use orthogonal polynomials which satisfy boundary conditions. Polynomials are convenient because the basis functions from the aerodynamic theory are also polynomials and an exact transformation between the two sets can be obtained.

6.4 Orthogonal Polynomials for Membrane Vibration Problem

The set of assumed modes can be anything as long as they satisfy the boundary conditions to the problem. A simple way to generate these is developing orthogonal polynomials that satisfy the boundary conditions. The reduced membrane equation for two dimensions has boundaries at -1 and 1. Therefore the first modeshape can be determined by

$$\begin{aligned} z_2(x) &= c_2x^2 + c_1x + c_0 \\ z_2(-1) &= 0 \\ z_2(1) &= 0 \end{aligned} \tag{6.20}$$

where the modeshape is denoted z_2 because the first two shapes z_0 and z_1 are the rigid body motion (plunge and pitch).

This gives a polynomial shape in terms of one coefficient, essentially a scaling factor. Choosing this coefficient to be 1 is sufficient. The higher order modeshapes are found in the exact same way, however an orthogonality condition is applied.

$$z_i(x) = \sum_{m=0}^{i} c_m x^m \quad for \quad i \geq 3 \tag{6.21}$$

$$\tag{6.22}$$

where,

$$\begin{gathered} z_i(-1) = 0 \quad z_i(1) = 0 \\ \int_{-1}^{1} z_i(x) z_j(x) dx = 0 \quad for \quad j < 1 \quad \& \quad j > 1 \end{gathered} \tag{6.23}$$

The first three modeshapes are

$$\begin{aligned} z_2 &= x^2 - 1 \\ z_3 &= x^3 - x \\ z_4 &= x^4 - \frac{8}{7}x^2 + \frac{1}{7} \end{aligned} \tag{6.24}$$

The transformation between the Chebychev polynomials and the orthogonal polynomials for membrane vibration, Eq. 6.25 is

$$\Big[C\Big] = \begin{bmatrix} 1 & 0 & -\frac{1}{2} & 0 & -\frac{3}{56} \\ 0 & 1 & 0 & -\frac{1}{4} & 0 \\ 0 & 0 & \frac{1}{2} & 0 & -\frac{1}{14} \\ 0 & 0 & 0 & \frac{1}{4} & 0 \\ 0 & 0 & 0 & 0 & \frac{1}{8} \end{bmatrix} \tag{6.25}$$

6.5 Generalized Force Matrices

Consider the aerodynamic theory where the generalized forces are calculated for generalized coordinates corresponding to Chebychev polynomials, the corresponding h_l's, and reduced frequency, k. The pressure difference Eq. 3.37 can be written in the form

$$\Delta\bar{p}(x,k) = \sum_{j=0}^{N-1} \Delta p_j(x,k)\bar{h}_j \tag{6.26}$$

Therefore the generalized forces for motion described by the Chebychev polynomials are

$$\left\{\bar{P}_i\right\} = \sum_{j=0}^{N-1} \int_{-1}^{1} \Delta p_j(x,k)\bar{h}_j T_i(x)dx = \left[P^h(k)\right]\left\{h_j\right\} \tag{6.27}$$

where $\left[P^h\right]$ is a function of only reduced frequency.

Eq. 6.27 gives the generalized forces for generalized coordinates based on the Chebychev polynomials. The structural equations require the generalized forces in terms of the structural assumed modes, Eq. 6.24. Using the transformation Eq. 6.25, the generalized force matrix corresponding to the membrane orthogonal polynomials is

$$\left[P^a\right] = \left[C\right]^T \left[P^h\right] \left[C\right] \tag{6.28}$$

The aerodynamic matrices required for the analysis above are:

$$\begin{aligned} P_D &= P^a_{3-N,3-N} \\ P_R &= P^a_{3-N,1-2} \end{aligned} \tag{6.29}$$

Chapter 7

Analytic Sensitivity Analysis

The convergence of gradient based optimization is significantly improved when the analytic gradients of the objective function(s) and constraints are provided. Thus it is worth deriving the sensitivity of the objectives and constraints with respect to the design space.

7.1 Sensitivity of Stroke-Averaged Thrust with Respect to the Design Variables

The aeroelastic optimization problem is quite nonlinear, but analytic sensitivities can be found and used in the gradient based optimization. Consider the complete membrane deformation problem presented in Chapter 6. The magnitude of the membrane deformations can be obtained from Eq. 6.18 and can be solved to give the deformation shape magnitudes

$$\left\{\bar{a}_l\right\} = -\frac{4}{\pi}\left(\left[M\right] - \left[K(q)\right] + \frac{1}{\sigma k^2}\left[P_D(k)\right]\right)^{-1}\left(\frac{1}{\sigma k^2}\left[P_R(k)\right] + \left[F_I\right]\right)\left\{\bar{a}_m\right\} \tag{7.1}$$

These membrane deformation shape magnitudes can be transformed into the aerodynamic shapes with Eq. 6.25 and the stroke-averaged thrust can then be calculated with Eq. 3.52. However, it can be seen that the design variables are included in the inverse of

a matrix, making the derivatives quite long expressions. Therefore a different approach is used. Taking the derivative of both sides of Eq. 6.18 results in

$$-\frac{\partial}{\partial q}\left(\left[K(q)\right]\right)\left\{\bar{a}_l\right\}+\left(\left[M\right]-\left[K(q)\right]+\frac{1}{\sigma k^2}\left[P_D(k)\right]\right)\left\{\frac{\partial \bar{a}_l}{\partial q}\right\}=0 \tag{7.2}$$

Therefore, the sensitivity of the membrane deformation shape magnitude with respect to the design variables is

$$\left\{\frac{\partial \bar{a}_l}{\partial q}\right\}=\left(\left[M\right]-\left[K(q)\right]+\frac{1}{\sigma k^2}\left[P_D(k)\right]\right)^{-1}\frac{\partial}{\partial q}\left(\left[K(q)\right]\right)\left\{\bar{a}_l\right\} \tag{7.3}$$

The sensitivity of average thrust with respect to the design variables is desired. Therefore the sensitivity of the aerodynamic deformation shapes with respect to the membrane deformation shapes as well as the sensitivity of the stroke-averaged thrust with respect to the aerodynamic deformation shapes are required. The sensitivity of the aerodynamic shape magnitudes with respect to the membrane shape magnitudes is Eq. 6.25. The sensitivity of the stroke-averaged thrust with respect to the aerodynamic shape magnitudes is actually two partial derivatives since the real function, Eq. 3.52, is being differentiated with respect to the complex variable h. Thus, via the chain rule the sensitivity of the stroke-averaged thrust with respect to the tension variables is

$$\frac{\partial T_{avg}}{\partial q}=\frac{\partial T_{avg}}{\partial h}\frac{\partial h}{\partial \bar{a}_l}\frac{\partial \bar{a}_l}{\partial q}+\frac{\partial T_{avg}}{\partial h^*}\frac{\partial h^*}{\partial \bar{a}_l^*}\frac{\partial \bar{a}_l^*}{\partial q} \tag{7.4}$$

where $()^*$ represents to complex conjugate. The derivatives of the stroke-averaged thrust with respect to h and h^* are

$$\begin{aligned}\frac{\partial T_{avg}}{\partial h} &= \frac{\pi\rho_a u^2 b}{2}\left(\frac{\partial T_{avg}}{\partial h_r} - i\frac{\partial T_{avg}}{\partial h_i}\right)\\ \frac{\partial T_{avg}}{\partial h^*} &= \frac{\pi\rho_a u^2 b}{2}\left(\frac{\partial T_{avg}}{\partial h_r} + i\frac{\partial T_{avg}}{\partial h_i}\right)\end{aligned} \tag{7.5}$$

where h_r and h_i are the real and imaginary components of the aerodynamic deformation terms, h. The stroke-averaged thrust must be written in a real form to calculate the derivatives required.

$$T_{avg} = \pi\rho_a u^2 b \mathrm{Re}\left(\{h_r + ih_i\}\left[T_r + iT_i\right]\{h_r - ih_i\}^T\right) \tag{7.6}$$

where $()^T$ is the non conjugate transpose. Expanding the expression and taking only the real part results in

$$T_{avg} = \frac{\pi\rho_a u^2 b}{2}(\{h_r\}\left[T_r\right]\{h_r\}^T + \{h_r\}\left[T_i\right]\{h_i\}^T - \{h_i\}\left[T_i\right]\{h_r\}^T + \{h_i\}\left[T_r\right]\{h_i\}^T) \tag{7.7}$$

where T_r and T_i are the real and imaginary parts of T_M. The derivatives of stroke-averaged thrust with respect to the real and imaginary components of the airfoil deformation terms are

$$\frac{\partial T_{avg}}{\partial h_r} = \frac{\pi\rho_a u^2 b}{2}\left(\left\{h_r\right\}\left[T_r\right] + \left\{h_r\right\}\left[T_r\right]^T + \left\{h_i\right\}\left[T_i\right]^T - \left\{h_i\right\}\left[T_i\right]\right) \tag{7.8}$$

$$\frac{\partial T_{avg}}{\partial h_i} = \frac{\pi\rho_a u^2 b}{2}\left(\left\{h_r\right\}\left[T_i\right] - \left\{h_r\right\}\left[T_i\right]^T + \left\{h_i\right\}\left[T_r\right]^T + \left\{h_i\right\}\left[T_r\right]\right) \tag{7.9}$$

The magnitude and phase of the pitch motion can also be a variable. Therefore the sensitivity of the average thrust with respect to the real and imaginary parts of the pitch motion are

$$\begin{aligned}\frac{\partial T_{avg}}{\partial a_{1_{Re}}} &= \frac{\partial T_{avg}}{\partial h}\frac{\partial h}{\partial \bar{a}_l}\frac{\partial \bar{a}_l}{\partial a_1}\frac{\partial a_1}{\partial a_{1_{Re}}} + \frac{\partial T_{avg}}{\partial h^*}\frac{\partial h^*}{\partial \bar{a}_l^*}\frac{\partial \bar{a}_l^*}{\partial a_1^*}\frac{\partial a_1 *}{\partial a_{1_{Re}}^*} \\ \frac{\partial T_{avg}}{\partial a_{1_{Im}}} &= \frac{\partial T_{avg}}{\partial h}\frac{\partial h}{\partial \bar{a}_l}\frac{\partial \bar{a}_l}{\partial a_1}\frac{\partial a_1}{\partial a_{1_{Im}}} + \frac{\partial T_{avg}}{\partial h^*}\frac{\partial h^*}{\partial \bar{a}_l^*}\frac{\partial \bar{a}_l^*}{\partial a_1^*}\frac{\partial a_1 *}{\partial a_{1_{Im}}^*}\end{aligned} \tag{7.10}$$

where $\frac{\partial \bar{a}_l}{\partial a_1}$ is the second column of $\frac{\partial \bar{a}_l}{\partial \bar{a}_m}$;

$$\frac{\partial \bar{a}_l}{\partial \bar{a}_m} = -\frac{4}{\pi}\left(\Big[M\Big] - \Big[K(q)\Big] + \frac{1}{\sigma k^2}\Big[P_D(k)\Big]\right)^{-1}\left(\frac{1}{\sigma k^2}\Big[P_R(k)\Big] + \Big[F_I\Big]\right) \tag{7.11}$$

and since $\bar{a}_1 = a_{1_{Re}} + i a_{1_{Im}}$

$$\begin{aligned}\frac{\partial \bar{a}_1}{\partial a_{1_{Re}}} &= \frac{\partial \bar{a}_1}{\partial a_{1_{Re}}^*} = 1 \\ \frac{\partial \bar{a}_1}{\partial a_{1_{Im}}} &= i \\ \frac{\partial \bar{a}_1}{\partial a_{1_{Im}}^*} &= -i\end{aligned} \tag{7.12}$$

Therefore, for the design vector $x = \{a_{1_{Re}}\ a_{1_{Im}}\ q\}$, the sensitivity of stroke-averaged thrust with respect to the design variables is

$$\frac{\partial T_{avg}}{\partial x} = \left\{\frac{\partial T_{avg}}{\partial a_{1_{Re}}}\ \frac{\partial T_{avg}}{\partial a_{1_{Im}}}\ \frac{\partial T_{avg}}{\partial q}\right\} \tag{7.13}$$

7.2 Sensitivity of Normalized Stroke-Averaged Thrust with Respect to the Design Variables

The aeroelastic optimization problem has natural limitations on deformation due to the structure itself. However, in order to compare with the aerodynamic theory it is necessary

to optimize normalized thrust to compare with the aerodynamic optimization. Thrust is a function of deformation squared and therefore an appropriate normalization would be

$$T_{avgnorm} = \frac{T_{avg}}{|\{h\}|^2} \tag{7.14}$$

Therefore the sensitivities of the normalized thrust function with respect to the design variables require additional derivatives. The sensitivity of the normalized stroke-averaged thrust with respect to the design variables can be expanded to

$$\frac{\partial T_{avgnorm}}{\partial q} = \frac{\partial T_{avg}}{\partial q}\frac{1}{|h|^2} + T_{avg}\frac{\partial}{\partial q}\left(\frac{1}{|h|^2}\right) \tag{7.15}$$

The only term which has not been determined thus far is the derivative of the inverse of the norm of h with respect to the design variables. Expanding with the product rule

$$\frac{\partial}{\partial q}\left(\frac{1}{|h|^2}\right) = \frac{\partial}{\partial h}\left(\frac{1}{|h|^2}\right)\frac{\partial h}{\partial \bar{a}}\frac{\partial \bar{a}}{\partial q} + \frac{\partial}{\partial h^*}\left(\frac{1}{|h|^2}\right)\frac{\partial h^*}{\partial \bar{a^*}}\frac{\partial \bar{a^*}}{\partial q} \tag{7.16}$$

The derivative of the inverse of the norm of h with respect to the real and imaginary parts of h are

$$\begin{aligned}\frac{\partial}{\partial h_r}\left(\frac{1}{|h|^2}\right) &= -\left(\frac{2h_r}{|h|^4}\right)\\ \frac{\partial}{\partial h_i}\left(\frac{1}{|h|^2}\right) &= -\left(\frac{2h_i}{|h|^4}\right)\end{aligned} \tag{7.17}$$

and so the derivative of the inverse of the norm of h with respect to h and h^* are

$$\begin{aligned}\frac{\partial}{\partial h}\left(\frac{1}{|h|^2}\right) &= \frac{\pi\rho_a u^2 b}{2}\left(\frac{\partial}{\partial h_r}\left(\frac{1}{|h|^2}\right) - i\frac{\partial}{\partial h_i}\left(\frac{1}{|h|^2}\right)\right)\\ \frac{\partial}{\partial h^*}\left(\frac{1}{|h|^2}\right) &= \frac{\pi\rho_a u^2 b}{2}\left(\frac{\partial}{\partial h_r}\left(\frac{1}{|h|^2}\right) + i\frac{\partial}{\partial h_i}\left(\frac{1}{|h|^2}\right)\right)\end{aligned} \tag{7.18}$$

Thus giving sensitivity of the inverse of the norm of h with respect to the membrane tensions can be calculated

$$\frac{\partial}{\partial q}\left(\frac{1}{|h|^2}\right) = \frac{\partial}{\partial h}\left(\frac{1}{|h|^2}\right)\left[C_{jl}\right]\frac{\partial \bar{a}}{\partial q} + \frac{\partial}{\partial h^*}\left(\frac{1}{|h|^2}\right)\left[C_{jl}\right]\frac{\partial \bar{a}^*}{\partial q} \tag{7.19}$$

Using Eq. 7.19 with Eqs. 7.20 and 7.16 will give the sensitivity of the normalized stroke-averaged thrust with respect to the membrane tension variables.

The sensitivity of the normalized stroke-averaged thrust with respect to the pitch terms is found in the same way and is

$$\begin{aligned}\frac{\partial T_{avgnorm}}{\partial a_{1_{Re}}} &= \frac{\partial T_{avg}}{\partial a_{1_{Re}}}\frac{1}{|h|^2} + T_{avg}\frac{\partial}{\partial a_{1_{Re}}}\left(\frac{1}{|h|^2}\right)\\ \frac{\partial T_{avgnorm}}{\partial a_{1_{Im}}} &= \frac{\partial T_{avg}}{\partial a_{1_{Im}}}\frac{1}{|h|^2} + T_{avg}\frac{\partial}{\partial a_{1_{Im}}}\left(\frac{1}{|h|^2}\right)\end{aligned} \tag{7.20}$$

meaning only the derivative of the inverse of the norm of h with respect to the membrane tensions remains to be calculated, and can be expressed via the chain rule.

$$\begin{aligned}\frac{\partial}{\partial a_{1_{Re}}}\left(\frac{1}{|h|^2}\right) &= \frac{\partial}{\partial h}\left(\frac{1}{|h|^2}\right)\left[C_{jl}\right]\frac{\partial \bar{a}}{\partial \bar{a}_1}\frac{\partial \bar{a}_1}{\partial a_{1Re}} + \frac{\partial}{\partial h^*}\left(\frac{1}{|h|^2}\right)\left[C_{jl}\right]\frac{\partial \bar{a}^*}{\partial a_1^*}\frac{\partial \bar{a}_1^*}{\partial a_{1Re}^*}\\ \frac{\partial}{\partial a_{1_{Im}}}\left(\frac{1}{|h|^2}\right) &= \frac{\partial}{\partial h}\left(\frac{1}{|h|^2}\right)\left[C_{jl}\right]\frac{\partial \bar{a}}{\partial \bar{a}_1}\frac{\partial \bar{a}_1}{\partial a_{1Im}} + \frac{\partial}{\partial h^*}\left(\frac{1}{|h|^2}\right)\left[C_{jl}\right]\frac{\partial \bar{a}^*}{\partial \bar{a}_1^*}\frac{\partial \bar{a}_1^*}{\partial a_{1Im}^*}\end{aligned} \tag{7.21}$$

Therefore, for the design vector $x = \{a_{1_{Re}}\ a_{1_{Im}}\ q\}$, the sensitivity of normalized stroke-averaged thrust with respect to the design variable is

$$\frac{\partial T_{avgnorm}}{\partial x} = \left\{ \frac{\partial}{\partial a_{1_{Re}}} \left(\frac{T_{avg}}{|h|^2} \right) \; \frac{\partial}{\partial a_{1_{Im}}} \left(\frac{T_{avg}}{|h|^2} \right) \; \frac{\partial}{\partial q} \left(\frac{T_{avg}}{|h|^2} \right) \right\} \tag{7.22}$$

7.3 Sensitivity of Various Constraints with Respect to the Design Variables

The sensitivity of the constraint functions with respect to the design variables can also be calculated and are quite useful in improving convergence in gradient based optimization. A total of four constraints have been applied to the aeroelastic optimization:

- Chordwise tension must be greater than zero
- Spanwise tension must everywhere be greater than zero
- The system must never enter aeroelastic divergence
- Propulsive efficiency constrained for epsilon-constraint multi-objective optimization

A constraint on flutter is not necessary when normalized thrust (thrust per unit deformation) is being optimized. The thrust producing mode is a damped mode which extracts energy from the wake and the structure to put into thrust, and will never produce flutter[18].

7.3.1 Sensitivity of Chordwise and Spanwise Tension Constraints with Respect to the Design Variables

The first constraint considered is the chordwise tension. The derivation of the optimization problem presented in Chapter six assumes only one chordwise tension variable. Thus the chordwise tension constraint, denoted c_1, is expressed in a function form as

$$c_1(x) = \bar{q}_x > 0 \tag{7.23}$$

Thus the gradient of the constrain is simply

$$\frac{\partial c_1}{\partial x}(x) = [0\ 0\ 1\ 0\ 0\ 0\ 0\ 0] \tag{7.24}$$

for the full design space of $x = \{a_{1_{Re}}\ a_{1_{Im}}\ q\}$. If the design space is smaller, the gradient is the same as Eq. 7.24, just truncated (for a five variable design space, only the first five terms in the gradient are needed).

The sensitivity of the spanwise tension function being everywhere greater than zero, c_2, requires a more rigorous derivation. The gradient will depend on how many variables are in the design vector. The smallest design vector, three variables, contains only one tension variable. Thus, the spanwise and chordwise tensions are equal making the constraint and gradient

$$c_2(x) = \min\left(\bar{q}_y(x)\right) = \bar{q}_x > 0 \tag{7.25}$$

$$\frac{\partial c_2}{\partial x}(x) = [0\ 0\ 1] \tag{7.26}$$

When the design vector consists on four variables (two tension variables), the constraint and respective gradient become

$$c_2(x) = \min\left(\bar{q}_y(x)\right) = \bar{q}_0 > 0 \tag{7.27}$$

$$\frac{\partial c_2}{\partial x}(x) = [0\ 0\ 0\ 1] \tag{7.28}$$

A design vector consisting of five design variables (three tension variables) is a situation where the spanwise tension can vary linearly with the chord. Therefore the constraint function will have a minimum value at either the leading or trailing edge.

$$c_2(x) = \min\left(\bar{q}_y(x)\right) = \min\left[\bar{q}_y(-1)\ \bar{q}_y(1)\right] > 0 \tag{7.29}$$

$$\begin{aligned} \frac{\partial c_2}{\partial x}(x) =& [0\ 0\ 0\ 1\ 1],\ \text{if } \min\left(\bar{q}_y(x)\right) = \bar{q}_y(1) \\ \frac{\partial c_2}{\partial x}(x) =& [0\ 0\ 0\ 1\ -1],\ \text{if } \min\left(\bar{q}_y(x)\right) = \bar{q}_y(-1) \end{aligned} \tag{7.30}$$

A design vector consisting of six design variables (four tensions variables) is a situation where the spanwise tension can vary quadratically with the chord. Therefore the constraint function can have a minimum value at the leading edge, trailing edge or somewhere in between. This requires the derivation of a function for the minimum value of $\bar{q}_y(x)$. The spanwise tension function for a design vector consisting of six design variables is $\bar{q}_y(x) = \bar{q}_{y0} + \bar{q}_{y1}x + \bar{q}_{y2}x^2$. The minimum or maximum will occur at the value of this function where it's derivative is zero.

$$\bar{q}_{ymin} = \min\left(\bar{q}_y(x)\right) = \bar{q}_{y0} - \frac{\bar{q}_{y1}^2}{2\bar{q}_{y2}} + \frac{\bar{q}_{y1}^2}{4\bar{q}_{y2}} \tag{7.31}$$

However, this value may occur at a value of x that is not in $-1 < +x <= 1$, thus these boundary points must be checked to see whether they are the minimum. Therefore two situations exist to calculate the minimum value of $\bar{q}_{ymin}$.

$$\begin{aligned} c_2(x) &= \min\left(\bar{q}_y(x)\right) = \min\left[\bar{q}_y(-1)\ \bar{q}_y(1)\ \bar{q}_{ymin}\right] > 0 \text{ if } -1 <= x_{min} <= 1 \\ c_2(x) &= \min\left(\bar{q}_y(x)\right) = \min\left[\bar{q}_y(-1)\ \bar{q}_y(1)\right] > 0 \text{ if } -\infty < x_{min} < -1 \text{ or } 1 < x_{min} < \infty \end{aligned} \tag{7.32}$$

Therefore there are three possibilities for the gradient. The gradient would be (i) if $\bar{q}_{ymin} = \bar{q}_y(1)$ and the minimum or maximum of $\bar{q}_y(x)$ occurs in $-\infty < x_{min} < -1$ or $1 < x_{min} < \infty$. The gradient would be (ii) if $\bar{q}_{ymin} = \bar{q}_y(-1)$ and the minimum or maximum of $\bar{q}_y(x)$ occurs in $-\infty < x_{min} < -1$ or $1 < x_{min} < \infty$. The gradient would be (iii) if the minimum or maximum of $\bar{q}_y(x)$ occurs in $-1 <= x_{min} <= 1$ and the value of $\bar{q}_{ymin}$ is smaller than both $\bar{q}_y(1)$ and $\bar{q}_y(-1)$.

$$\begin{aligned} (i)\ \ & \frac{\partial c_2}{\partial x}(x) = [0\ 0\ 0\ 1\ 1\ 1] \\ (ii)\ \ & \frac{\partial c_2}{\partial x}(x) = [0\ 0\ 0\ 1\ \ -1\ 1] \\ (iii)\ \ & \frac{\partial c_2}{\partial x}(x) = \left[0\ 0\ 0\ 1\ \ -\frac{\bar{q}_{y1}}{2\bar{q}_{y2}}\ \ \frac{\bar{q}_{y1}^2}{4\bar{q}_{y2}^2}\right] \end{aligned} \tag{7.33}$$

A design vector consisting of seven or eight design variables (five or six tension variables) can be solved the same way as with six design variables. There are still three possibilities for the value of $\bar{q}_{ymin}$; the leading edge, the trailing edge or in between. The difference for seven and eight design variables, is that there is now a possibility of being two or three

locations in $-1 <= x_{min} <= 1$ where a local minimum or maximum of $\bar{q}_y$ can occur. And so, just as with the six design variables, the local minima or maxima are found by solving for the value(s) of x where the derivative of $\bar{q}_y$ is zero. However, this requires solving a quadratic (seven design variables) or cubic (eight design variables) polynomial, and could result in complex roots.

$$\bar{q}_{ymin} = \bar{q}_y(x_{min}) \tag{7.34}$$

where x_{min} is the solution to

$$\frac{\partial}{\partial x}\bar{q}_y(x) = 0 \tag{7.35}$$

The roots, and therefore the gradients are quite long and not shown, but they can be calculated as described in Eqs. 7.34 and 7.35. The value of the constraint function for seven variables is determined by

$$\begin{aligned} c_2(x) &= \min\left(\bar{q}_y(x)\right) = \min\left[\bar{q}_y(-1)\ \bar{q}_y(1)\ \bar{q}_{ymin1}\ \bar{q}_{ymin2}\right] > 0 \text{ if } -1 <= x_{min} <= 1 \\ c_2(x) &= \min\left(\bar{q}_y(x)\right) = \min\left[\bar{q}_y(-1)\ \bar{q}_y(1)\right] > 0 \text{ if } -\infty < x_{min} < -1 \text{ or } 1 < x_{min} < \infty \end{aligned} \tag{7.36}$$

where $\bar{q}_{ymin1}$ and $\bar{q}_{ymin2}$ are solutions to Eq. 7.34 in the case for seven design variables. The value of the constraint function for seven variables is determined by

$$\begin{aligned} c_2(x) &= \min\left(\bar{q}_y(x)\right) = \min\left[\bar{q}_y(-1)\ \bar{q}_y(1)\ \bar{q}_{ymin1}\ \bar{q}_{ymin2}\ \bar{q}_{ymin3}\right] > 0 \text{ if } -1 <= x_{min} <= 1 \\ c_2(x) &= \min\left(\bar{q}_y(x)\right) = \min\left[\bar{q}_y(-1)\ \bar{q}_y(1)\right] > 0 \text{ if } -\infty < x_{min} < -1 \text{ or } 1 < x_{min} < \infty \end{aligned} \tag{7.37}$$

where $\bar{q}_{ymin1}$, $\bar{q}_{ymin2}$ and $\bar{q}_{ymin3}$ are solutions to Eq. 7.34 in the case for eight design variables.

There are four possibilities for the gradient in the case of seven design variables. The gradient would be (i) if $\bar{q}_{ymin} = \bar{q}_y(1)$ and the minimum or maximum of $\bar{q}_y(x)$ occurs in $-\infty < x_{min} < -1$ or $1 < x_{min} < \infty$. The gradient would be (ii) if $\bar{q}_{ymin} = \bar{q}_y(-1)$ and the minimum or maximum of $\bar{q}_y(x)$ occurs in $-\infty < x_{min} < -1$ or $1 < x_{min} < \infty$. The gradient would be (iii) if the minimum or maximum of $\bar{q}_y(x)$ occurs in $-1 <= x_{min} <= 1$ and the value of $\bar{q}_{ymin1}$ is smaller than $\bar{q}_y(1)$, $\bar{q}_y(-1)$ and $\bar{q}_{ymin2}$. The gradient would be (iv) if the minimum or maximum of $\bar{q}_y(x)$ occurs in $-1 <= x_{min} <= 1$ and the value of $\bar{q}_{ymin2}$ is smaller than $\bar{q}_y(1)$, $\bar{q}_y(-1)$ and $\bar{q}_{ymin1}$.

$$
\begin{aligned}
(i) \quad & \frac{\partial c_2}{\partial x}(x) = [0\ 0\ 0\ 1\ 1\ 1\ 1] \\
(ii) \quad & \frac{\partial c_2}{\partial x}(x) = [0\ 0\ 0\ 1\ -1\ 1\ -1] \\
(iii) \quad & \frac{\partial c_2}{\partial x}(x) = \left[0\ 0\ 0\ 1\ \frac{\partial q_{ymin1}}{\partial \bar{q}_{y1}}\ \frac{\partial q_{ymin1}}{\partial \bar{q}_{y2}}\ \frac{\partial q_{ymin1}}{\partial \bar{q}_{y3}}\right] \\
(iv) \quad & \frac{\partial c_2}{\partial x}(x) = \left[0\ 0\ 0\ 1\ \frac{\partial q_{ymin2}}{\partial \bar{q}_{y1}}\ \frac{\partial q_{ymin1}}{\partial \bar{q}_{y2}}\ \frac{\partial q_{ymin1}}{\partial \bar{q}_{y3}}\right]
\end{aligned}
\tag{7.38}
$$

There are five possibilities for the gradient in the case of eight design variables. The gradient would be (i) if $\bar{q}_{ymin} = \bar{q}_y(1)$ and the minimum or maximum of $\bar{q}_y(x)$ occurs in $-\infty < x_{min} < -1$ or $1 < x_{min} < \infty$. The gradient would be (ii) if $\bar{q}_{ymin} = \bar{q}_y(-1)$ and the minimum or maximum of $\bar{q}_y(x)$ occurs in $-\infty < x_{min} < -1$ or $1 < x_{min} < \infty$. The gradient would be (iii) if the minimum or maximum of $\bar{q}_y(x)$ occurs in $-1 <= x_{min} <= 1$ and the value of $\bar{q}_{ymin1}$ is smaller than $\bar{q}_y(1)$, $\bar{q}_y(-1)$, $\bar{q}_{ymin2}$ and $\bar{q}_{ymin3}$. The gradient would be (iv) if the minimum or maximum of $\bar{q}_y(x)$ occurs in $-1 <= x_{min} <= 1$ and the value of $\bar{q}_{ymin2}$ is smaller than $\bar{q}_y(1)$, $\bar{q}_y(-1)$, $\bar{q}_{ymin1}$ and $\bar{q}_{ymin3}$. The gradient would be (v) if the minimum or maximum of $\bar{q}_y(x)$ occurs in $-1 <= x_{min} <= 1$ and the value of $\bar{q}_{ymin3}$ is smaller than $\bar{q}_y(1)$, $\bar{q}_y(-1)$, $\bar{q}_{ymin1}$ and $\bar{q}_{ymin2}$.

$$
\begin{aligned}
(i)\quad & \frac{\partial c_2}{\partial x}(x) = [0\ 0\ 0\ 1\ 1\ 1\ 1\ 1] \\
(ii)\quad & \frac{\partial c_2}{\partial x}(x) = [0\ 0\ 0\ 1\ -1\ 1\ -1\ 1] \\
(iii)\quad & \frac{\partial c_2}{\partial x}(x) = \left[0\ 0\ 0\ 1\ \frac{\partial q_{ymin1}}{\partial \bar{q}_{y1}}\ \frac{\partial q_{ymin1}}{\partial \bar{q}_{y2}}\ \frac{\partial q_{ymin1}}{\partial \bar{q}_{y3}}\ \frac{\partial q_{ymin1}}{\partial \bar{q}_{y4}}\right] \\
(iv)\quad & \frac{\partial c_2}{\partial x}(x) = \left[0\ 0\ 0\ 1\ \frac{\partial q_{ymin2}}{\partial \bar{q}_{y1}}\ \frac{\partial q_{ymin2}}{\partial \bar{q}_{y2}}\ \frac{\partial q_{ymin2}}{\partial \bar{q}_{y3}}\ \frac{\partial q_{ymin2}}{\partial \bar{q}_{y4}}\right] \\
(v)\quad & \frac{\partial c_2}{\partial x}(x) = \left[0\ 0\ 0\ 1\ \frac{\partial q_{ymin3}}{\partial \bar{q}_{y1}}\ \frac{\partial q_{ymin3}}{\partial \bar{q}_{y2}}\ \frac{\partial q_{ymin3}}{\partial \bar{q}_{y3}}\ \frac{\partial q_{ymin3}}{\partial \bar{q}_{y4}}\right]
\end{aligned}
\tag{7.39}
$$

7.3.2 Sensitivity of Divergence Constraint with Respect to the Design Variables

Constraining the tension to be greater than zero is not sufficient enough to ensure that aeroelastic divergence will not occur. A constraint needs to be placed on the aeroelastic stiffness such that it is always positive definite. The aeroelastic stiffness can be expressed in terms of an alternate nondimensionalized variable, $\tilde{q}$

$$
\Big[K(q)\Big] - \frac{1}{\sigma k^2}\Big[P_D\Big] \tag{7.40}
$$

where $\tilde{q}$ is

$$
\tilde{q} = \bar{q}\sigma k^2 \tag{7.41}
$$

The aeroelastic stiffness is now

$$
\Big(\Big[K(\tilde{q})\Big] - \Big[P_D\Big]\Big)\Big|_{k=0} \tag{7.42}
$$

A three degree of freedom system will have three divergent modes. However, only the mode which diverges at lowest velocity or highest stiffness is critical. The stiffness at which the smallest eigenvalue of the aeroelastic stiffness matrix becomes negative is the stiffness where divergence will occur. The divergence constraint is

$$c_3(x) = \min\left(\mathrm{Re}\left(\lambda_{K_{aero}}\right)\right) > 0 \tag{7.43}$$

where $\lambda_{K_{aero}}$ are the eigenvalues of the aeroelastic stiffness. The sensitivity of eigenvalues with respect to the design variables is given in Haftka and Gürdal[57].

$$\frac{\partial \lambda_{K_{aero}}}{\partial x} = \frac{u^T \frac{\partial K}{\partial x} v}{u^T v} \tag{7.44}$$

where u and v are the left and right eigenvectors respectively. Thus, the sensitivity of the real part of the minimum eigenvalue is

$$\frac{\partial c_3}{\partial x}(x) = \mathrm{Re}\left(\frac{u_{min}^T \frac{\partial K}{\partial x} v_{min}}{u_{min}^T v_{min}}\right) \tag{7.45}$$

7.3.3 Sensitivity of the Efficiency Constraint with Respect to the Design Variables

The multi-objective optimization requires the propulsive efficiency be constrained to generate the Pareto front. The efficiency constraint expressed in the complex form of the airfoil motion is

$$c_4(x) = T_{avg} - \eta_{ref} W_{avg} = \frac{1}{2}\mathrm{Re}\left(\{h\}\,[T_M]\,\{h\}^T\right) - \eta_{ref}\frac{1}{2}\mathrm{Re}\left(\{h\}\,[W_M]\,\{h\}^T\right) = 0 \tag{7.46}$$

where $()^T$ is the conjugate transpose. Therefore, the gradient of this constraint is

$$\frac{\partial c_4}{\partial x}(x) = \frac{\partial T_{avg}}{\partial x} - \eta_{ref}\frac{\partial W_{avg}}{\partial x} \tag{7.47}$$

where the sensitivity of stroke-averaged thrust is derived in Section 7.1 and detailed in Eqs. 7.3 through 7.13. The complex form of the work done by the structure is the exact same form as the stroke-averaged thrust and is computed the same way using the matrix W_M rather than T_M.

These sensitives utilized in gradient based optimization will ensure convergence to a solution, but not necessarily the global optimum. Furthermore, the speed of convergence will be improved.

Chapter 8

Aeroelastic Tailoring Results

This chapter presents optimization results of the aeroelastic system for maximum thrust, maximum normalized thrust and thrust efficiency. The optimization is constrained such that the spanwise and chordwise tension are everywhere positive and aeroelastic divergence does not occur. Optimization for maximum thrust is performed on a one degree of freedom system, for purposes of showing the physics of the system; and a three degree of freedom system. The normalized stroke-averaged thrust optimization was performed for a three degree of freedom system.

All results shown in this chapter were generated in MATLAB using the gradient based optimization function *fmincon* while using the analytic sensitivities presented in Chapter 7. Some results were generated using the genetic algorithm *ga* to obtain points which gradient based optimization was unable to find. The multi-objective optimization was done via the ϵ-constraint method.

8.1 Aeroelastic Tailoring for Maximum Thrust of a Plunging Membrane Wing

8.1.1 Analysis and Optimization of a One Degree of Freedom Membrane Wing

The system of equations in Eq. 6.18 provides the basis for optimization of the aeroelastic system for any number of assumed mode shapes and any functional form of the spanwise tension. However, much can be learned from a simpler 1 degree of freedom model. Assuming a rigid body motion consisting of only plunge and the membrane vibrating in the first assumed mode, a_2, the aeroelastic system reduces to a single equation for the complex magnitude of the deformation.

$$\bar{a}_2 = -\frac{4}{\pi}\frac{\frac{1}{\sigma k^2}P_R + F_I}{M - K + \frac{1}{\sigma k^2}P_D}\bar{a}_0 \tag{8.1}$$

where the stiffness, K, contains tension terms, q_x and $q_y(x)$, M is the normalized mass term and F_I is the inertial force term. The aerodynamic term, P_D is the nodal force due to $\bar{a}_2$ in the $\bar{a}_2$ direction and P_R is the nodal force due to $\bar{a}_0$ in the $\bar{a}_2$ direction.

Eq. 8.1 gives the complex magnitude of the deformation for a prescribed plunging motion at a specific reduced frequency and mass ratio. Using the plunge and deformation information with Eq. 6.25 will give the complex magnitude of the motion in terms of the aerodynamic deformation shapes. This information can be used in Eq. 3.52 to obtain the average thrust for the aeroelastic system. Therefore specifying a rigid body motion, reduced frequency and mass ratio will pose the optimization problem where stiffness is the design variable.

Consider a case where the spanwise tension in the membrane is also constant, $S_y(X) = S_{y_0}$ or $q_y(x) = q_{y_0}$. The parameters for this system are found in Eq. 6.19 and Eq. 6.29.

$$
\begin{aligned}
K &= \frac{8}{3}q_x + \frac{16}{15}q_{y_0} \\
M &= \frac{16}{15} \\
F_I &= \frac{4}{3} \\
P_D &= \frac{\pi}{6}\left(6 + 6C(k)(2 - ik) + 7k^2\right) \\
P_R &= \frac{\pi}{2}k\left(4iC(k) - 3k\right)
\end{aligned}
\tag{8.2}
$$

The problem is constrained such that spanwise, Eq. 7.25 and chordwise, Eq. 7.23 tension are everywhere positive and the stiffness is large enough such that aeroelastic divergence will not occur, Eq. 7.43. We can rewrite the nondimensional stiffness in terms of the alternate nondimensional variables, $\tilde{q}$ shown in Eq. 7.41.

$$
K = \frac{1}{\sigma k^2}\left(\frac{8}{3}\tilde{q}_x + \frac{16}{15}\tilde{q}_{y0}\right) \tag{8.3}
$$

where

$$
\begin{aligned}
\tilde{q}_x &= \frac{S_x}{\frac{1}{2}\rho_a u^2 b} \\
\tilde{q}_{y0} &= \frac{S_{y_0} b}{\frac{1}{2}\rho_a u^2 s^2}
\end{aligned}
\tag{8.4}
$$

Figures 8.1 and 8.2 show the effect of stiffness on the stroke-averaged thrust for a deformable wing in unit harmonic plunging. The added grid line above zero in Figure 8.1 represents 1. As expected, the stiffness has a significant influence on the thrust generated by the membrane wing. Typically the thrust generated by the flexible membrane wing has large changes below the divergence stiffness. Above the divergence stiffness, though, the thrust typically increases starting from negative values to peak at values in excess of the rigid

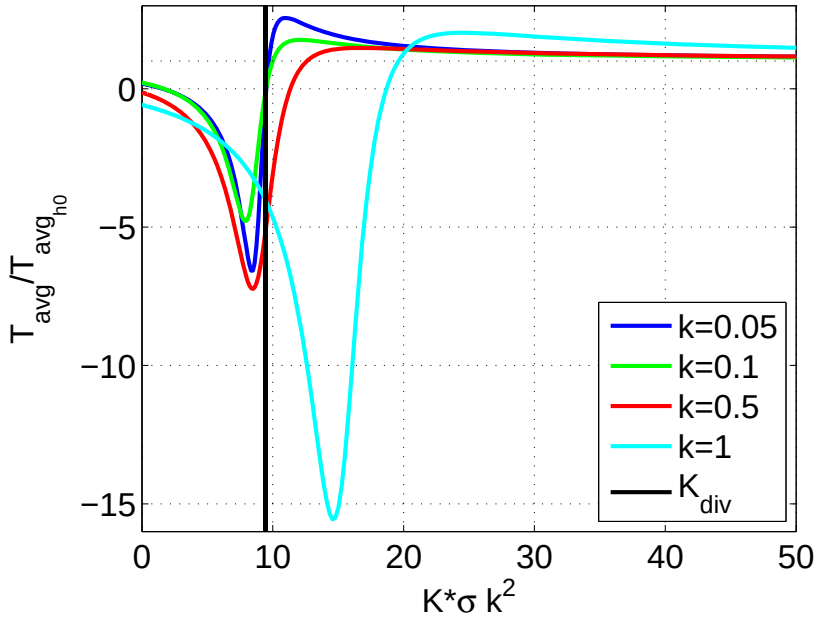

Figure 8.1: Effect of stiffness on average thrust for $k = 0.25$ (1 degree of freedom)

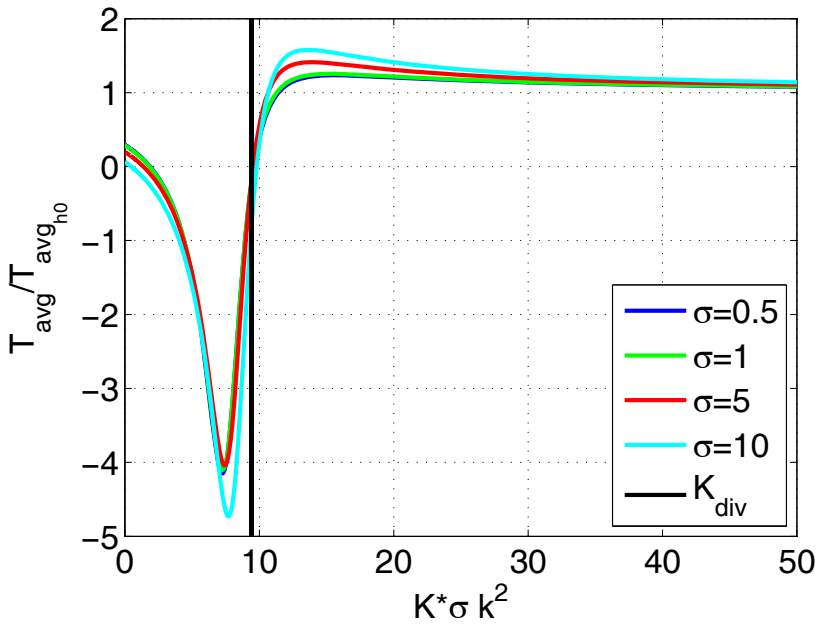

Figure 8.2: Effect of stiffness on average thrust for $\sigma = 5$ (1 degree of freedom)

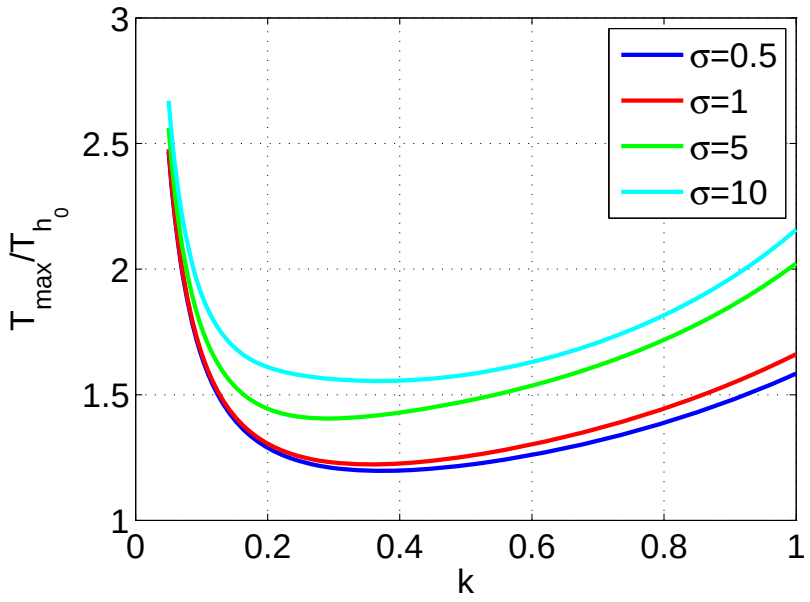

Figure 8.3: Maximum thrust as a function of reduced frequency (1 degree of freedom)

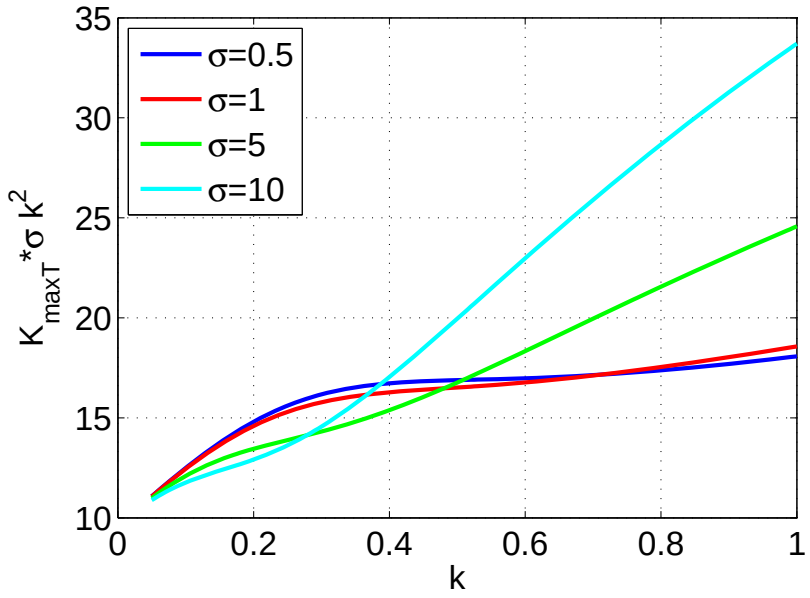

Figure 8.4: Stiffness for maximum thrust (1 degree of freedom)

wing thrust. Then as the stiffness further increases, the thrust generated asymptotically approaches the rigid wing results. For all cases, one can choose a range of stiffness for which the flexible wing outperforms the rigid wing. Figure 8.1 shows that for a given mass ratio the results change significantly with reduced frequencies. Figure 8.2 shows that for a given reduced frequency, the results do not change as much with mass ratio. The stiffness is comprised of parts due to the chordwise tension and spanwise tension as shown in Eq. 8.2. Stiffness is a scalar for the 1 degree of freedom system, and so performing a multivariable optimization is redundant. However, this does show that any combination of spanwise and chordwise tensions in the form of Eq. 8.2 that produce the stiffness equal to the value required for maximum thrust is a viable design solution.

The maximum thrust as a function of reduced frequency for various values of mass ratios is given in Figure 8.3. The corresponding stiffnesses are plotted in Figure 8.4. The optimization routine, *fmincon* in MATLAB was used to generate the results. It can be seen that a flexible wing can always be designed to yield a larger thrust as compared to a rigid wing in a unit harmonic plunging motion. For a given mass ratio, there is a specific reduced frequency at which the increase in thrust is a minimum with the increase being high for both low and high reduced frequencies. Increasing frequency for a specific mass will make the added mass component of the aerodynamics larger, which leads to a larger deformation and therefore a larger thrust. However, decreasing the frequency leads to the maximum thrust occurring at a lower stiffness because the wing is more compliant. As reduced frequency approaches zero, the stiffness for maximum thrust approaches the stiffness, which will lead to divergence, which leads to the larger increase of thrust over the rigid body case.

Increasing the mass ratio also changes the maximum average thrust. A heavier wing will lead to more thrust than a lighter one when a unit plunge is prescribed, which was also shown by Pederzani and Haj-Hariri[45] for a viscous flow. This is due to the inertial effects of the wing itself. A heavier wing will deform more, increasing the magnitude of deformation, which will then increase the maximum thrust.

The one degree of freedom case described above provides a very useful approximation

for tensions required in a membrane wing such that maximum thrust can be generated when flapping. However, the actual wing will deform in higher modes as well and the thrust can be accurately captured only if more degrees of freedom are considered. Furthermore, more degrees of freedom leads to a stiffness matrix with multiple stiffness numbers which can be tailored. This is achieved by having a nonuniform spanwise tension.

8.1.2 Analysis and Optimization of a Three Degree of Freedom Membrane Wing

The one degree of freedom results show much insight into the physics of the aeroelastic system. However, realistic systems will vibrate in more than one degree of freedom. Consider a three degree of freedom system. The mass, stiffness and forcing matrices are determined from Eq. 6.19. The deformations are

$$\begin{Bmatrix} \bar{a}_2 \\ \bar{a}_3 \\ \bar{a}_4 \end{Bmatrix} = -\frac{4}{\pi}\left(\left[M\right] - \left[K\right] + \frac{1}{\sigma k^2}\left[P_D\right]\right)^{-1}\left(\frac{1}{\sigma k^2}\left[P_R\right] + \left[F_I\right]\right)\begin{Bmatrix} \bar{a}_0 \\ \bar{a}_1 \end{Bmatrix} \tag{8.5}$$

The stiffness matrix is a function of both the chordwise tension, q_x, and the spanwise tension, $q_y(x)$.

Three Degree of Freedom System with One Design Variable

Consider a case where the spanwise tension is a constant and is equal to the chordwise tension. The resulting optimization problem will be a three degree of freedom system with a one variable design space. As with the one degree of freedom system, constraints are placed on the spanwise tension, chordwise tension and aeroelastic stiffness.

Figures 8.5 and 8.6 show the stroke-averaged thrust of the three degree of freedom case as a function of the tension variable $q_x = q_{y_0}$ for two sets of parameters. The results

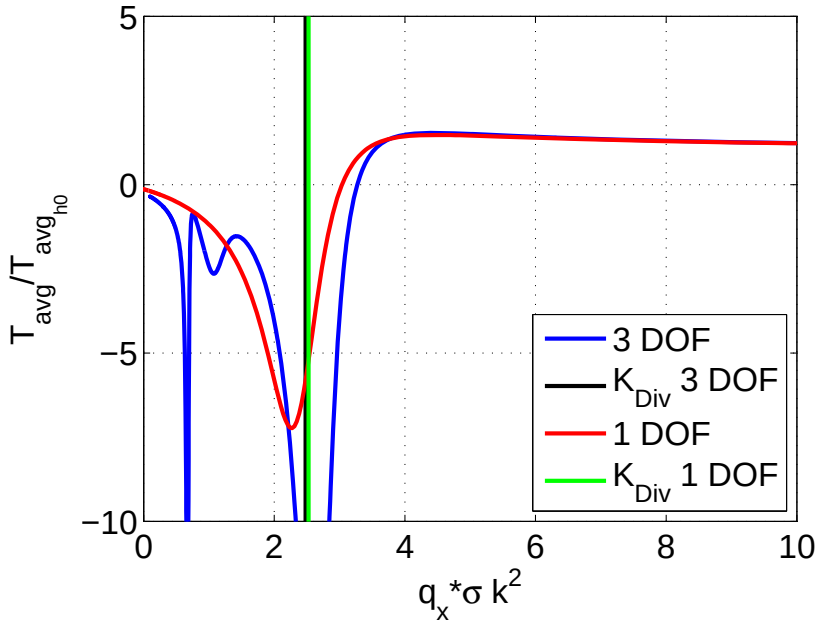

Figure 8.5: Effect of stiffness on average thrust for $k = 0.5$ and $\sigma = 5$ (3 degrees of freedom)

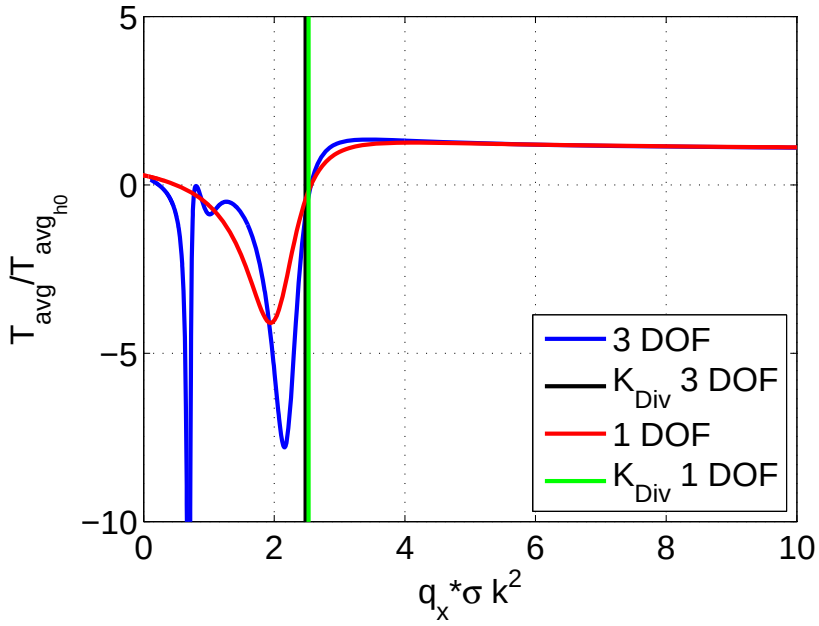

Figure 8.6: Effect of stiffness on average thrust for $k = 0.25$ and $\sigma = 1$ (3 degrees of freedom)

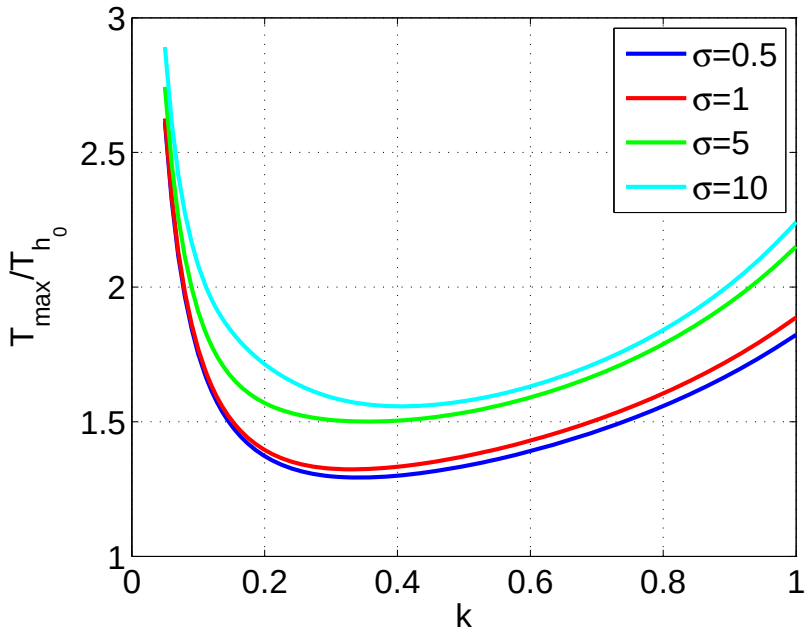

Figure 8.7: Maximum thrust for a 3 degree of freedom system using a single design variable

are compared to the one degree of freedom case. It can be seen that a more accurate model including more than one degree of freedom results in different thrust values. The divergence stiffness for the two models are close. The results for the thrust are close for stiffness much above the divergence stiffness but the results below divergence stiffness are very different. This is expected as a 3 degree of freedom system is likely to have 2 more lower divergence stiffnesses and associated dynamics.

Figure 8.7 shows the maximum stroke-averaged thrust as a function of reduced frequency. As with the one degree of freedom system, the maximum thrust increases with an increase and a decrease in reduced frequency from a minimum value. Also higher mass ratios lead to higher improvement in performance of the optimized flexible wing. Figure 8.8 shows a comparison of the one degree of freedom and three degree of freedom systems at a low and high value of mass ratio. Again we see that the one degree of freedom system captures the trend accurately but is different than the three degree of freedom model sometimes by up to 15%. The optimal three degree of freedom flexible wing seems to generate more than or close to the same thrust as an optimal one degree of freedom flexible wing.

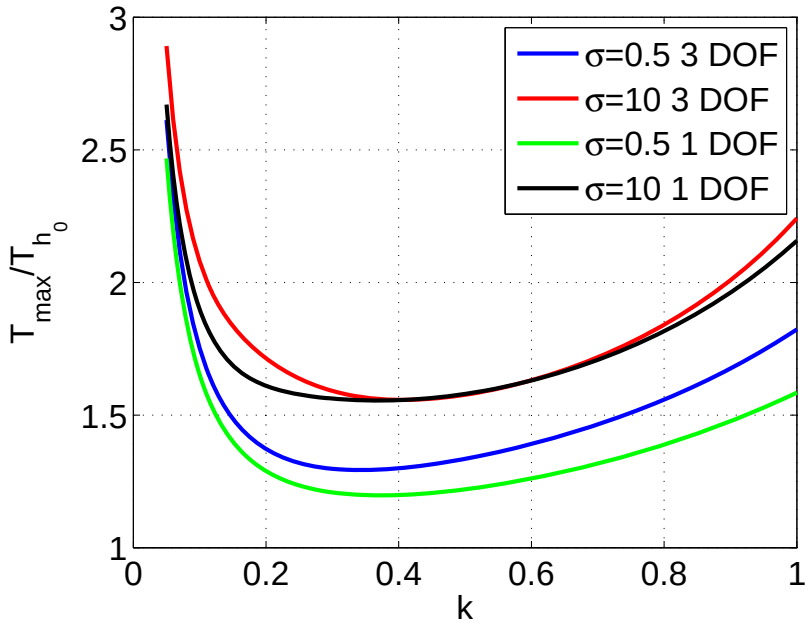

Figure 8.8: Difference in results between the 3 degree of freedom system and 1 degree of freedom system

Increasing the number of degrees of freedom of the system does not change the system such that it can be tailored for more thrust. It simply models the physics of the system more accurately. The only way to achieve larger thrust is by expanding the design space by having the spanwise tension take a more general form.

Three Degree of Freedom System with Multiple Design Variables

Let us represent the nondimensional tension, $q_y(x)$, is terms of a polynomial expansion with

$$q_y(x) = \sum_{i=0}^{M} q_{y_i} x^i = q_{y_0} + q_{y_1} x + q_{y2} x + \cdots + q_{y_N} x^M \tag{8.6}$$

The optimization problem now has $N + 2$ design variables. The stiffness matrix is a function of these design variables. However, for the three degree of freedom system the stiffness matrix can only have six independent terms due to symmetry. Therefore having

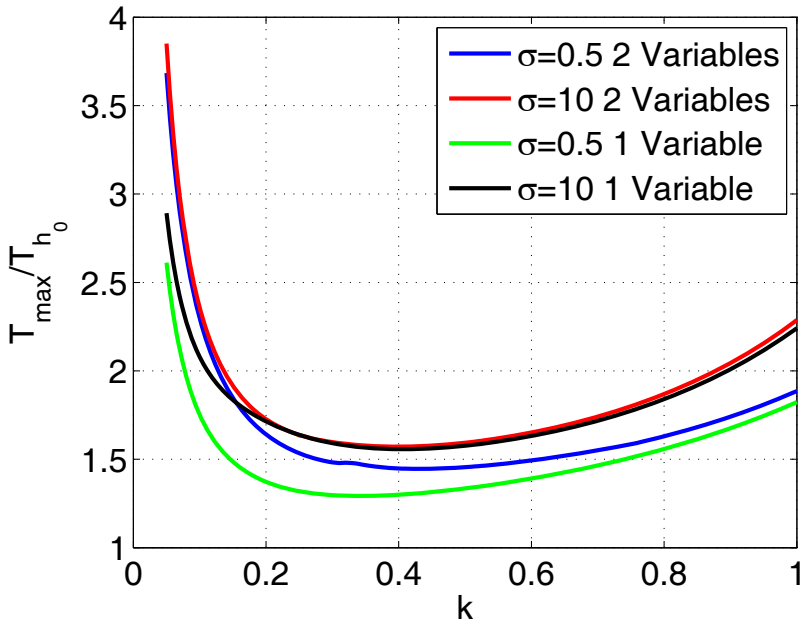

Figure 8.9: Improvement of maximum thrust with 2 design variables for a 3 DOF system

more than six design variables is redundant. The largest feasible design space for the three degree of freedom system is q_x, q_{y_0}, q_{y_1}, q_{y_2}, q_{y_3} and q_{y_4}.

Consider the two design variable case where the spanwise and chordwise tensions are constant, but are not required to be equal to each other. During studies of the two variable problem it was found that multiple maxima existed and the optima calculated was dependent on the initial guess provided. Figure 8.9 shows the improvement in optimal thrust by expanding the design space from one to two variables. The results presented use the optimal but equal tensions from the one design variable case as the starting point for the optimization. This always leads to improvement in thrust performance. However, there is no guarantee that the solution is the global maximum. The two design variable system shows improvement over the one design variable system for both a small and large mass ratios over a range of reduced frequency. Therefore allowing the membrane wing to have different tensions in the spanwise and chordwise directions allows for the structure to be tailored so that more thrust can be produced during pure plunging.

Finally, consider a third case with three design variables, q_x, q_{y_0} and q_{y_1}. The de-

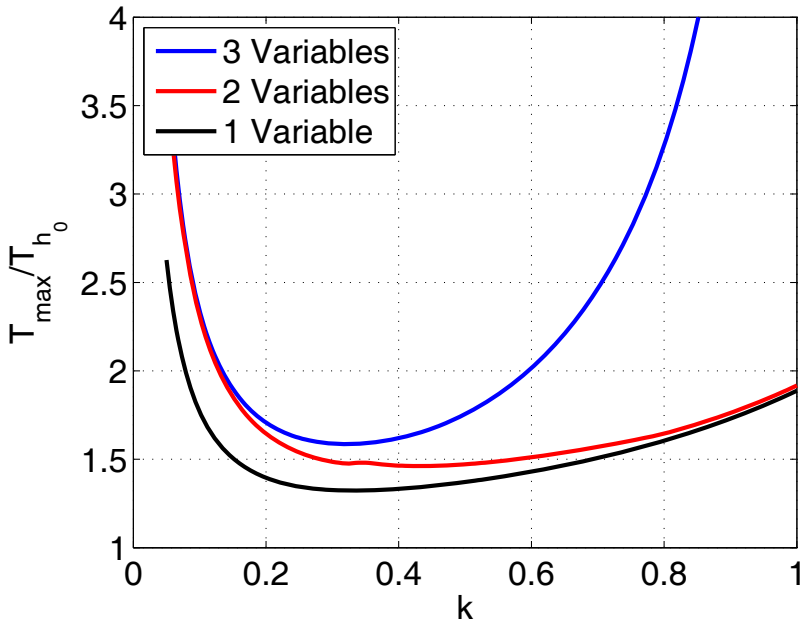

Figure 8.10: Improvement of maximum thrust with 3 design variables for a 3 degree of freedom system for $\sigma = 1$

sign space for the three variable system allows for a linear variation in the spanwise tension. Figures 8.10 and 8.11 show the optimized stroke-averaged thrust and corresponding nondimensional spanwise tension at various reduced frequencies. Expanding the design space to have linear spanwise tension variation along the chord significantly increases the amount of thrust possible for an airfoil undergoing unit plunge. This improvement is very large at higher reduced frequencies. The majority of the thrust is coming from near the leading edge of the airfoil. The optimum tension is a linear function with the tension equal to zero at the leading edge which allows the deflection to be larger there. The large deflection rotates the pressure difference normal at the surface toward the free stream direction. This provides a large contribution to thrust from the pressure difference across the airfoil which is added to the leading edge suction thrust from the plunging.

At low reduced frequencies the optimal spanwise tension function for maximum thrust is not zero at the leading edge. Further investigation using different initial guesses resulted in convergence to multiple maxima. Therefore, there is the possibility that the solution at

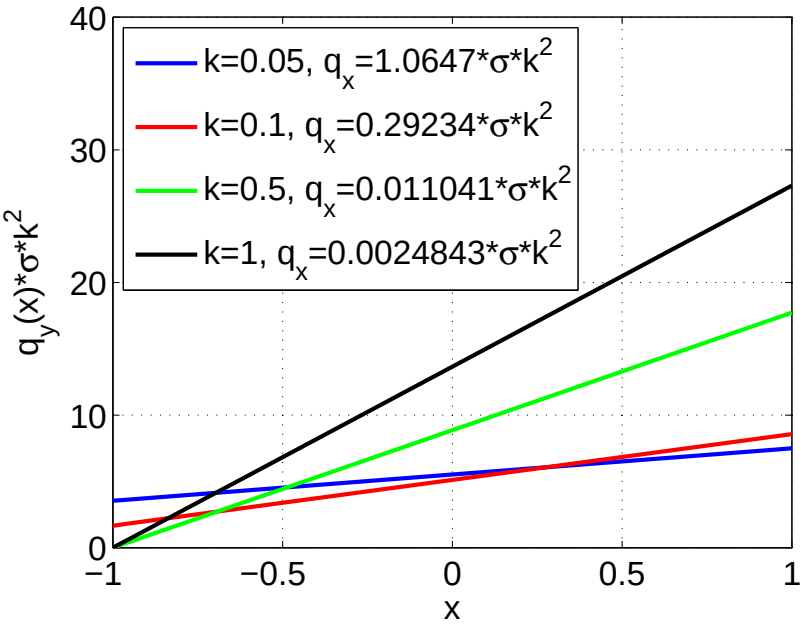

Figure 8.11: Spanwise tension for maximum thrust of a 3 design variable, 3 degree of freedom system for $\sigma = 1$

low reduced frequencies is not a maximum in the region of the solution at higher frequencies.

Figure 8.10 shows a very large increase in maximum thrust as a function of reduced frequency. Continuing to optimize for high values of reduced frequency results in an exponential increase in maximum thrust, which violates the assumption of small deformations used in the derivation of the thin airfoil theory. Thus, an explanation of this increase in thrust is required, as well as the addition of a motion constraint or modification of the objective function is required in order to generate meaningful results within the bounds of the aerodynamic model.

8.1.3 Investigation of Exponential Increase in Thrust

One possible reason for an exponential harmonic deformation is that the system is becoming dynamically unstable. Therefore the possibility of flutter must be investigated. Flutter has been ignored as a problem thus far because Patil was able to show that conservation of energy dictates energy must be taken from the wake and the structure and contribute to thrust in a

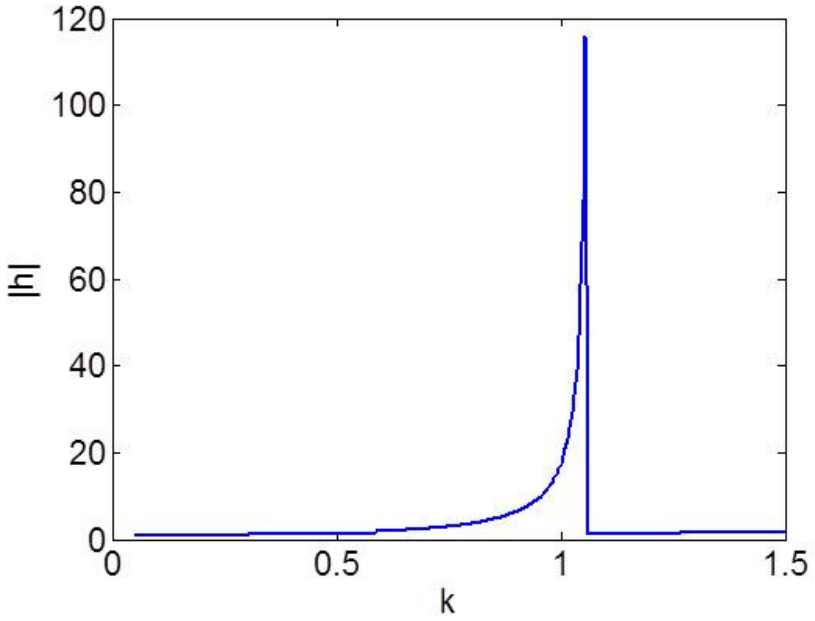

Figure 8.12: Magnitude of deformation required for maximum thrust with 3 design variables for $\sigma = 1$

system that is producing thrust[18]. Therefore, the maximum thrust, if positive, would not correspond to a system which is fluttering. Figure 8.12 shows the norm of the deformation vector as a function of reduced frequency for a unit mass ratio for the three tension variable case shown in Figure 8.10.

It can be seen that the norm of the magnitude of deformation is increasing at the same rate as the stroke-averaged thrust and appears to have a maximum around a reduced frequency of $k \approx 1.05$. The stroke-averaged thrust per unit deformation, shown in Figure 8.13 is a better method of observing the behavior of the system at this point. The thrust per unit deformation is approaching zero at $k \approx 1.05$. It is also seen that the solution jumps from one maximum to another, which was deemed possible when optimizing with one design variable. This confirms the existence of multiple maxima. Nonetheless, it can be deduced that at the specific combination of reduced frequency and mass ratio, the system is approaching the flutter instability.

A dynamic system that is fluttering will have a zero real part of the determinate[54].

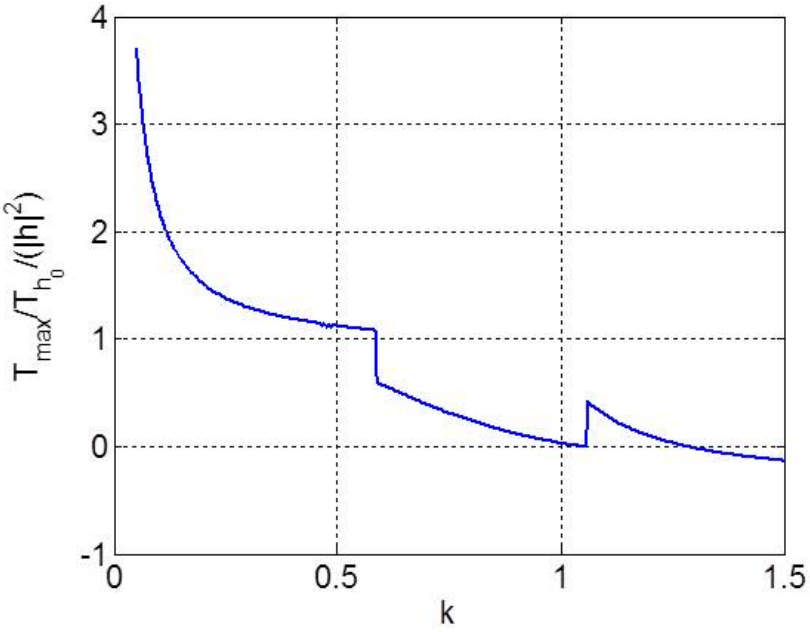

Figure 8.13: Maximum thrust normalized by the deformation with 3 design variables for $\sigma = 1$

Figure 8.14 shows the real and imaginary components the determinate of the system as a function of reduced frequency, and it can be seen that it approaches zero as reduced frequency approaches $k \approx 1.05$. Therefore, it can be deduced that the reason for the exponential increase in maximum thrust for a unit mass ratio is a result of the aeroelastic system becoming dynamically unstable due to flutter.

It has been shown that unlike the aerodynamic system, the aeroelastic system is naturally bounded and has an optimum that is not infinity. However, the maximum stroke-averaged thrust results in a design which has very large deformations at certain values of reduced frequency due to approaching the flutter instability. These results also violate the assumption of small deformations, which is the reason for the magnitude constraint in the aerodynamic optimization. Thus, the deformation should be constrained to a specific value, as with the aerodynamic optimization or one could just refine the objective function to normalized stroke-averaged thrust (thrust per unit deformation), which essentially creates a unit deformation constraint.

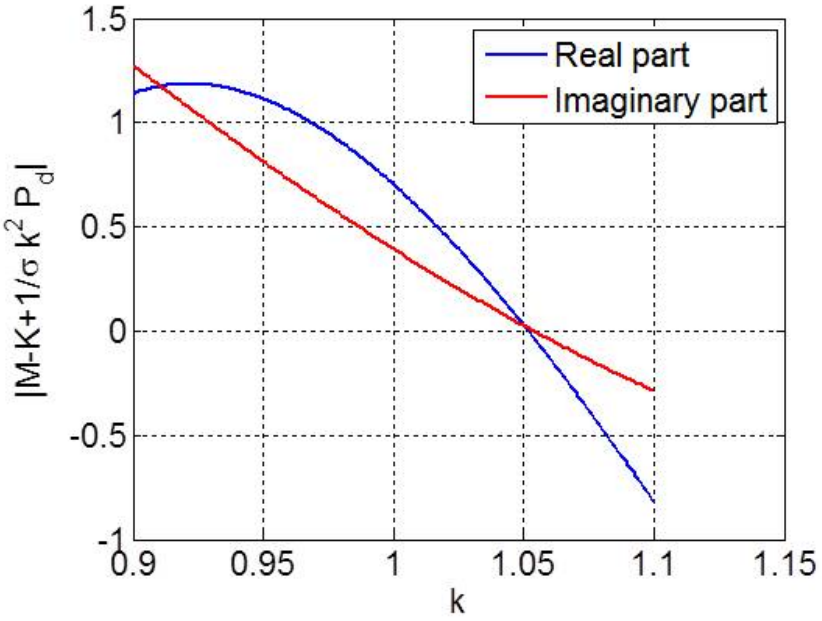

Figure 8.14: Determinate of the aeroelastic system with 3 design variables for $\sigma = 1$

8.2 Aeroelastic Tailoring for Maximum Normalized Thrust of a Pitching and Plunging Membrane Wing

Thrust optimization where the motion was unrestricted resulted in the optimization tending toward flutter. Therefore the normalized thrust was optimized. The optimization was subject to the constraints that the chordwise tension distribution was greater than zero, the spanwise tension distribution was everywhere greater than zero and the aeroelastic stiffness was greater than zero. Optimization was performed for three to eight design variables given a unit plunge motion. Table 8.1 shows the design vector for a given number of design variables. The three design variable optimization consists of one tension variable, meaning the tension is the same spanwise and chordwise, and two variables for the magnitude and phase of pitch relative to plunge. Increasing the design space to eight variables allows the tension to take a more general form.

Figure 8.15 shows the improvement of maximum thrust over unit plunging as a function of reduced frequency for a unit mass ratio as the design space increases. The aerodynamic

Number of variables	Design vector
3 Design variables	$\{a_{1Re}\ a_{1Im}\ q_x\}$
4 Design variables	$\{a_{1Re}\ a_{1Im}\ q_x\ q_{y0}\}$
5 Design variables	$\{a_{1Re}\ a_{1Im}\ q_x\ q_{y0}\ q_{y1}\}$
6 Design variables	$\{a_{1Re}\ a_{1Im}\ q_x\ q_{y0}\ q_{y1}\ q_{y2}\}$
7 Design variables	$\{a_{1Re}\ a_{1Im}\ q_x\ q_{y0}\ q_{y1}\ q_{y2}\ q_{y3}\}$
8 Design variables	$\{a_{1Re}\ a_{1Im}\ q_x\ q_{y0}\ q_{y1}\ q_{y2}\ q_{y3}\ q_{y4}\}$

Table 8.1: Design vector for different numbers of design variables

optimization lines for the rigid body motion case and five (two rigid body shapes and three deformations) calculated in Chapter 4 are shown as well.

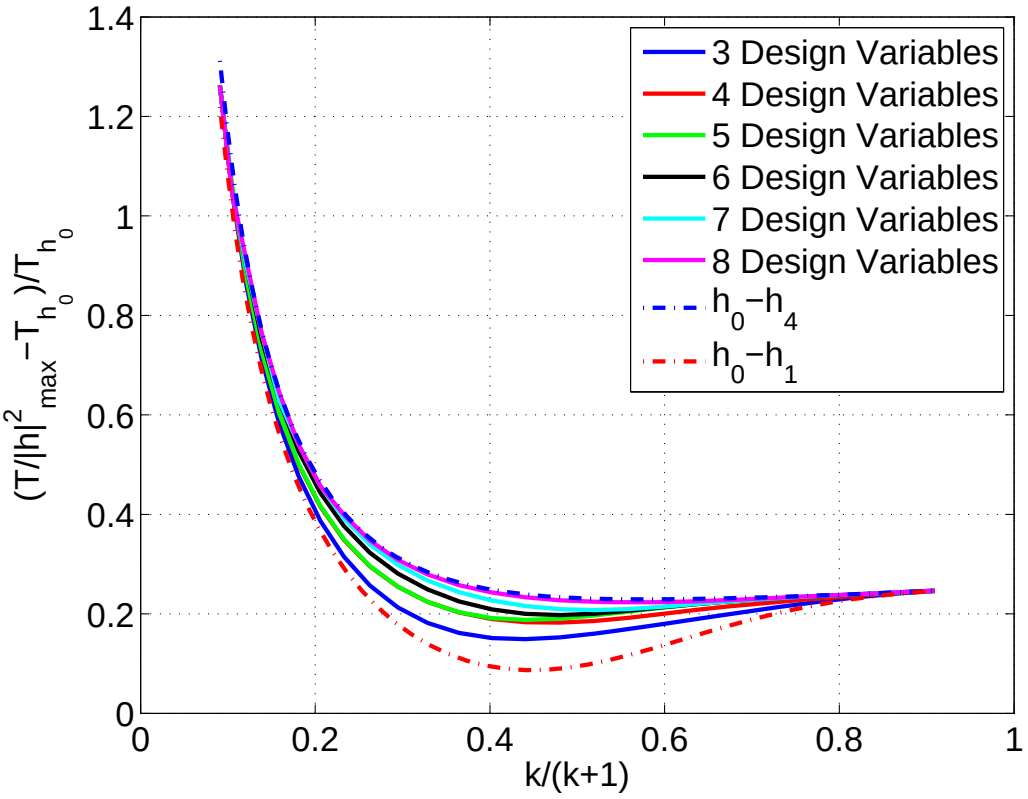

Figure 8.15: Maximum Thrust ($\sigma = 1$)

As expected, designing a flexible membrane wing results in more thrust as compared to rigid body motion. This is a very useful result because realistic wings will deform naturally as a result of aerodynamic and inertial forces; and so designing the wing to take advantage

of the deformation is essential. Continuing to allow the tension to take a more general form results in an increase in maximum thrust, as expected. The aerodynamic optimization for five shapes (three degrees of freedom in deformation) is the absolute best possible result that the aeroelastic optimization can generate with the three degrees of freedom. This is because the aerodynamic optimization assumes the shapes can be prescribed, when they are not. Designing the wing to deform in the mode that produces the shape for maximum thrust found in the aerodynamic optimization is the best solution possible. It can be seen that optimizing with only six tension variables can reach thrust very close to that obtained by the aerodynamic optimization with prescribed deformation.

Realistic MAVs will likely not have a unit mass ratio. Thus, results are presented for mass ratios that represent typical bird wings. Experimental work by Van Den Berg[58] on various bird and bat wings shows mass ratios range from $\sigma = 15$ to nearly $\sigma = 150$ with an average of around $\sigma = 40$. The percent increase in maximum thrust over plunge for mass ratios of 15, 40 and 150 are shown below in Figures 8.16 through 8.18.

The larger mass ratio corresponds to a wing that is significantly heavier than the surrounding air. Thus, the inertia of the wing will lead to larger deformation in a membrane undergoing unit plunging. This is reflected in the results. Allowing the rigid wing to deform with only 1 tension variable yields a significant increase in maximum thrust. Allowing the tension to be different in the spanwise and chordwise directions results in an increase in maximum thrust that is nearly as good as the aerodynamic optimum. Further increases in thrust are achievable by adding more tension terms, however the increase is very small.

Another interesting result is that the effect of mass ratio appears to be quite insignificant at values where the wing is far heavier than the air. It can be seen that Figures 8.16 through 8.18 appear very similar. As mass ratio increases the maximum thrust increases as well, but by a very small amount. Therefore heavier wings are capable of producing values of thrust closer to the aerodynamic optimum than lighter ones. An alternate way of looking at this is that a smaller design space (or less complex structure) is required for a heavy wing to achieve the aerodynamic optimum.

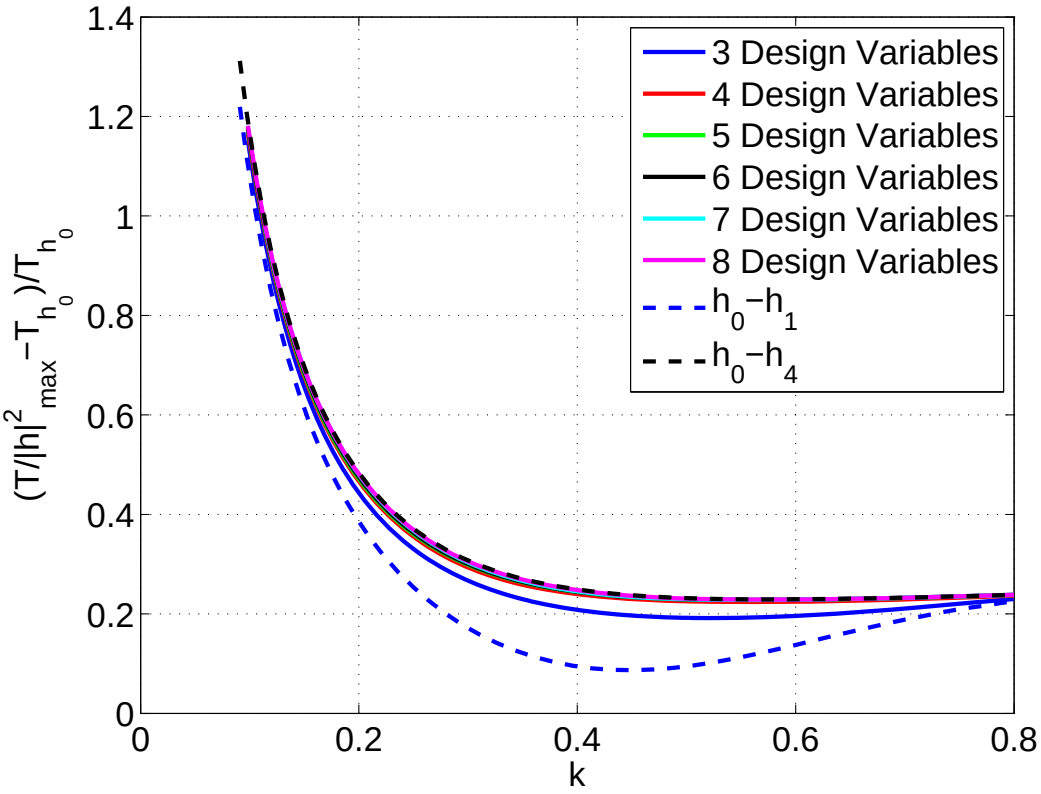

Figure 8.16: Maximum Thrust ($\sigma = 15$)

A very large range of reduced frequencies has been shown, however flapping wing MAV's will not fly over the entire range of frequency shown, but in the regime of bird flight. Observation of bird flight has shown the typical regime of reduced frequency to be $k = 0.2$ through $k = 0.4$. Thus, the percent increase in maximum thrust over plunge for a deformable membrane wing undergoing unit plunging for the bird flight regime at the average mass ratio of $\sigma = 40$ is shown in Figure 8.19.

These results are quite useful because they show that if a wing that generates the maximum thrust possible is desired, a complex design is not needed. Most of the thrust can be generated by choosing the correct value of spanwise and chordwise tension. However, the maximum thrust is not always the desired result. Flapping wing MAVs are very small and must carry the energy required for flight on board, most likely in a battery. Propulsive

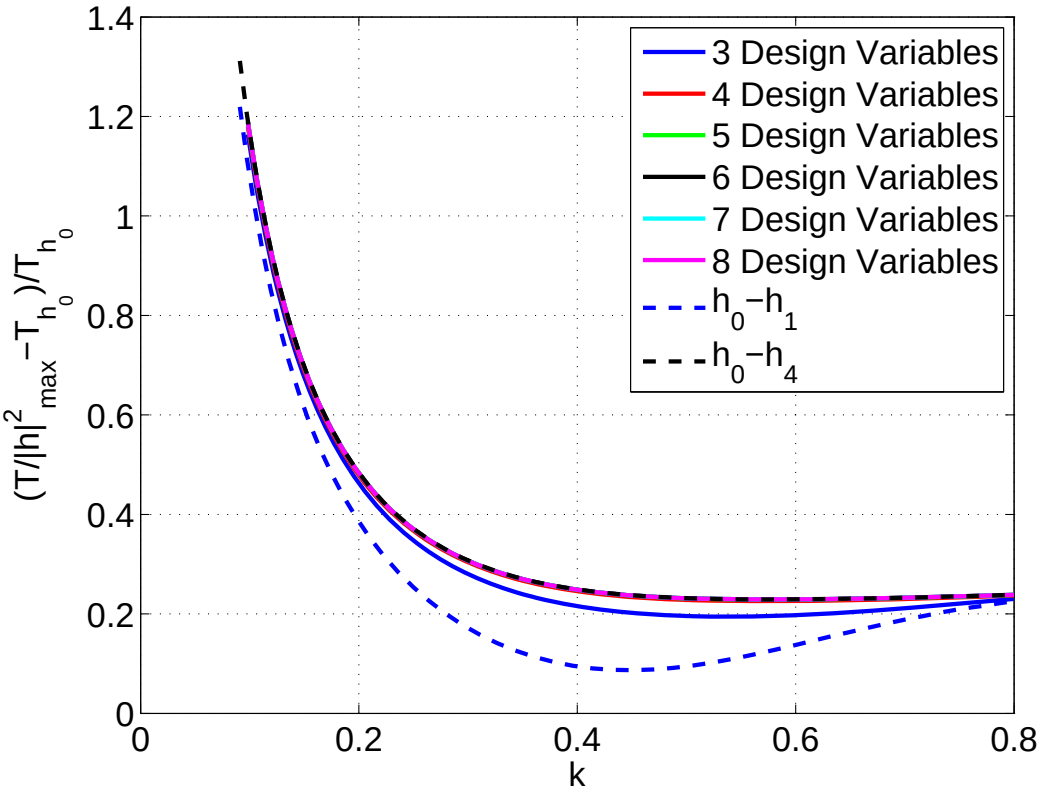

Figure 8.17: Maximum Thrust ($\sigma = 40$)

efficiency of the wing is just as important to MAV flight as the thrust producing capability. The following section investigates the multi-objective optimization for stroke-averaged thrust and propulsive efficiency.

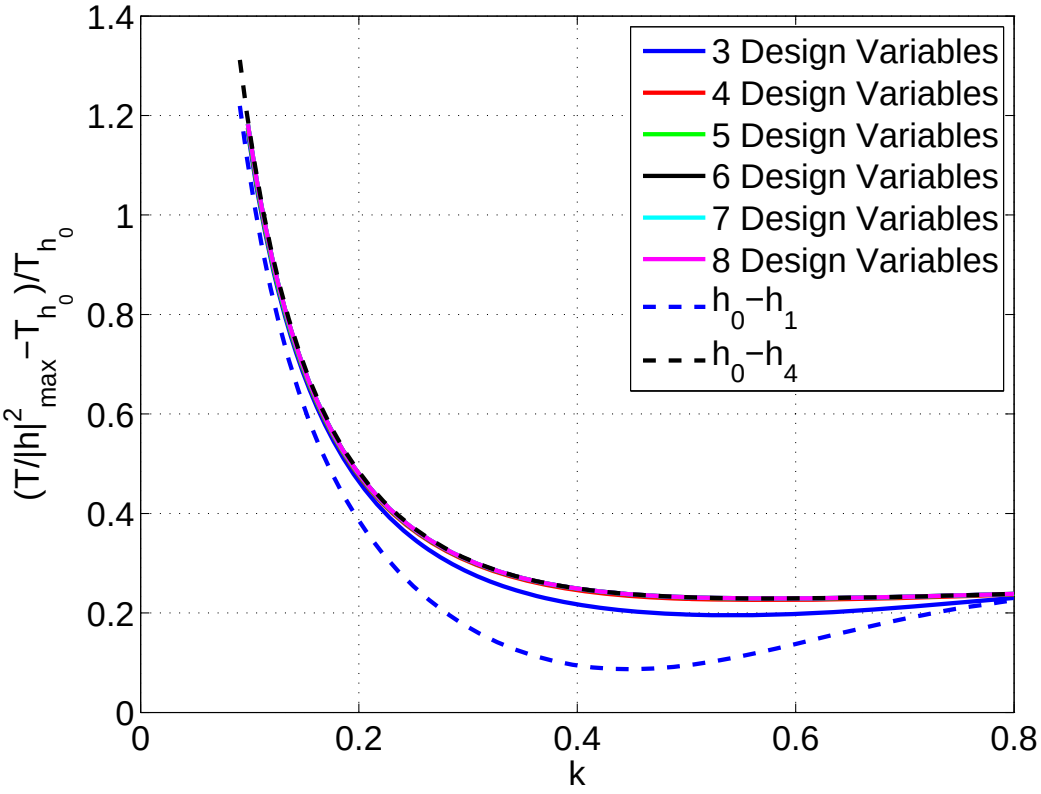

Figure 8.18: Maximum Thrust ($\sigma = 150$)

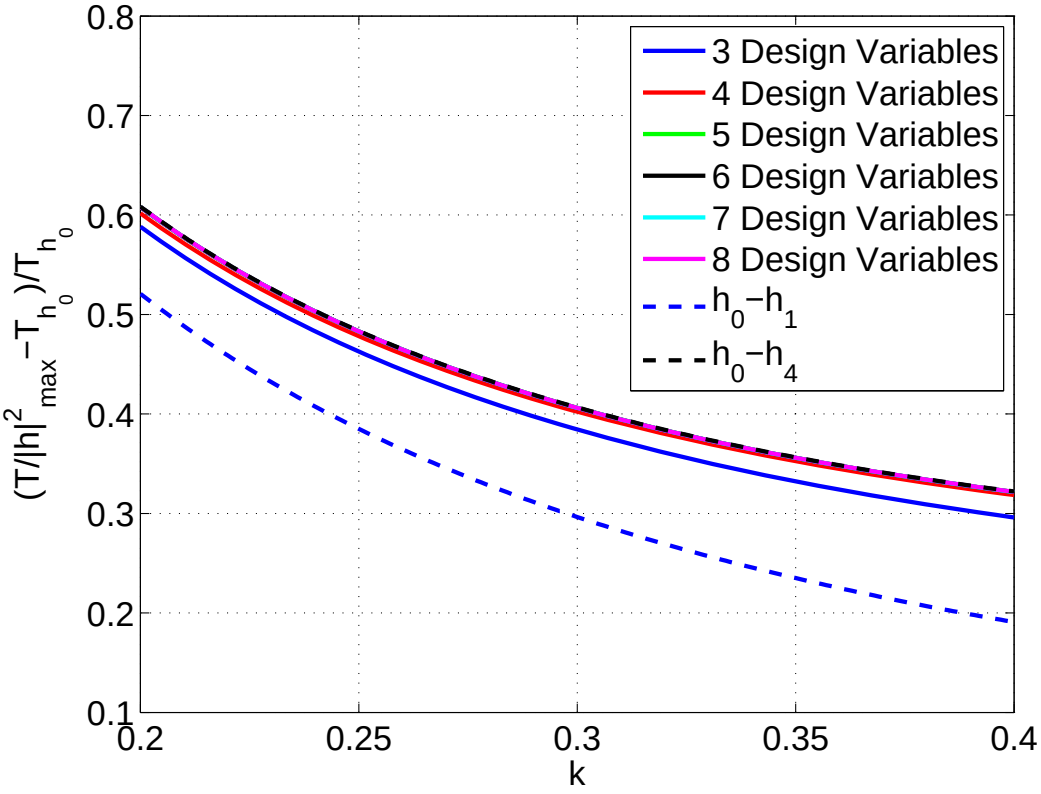

Figure 8.19: Maximum Thrust ($\sigma = 40$)

8.3 Aeroelastic Tailoring for Maximum Normalized Thrust and Propulsive Efficiency

The maximum stroke-averaged thrust that can be produced by a deformable membrane wing occurs at a propulsive efficiency of around 50% as seen in Figures Figures 8.20 through 8.22. In MAV flight a higher efficiency is desired. As with the aerodynamic optimization, a Pareto front for the coefficient of stroke-averaged, C_T, thrust and propulsive efficiency, η, can be generated. Thus the maximum stroke-averaged thrust at various values of efficiency can be determined. Figures 8.20 through 8.22 show Pareto fronts for the multi-objective aeroelastic optimization of stroke-averaged thrust and propulsive efficiency. Results are shown for the bird flight regime; a mass ratio of $\sigma = 40$ and the lower bound, upper bound and average reduced frequency, $k = 0.2$, $k = 0.4$ and $k = 0.3$ respectively. The aerodynamic optimization for rigid body motion and three degrees of freedom of deformation are also shown.

It can be seen at all three values of reduced frequency that there is significant improvement in maximum stroke-averaged thrust with only one tension variable at lower values of propulsive efficiency ($50\% - 65\%$). Allowing the tension in the spanwise and chordwise directions to be different values (two tension variables) results in a stroke-averaged thrust very close to the aerodynamic optimum at lower values of propulsive efficiency.

At higher values of propulsive efficiency it can be seen that there is some improvement over the rigid body optimization by allowing the wing to deform with one tension variable. Increasing the the design space further results in a very small increase in stroke-averaged thrust. This shows that designing the wing with just two tension variables yields a result close to the maximum achievable stroke-averaged thrust and a far more general structure with six tension variables may not be needed.

It is likely that the current aeroelastic system, when being constrained to have such a high value of propulsive efficiency cannot yield a stroke-averaged thrust much higher than the rigid body optimum. The design is based on passive deformation and thus large thrust at high efficiencies may be unobtainable.

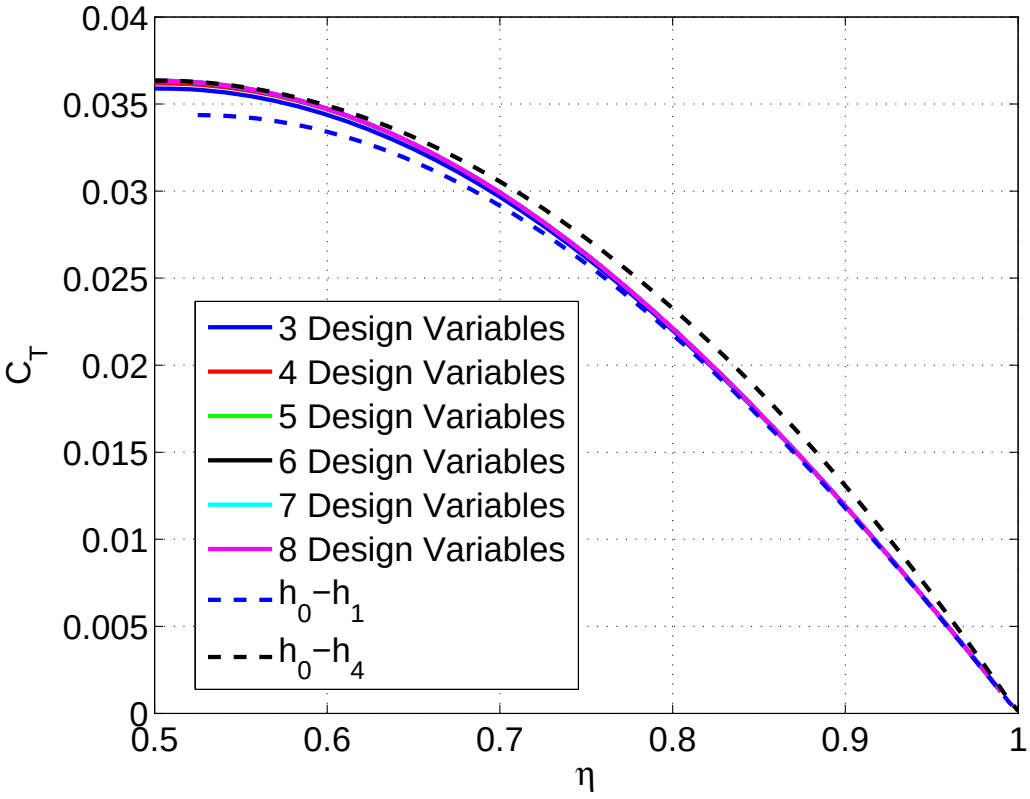

Figure 8.20: Pareto front ($k = 0.2$ and $\sigma = 40$)

The design of a flapping membrane wing that produces maximum stroke-averaged thrust is useful, however higher propulsive efficiency is also desired. Another way of looking at these results is seeing how the maximum thrust changes as a function of frequency for various values of propulsive efficiency. Figures 8.23 and 8.24 show the fractional improvement of maximum stroke-averaged thrust over plunging for situations where the propulsive efficiency is restricted to 60% and 70% respectively. Note that thrust due to plunging occurs at one value of efficiency which is dependent on the reduced frequency. Results are presented in this manner to show that situations exist where constraining the propulsive efficiency to be so high results in a maximum stroke-averaged thrust that is lower than thrust due to plunging.

It can be seen from Figure 8.23 that allowing the wing to deform with just one tension variable makes it capable of producing over half the aerodynamic optimum at 60% efficiency.

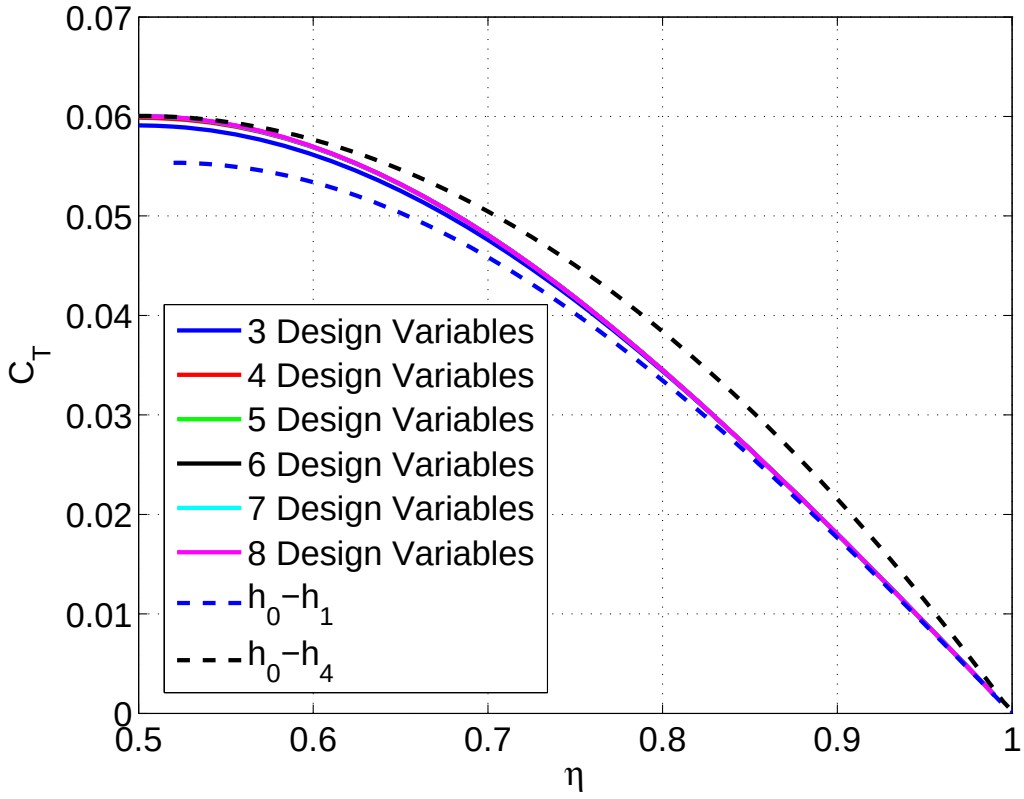

Figure 8.21: Pareto front ($k = 0.3$ and $\sigma = 40$)

Allowing the tension to take a more general form continues to increase the maximum stroke-averaged thrust to within 95% of the aerodynamic optimum, which was also seen in Figures 8.20 through 8.22.

Figure 8.24 shows similar results for a case when the propulsive efficiency is constrained to be 70%. However at the higher values of propulsive efficiency, a larger design space is needed to obtain a maximum stroke-averaged thrust close to the aerodynamic optimum. At this value of propulsive efficiency, the maximum possible stroke-averaged thrust with the full design space is not as close to the aerodynamic optimum as with 60% efficiency. This is expected from observation of the Pareto fronts. In both figures, the five variable optimum (green line) gives very little improvement over the four variable optimum (red line). The difference is so small that it cannot be seen on the figure; the green line simply covers

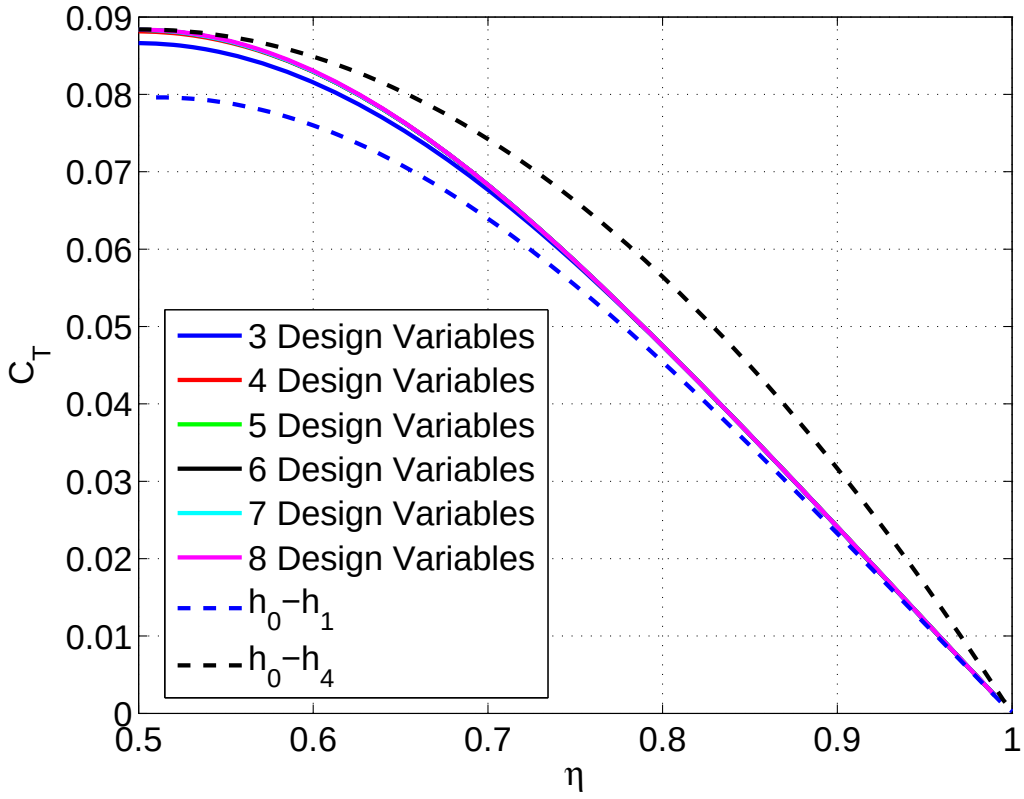

Figure 8.22: Pareto front ($k = 0.4$ and $\sigma = 40$)

the red line. Constraining the efficiency to be higher results in situations where the maximum stroke-averaged thrust is less than thrust due to plunging. However, this does show that a plunging membrane wing can not only be tailored to increase the thrust producing capability, but also be tailored to increase the efficiency while maintaining the same amount of thrust as plunging.

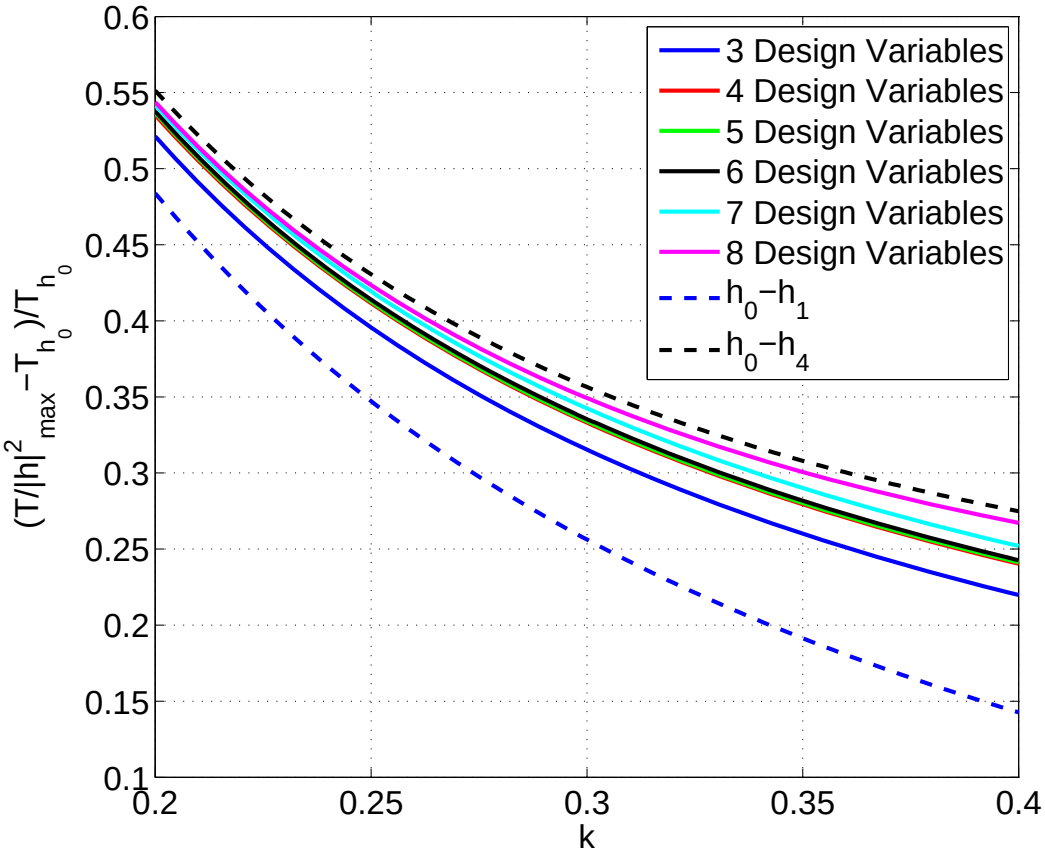

Figure 8.23: Maximum thrust at 60% Efficiency ($\sigma = 40$)

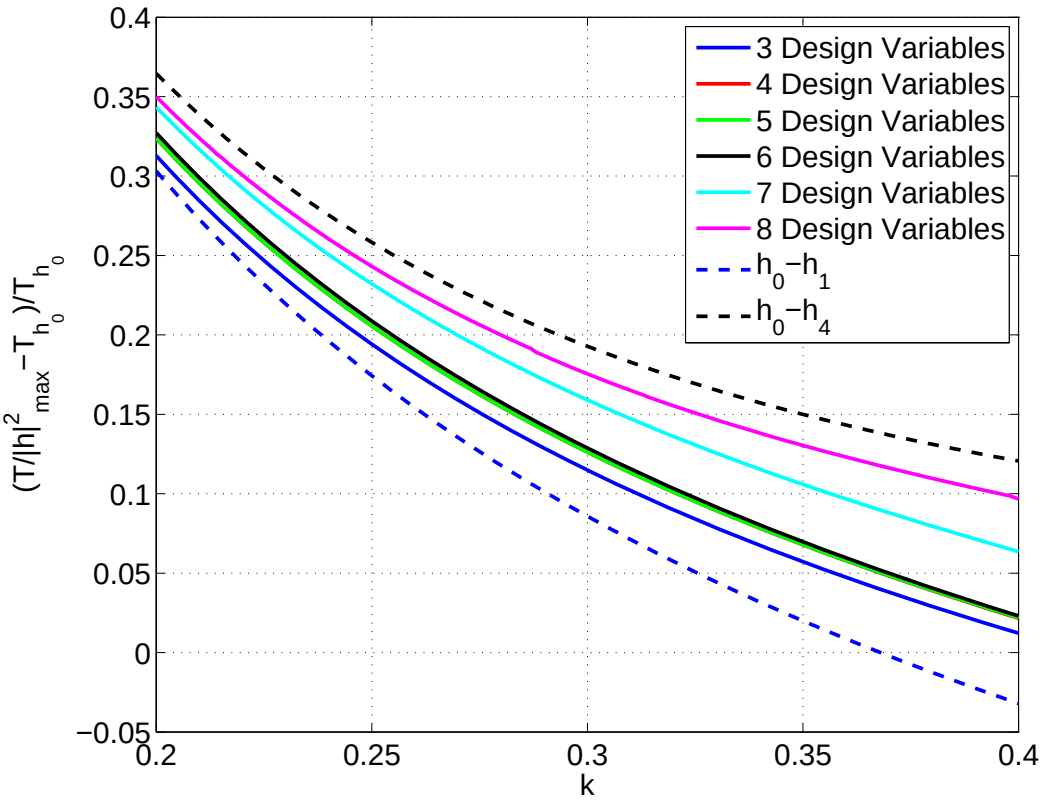

Figure 8.24: Maximum thrust at 70% Efficiency ($\sigma = 40$)

8.4 Optimal Design for Various Cases

The maximum stroke-averaged thrust and propulsive efficiency for MAV membrane wings operating in the regime of bird flight have been found and presented. This section shows the design of the structure required to achieve these optimal flight characteristics. The optimal membrane design for six tension variables and two pitch variables is shown for the lower bound, average, and upper bound reduced frequencies of the bird flight regime at the average mass ratio of $\sigma = 40$. These results are shown for the maximum thrust case as well as the maximum thrust at 60% and 70% efficiency. Higher propulsive efficiencies are not considered because maximum stroke-averaged thrust is low at high propulsive efficiency. As stated previously, the effect of mass ratio on the optimum is quite small and so bird wings outside of the average will have very similar solutions.

Figures 8.25 through 8.27 show spanwise tension function for the full design space at conditions for maximum stroke-averaged thrust, 60% efficiency and 70% efficiency. Results are presented for the lower bound, average and upper bound reduced frequencies of bird flight, $k = 0.2$, $k = 0.3$ and $k = 0.4$. The chordwise tension is given in the legend.

The figures show the nondimesnional spanwise tension multiplied by the mass ratio and square of the reduced frequency. This was done for comparison purposes because the nondimensional tension terms contain σk^2 in the denominator. As expected the tension for the optimal design grows larger with reduced frequency. Faster oscillation will result in larger apparent mass terms and thus a larger tension is required to maintain a unit deformation. The shapes of the spanwise tension function for maximum stroke-averaged thrust and maximum stroke-averaged thrust at 60% efficiency look nearly the same, however they are sligtly different. Furthermore, it appears that the spanwise tension constraint is active. Further inspection of the plots show that the constraint is actually inactive. The spanwise tension at the trailing edge for these cases is on the order 1e-1. The constraint tolerance chosen during optimzation was 1e-10, thus the solution is converged to an optimum without an active inequality. However, it can be seen that the chordwise tension constraint is active for the maximum thrust case at a reduced frequency of $k = 0.4$.

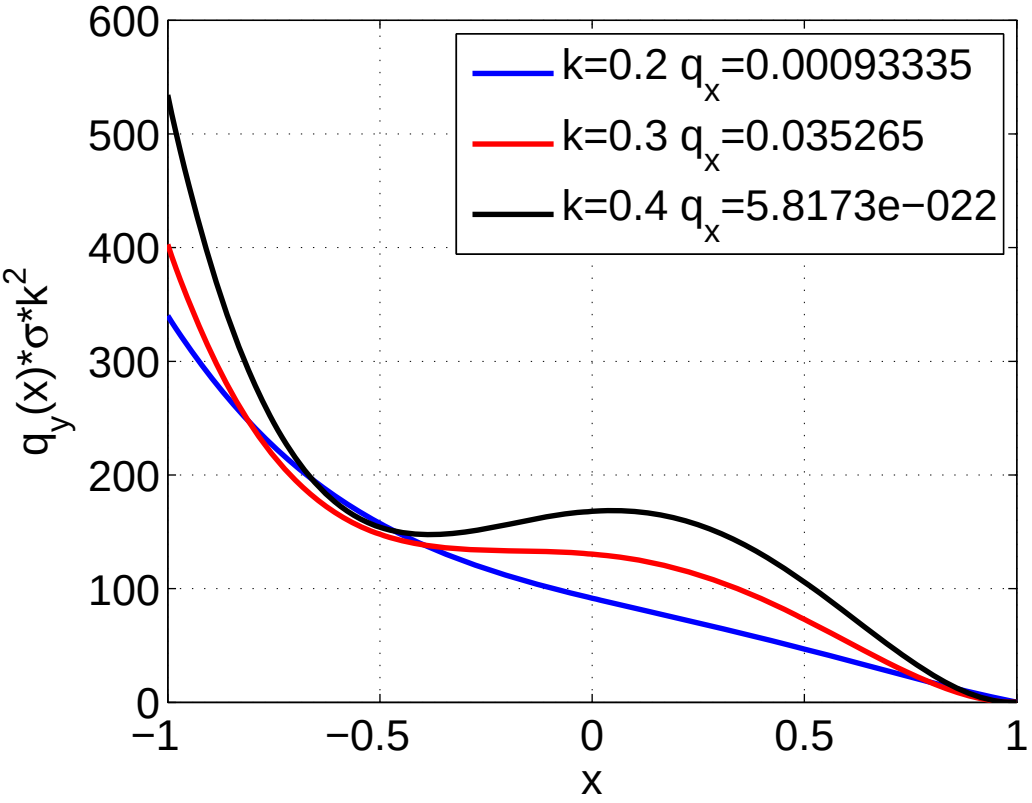

Figure 8.25: Spanwise tension for maximum thrust $\sigma = 40$

The optimal design for maximum stroke-averaged thrust at 70% efficiency looks quite different than the design for maximum thrust and 60% efficiency. Investigation of the results has shown that multiple local optima exist for this system and the use of gradient based optimization is not guaranteed to give the global optimum. It appears that the optimal design found for 70% efficiency has either jumped to a different, still feasible, solution or the optimal peak which existed for lower efficiencies does not exist for such high efficiencies. In other words the efficiency constraint may have removed that local maximum from the feasible domain. The optimization for these points was conducted by using the solution from one less design variable, making the additional variable zero, and using the solution from a lower value of efficiency where the solution in the form of 60% efficiency exists. Both optimizations yield the same solution at 70%, thus showing the most likely reason for the change in spanwise tension is that the maximum that existed at lower efficiencies is non

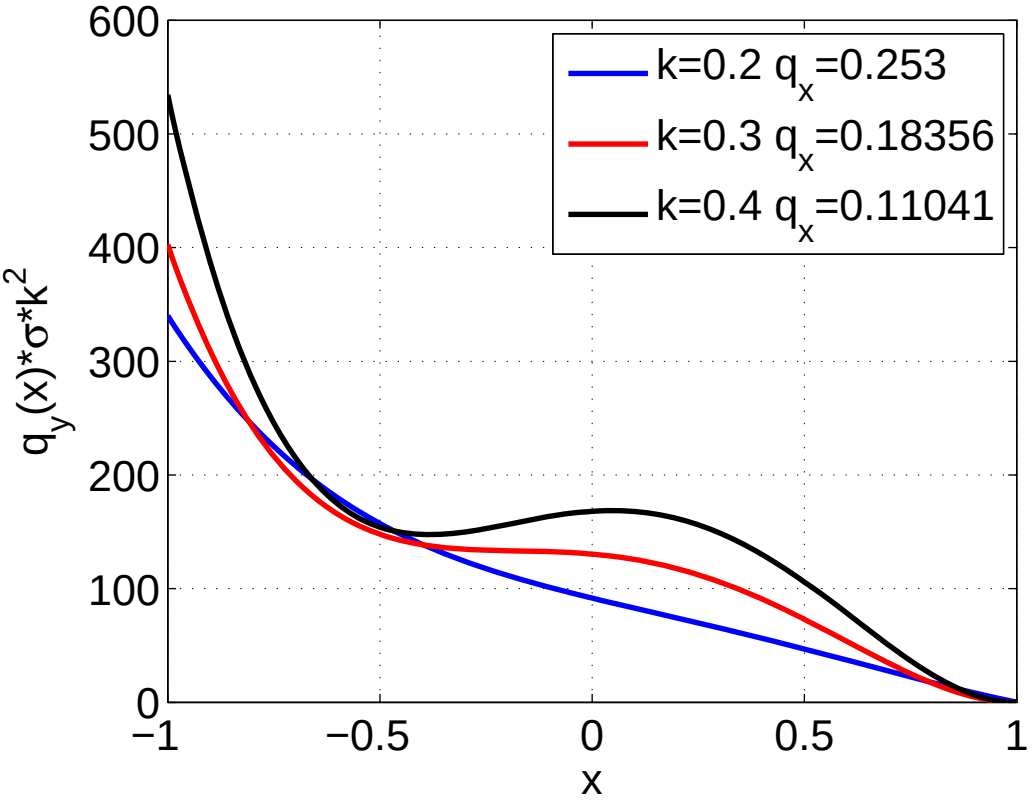

Figure 8.26: Spanwise tension for maximum thrust at 60% efficiency $\sigma = 40$

existent in higher efficiencies.

The cases for maximum stroke-averaged thrust and thrust at 60% efficiency show that the optimal design has a tight leading edge and looser trailing edge. The thrust optimization results for a plunging (not pitching) show the opposite. It was shown that a plunging wing with no bound on the magnitude of motion requires a tight trailing edge and loose leading edge. This allows more deformation at the leading edge directing the pressure toward the thrust direction. Situations where pitch is included and the magnitude of the motion is

k	0.2	0.3	0.4
Maximum Thrust	0.2251	0.2835	0.3288
Thrust at $\eta = 0.6$	0.1523	0.1861	0.2188
Thrust at $\eta = 0.7$	0.0990	0.1458	0.2022

Table 8.2: Magnitude of pitching for optimal design

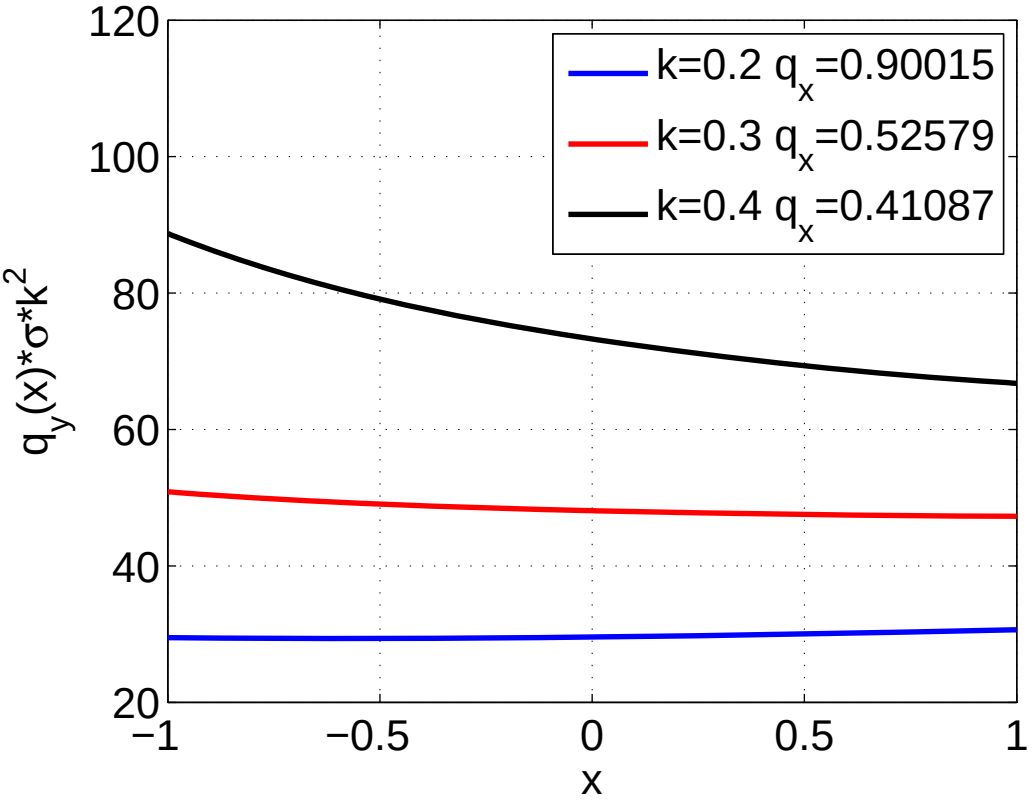

Figure 8.27: Spanwise tension for maximum thrust at 70% efficiency $\sigma = 40$

constrained, as with the normalized thrust optimization here, the optimal design is different. As verification, the maximum stroke-averaged thrust shape was compared to the aerodynamic optimal shape, showing very little difference. This further shows that tailoring the structure with six tension variables yields almost all of the thrust possible.

Tables 8.2 and 8.3 show the magnitude and phase of pitching for these optimal designs. It can be seen that pitch has a significant contribution to the motion, more so in the case of maximum thrust. The optimal design at higher efficiencies requires a smaller contribution

k	0.2	0.3	0.4
Maximum Thrust	51.7	45.2	40.1
Thrust at $\eta = 0.6$	44.2	26.8	13.2
Thrust at $\eta = 0.7$	15.2	-15.4	-33.2

Table 8.3: Phase of pitching in degrees for optimal design

from pitch. The magnitude of pitch also increases as reduced frequency increases while the phase of pitch required decreases. This change is due to the effect of Theodorsen's function shifting the phase of thrust relative to the motion as reduced frequency changes.

The results shown in Figures 8.25 through 8.27 and Tables 8.2 and 8.3 present the optimal design for a flapping membrane wing to generate maximum stroke-averaged thrust and thrust at 60% and 70% propulsive efficiency at various reduced frequencies in the bird flight regime. However, as shown in the first two sections, much of the acheivable stroke-averaged thrust can be obtained with a simple one or two tension variable design. Therefore it is worth presenting some cases for these results. Tables 8.4 through 8.6 present the magnitude and phase of pitching and the tension (both spanwise and chordwise) required for an optimal three variable design. The same cases presented for eight variables are shown. Tables 8.7 through 8.10 present the magnitude and phase of pitching and the spanwise and chordwise tension required for an optimal four variable design.

k	0.2	0.3	0.4
Maximum Thrust	0.1973	0.2502	0.2923
Thrust at $\eta = 0.6$	0.1262	0.1532	0.1850
Thrust at $\eta = 0.7$	0.0565	0.1111	0.1776

Table 8.4: Magnitude of pitching for 3 variable optimal design

k	0.2	0.3	0.4
Maximum Thrust	62.8	51.1	43.5
Thrust at $\eta = 0.6$	56.7	32.3	15.3
Thrust at $\eta = 0.7$	23.0	-20.4	-36.6

Table 8.5: Phase of pitching in degrees for 3 variable optimal design

k	0.2	0.3	0.4
Maximum Thrust	3.9394	2.6201	2.1097
Thrust at $\eta = 0.6$	4.6209	2.9899	2.3661
Thrust at $\eta = 0.7$	5.5740	3.4284	2.6470

Table 8.6: Nondimensional tension (spanwise and chordwise) for 3 variable optimal design

The contribution of pitch in the three variable case shows a similar trend to the eight variable case. The magnitude of pitch required is larger at higher reduced frequencies and lower at higher efficiencies. The phase of pitch relative to plunge decreases as frequency increases and efficiency increases. The tension is constant and is the same value in both spanwise and chordwise directions. The tension required for an optimal design is larger at higher efficiencies and decreases as reduced frequency increases.

The Pareto fronts showed that most of the thrust can be generated with four design variables, meaning the additional tension terms lead to little additional improvement. This can be seen in Tables 8.7 and 8.8 which show the magnitude and phase of pitching. These results are the same as the pitching results for the eight variable optimum design implying that minor improvements in maximum thrust are achieved only by tailoring the tension. Again, this is not unexpected since the Pareto fronts are nearly the same. The addition of the tension variable, allowing tension to be different in spanwise and chordwise directions, leads to the optimum design having a very small chordwise tension and a large spanwise tension, showing that the spanwise tension has a more significant effect on the thrust than the chordwise tension.

k	0.2	0.3	0.4
Maximum Thrust	0.2251	0.2835	0.3288
Thrust at $\eta = 0.6$	0.1523	0.1861	0.2188
Thrust at $\eta = 0.7$	0.0990	0.1458	0.2022

Table 8.7: Magnitude of pitching in degrees for 4 variable optimal design

k	0.2	0.3	0.4
Maximum Thrust	51.7	45.2	40.1
Thrust at $\eta = 0.6$	44.2	26.8	13.2
Thrust at $\eta = 0.7$	15.2	-15.4	-33.2

Table 8.8: Phase of pitching in degrees for 4 variable optimal design

k	0.2	0.3	0.4
Maximum Thrust	0.0009	0.0353	0
Thrust at $\eta = 0.6$	0.2530	0.1836	0.1104
Thrust at $\eta = 0.7$	0.9001	0.5258	0.4109

Table 8.9: Nondimensional chordwise tension for 4 variable optimal design

k	0.2	0.3	0.4
Maximum Thrust	57.28	36.20	26.24
Thrust at $\eta = 0.6$	57.30	36.21	26.25
Thrust at $\eta = 0.7$	18.49	13.36	11.45

Table 8.10: Nondimensional spanwise tension for 4 variable optimal design

Chapter 9

Conclusions and Future Work

9.1 Conclusions

Optimization of the aerodynamic and aeroelastic systems of a deformable wing for stroke-averaged thrust and thrust efficiency has been addressed. Optimization of the aerodynamic system showed that maximum stroke-averaged thrust can be calculated for a given amplitude of motion and deformation. The maximum stroke-averaged thrust increases if we expand the design space with more deformation shapes.

A Pareto front for stroke-averaged thrust and propulsive efficiency was generated using the ϵ-constraint method. It was shown that adding higher order deformation shapes to the design space leads to an increase in the maximum stroke-averaged thrust for a given efficiency and increase of efficiency for a given stroke-averaged thrust. At high reduced frequencies, the Pareto fronts become like a bell shape, thus leading to very low maximum stroke-averaged thrust, at high efficiencies.

A constraint for zero leading edge suction was investigated. This allowed for the maximum stroke-averaged thrust and efficiency to be found for a case where there was no leading edge suction. It was shown that using this constraint forced the pressure difference to be zero at the leading edge of the airfoil, ensuring no leading edge separation. Maximum stroke-averaged thrust with this constraint was found to be smaller than, but on the order

of the stroke-averaged thrust without the constraint.

The use of a magnitude of motion/deformation constraint and a leading edge suction constraint gives results for flow which satisfies the assumptions used to derive the deformable thin airfoil theory. This provides detailed airfoil shapes required to generate maximum stroke-averaged thrust and efficiency for flapping wings without the use of CFD.

Optimization of the aeroelastic system was also investigated. The aeroelastic equations of motion for a membrane wing undergoing prescribed rigid body motions are derived. The spanwise deformation was represented using a single shape reducing the two dimensional membrane problem to a one dimensional form. Optimization of the aeroelastic system for one and three degrees of freedom was presented with divergence and tension constraints. Results were presented for various reduced frequencies and mass ratios. It was shown that the stiffness of a flexible membrane wing undergoing unit harmonic plunging can be tailored to maximize stroke-averaged thrust. For all cases considered, there is a range of stiffness for which the flexible wing produces higher thrust as compared to rigid plunging wing.

Maximum thrust for a one, two, and three design variable system was presented. Increasing the design space by allowing the tension to be defined in a more general form always leads to a larger value of maximum thrust. The case of a linear variation of tension yields an optimum that has the lowest spanwise tension at the leading edge. This results in the deformation which points the pressure vector more toward the free stream, thus increasing the thrust. Larger values of mass ratio led to larger values of thrust at all reduced frequency for every design space investigated.

The maximum thrust for every scenario approaches infinity at some value of reduced frequency. Further investigation into the results showed that the magnitude of the deformation was also approaching infinity; and the thrust per unit deformation was approaching zero. Very large deformations violate the assumption that the wing is undergoing small disturbances. It was further shown that the reason for the large deformation is that the optimization gave results which were approaching conditions for flutter, leading to large deformation. Therefore the motion needed to be constrained or the objective function needed

to be modified.

The objective was modified to normalized stroke-averaged thrust. It was shown that allowing a flapping wing to deform using only one structural design variable results in a structure that can be tailored to have a larger thrust than a rigid wing. Allowing the membrane tension to take a more general form resulted in higher thrust, as expected. Furthermore, using only two tension variables (different spanwise and chordwise tension) resulted in a tailored structure that could obtain most of the thrust from the design with six tension variables. Optimizing with six structural design variables along with the magnitude and phase of pitch yielded a maximum thrust very close to the aerodynamic optimization for five Chebychev shapes (plunge, pitch, and three deformation mode shapes); the best the wing can perform.

Multi-objective optimization of stroke-averaged thrust per unit span and propulsive efficiency was performed at various reduced frequencies and mass ratios. As with the aerodynamic optimization, allowing the wing to deform results in a larger maximum thrust at all values of efficiency, as expected. Furthermore, increasing the number of structural variables increases the maximum thrust very close to the best solution (the aerodynamic optimization).

The optimal design was presented for various cases at the lower bound, upper bound and average reduced frequencies in the bird flight regime. Spanwise tension functions required to generate maximum stroke-averaged thrust at various efficiencies were presented. Also, constant tension designs (three and four variables) were shown. It was seen that pitch has a large contribution to the optimal designs and the higher order tension shapes have a smaller contribution.

The theory and design results presented give the detailed design of a flapping membrane wing required to generated maximum stroke-averaged thrust at various efficiencies for flapping wing MAV's. These results can easily be implemented into a flapping wing MAV design to increase overall performance and will be extremely helpful in the future of MAV design.

9.2 Future Work

Optimization of the aerodynamic and aeroelastic systems has been performed. The aerodynamic optimization has shown the deformation required to generate maximum thrust and the aeroelastic optimization has shown how to tailor the membrane wing to achieve maximum thrust. However the aeroelastic optimization has far more potential for improvement. A combination of global (genetic algorithm) and gradient-based constrained optimization has been used to find local optima. However it has been shown that the there are many local maxima and converging the global optimum and Pareto optimum for the multi-objective optimization is not guaranteed. Further investigation of the optimization techniques will be useful in future aeroelastic tailoring.

The aeroelastic optimization design space consisted of only a constant chordwise tension and a varying spanwise tension. Furthermore, only a three degree of freedom membrane model was used, with only one spanwise degree of freedom. The aeroelastic model has room for further improvement and the design space could consist of many other terms. For example, the membrane material has not been considered. The density and thickness of the membrane could be constant or vary along the chord and span. Furthermore, the shape of the wing has not been considered. This opens up the possibility of other design constraints, such as manufacturing.

Bibliography

[1] Theodorsen, T., "General Theory of Aerodynamic Instability and the Mechanism of Flutter," NACA TR No. 496, May 1934.

[2] Garrick, I. E., "Propulsion of a Flapping and Oscillating Airfoil," NACA TR No. 567, May 1936.

[3] Peters, D. A., Hsieh, M.-C. A., and Torrero, A., "A state-space airloads theory for flexible airfoils," *Annual Forum Proceedings - AHS International*, Vol. III, Phoenix, AZ, United states, 2006, pp. 1806 – 1823.

[4] Peters, D., "Two-dimensional incompressible unsteady airfoil theory-An overview," *Journal of Fluids and Structures*, Vol. 24, No. 3, 2008, pp. 295 – 312.

[5] Walker, W. P. and Patil, M. J., "Unsteady Aerodynamics of Deformable Thin Airfoils," No. AIAA-2010-322, 48th AIAA Aerospace Sciences Meeting Including the New Horizons Forum and Aerospace Exposition, Orlando, Florida, Jan. 4-7 2010.

[6] von Kármán, T. and Burgers, J. M., *General Aerodynamic Theory-Perfect Fluids*, Vol. II, Julius Springer, Berlin, 1935.

[7] Wagner, H., "Über die Entstehung des dynamischen Auftriebes von Tragflügeln," February 1925, pp. 17–35.

[8] Küssner, H. G., "Zusammenfassender Bericht über den instationaren Auftrieb von Flügeln," December 1936, pp. 410–424.

[9] Garrick, I. E., "On Some Reciprical Relations in the Theory of Nonstationary Flows," NACA TR No. 629, March 1938.

[10] von Kármán and Sears, "Airfoil Theory for Non-Uniform Motion," *Journal of the Aeronautical Sciences*, Vol. 5, No. 10, 1938, pp. 379–390.

[11] Sears, W. R., "Operational Methods in the Theory of Airfoils in Non-Uniform Motion," *Journal of the Franklin Institute*, Vol. 230, July 1940, pp. 95–111.

[12] Isaacs, R., "Airfoil Theory for Flows of Variable Velocity," *Journal of the Aeronautical Sciences*, Vol. 12, No. 1, 1945, pp. 113–117.

[13] Isaacs, R., "Airfoil Theory for Rotary Wing Aircraft," *Journal of the Aeronautical Sciences*, Vol. 13, No. 4, 1946, pp. 218–220.

[14] Loewy, R., "A Two-Dimensional Approximation to the Unsteady Aerodynamics of Rotary Wings," *Journal of the Aeronautical Sciences*, Vol. 24, No. 2, February 1957, pp. 81–92.

[15] Greenberg, J. M., "Airfoil in Sinusoidal Motion in a Pulsating Stream," NACA TN No. 1326, June 1947.

[16] Zbikowski, R., "On aerodynamic modelling of an insect-like flapping wing in hover for micro air vehicles," *Philosophical Transactions of the Royal Society London, Series A (Mathematical, Physical and Engineering Sciences)*, Vol. 360, No. 1791, 2002/02/15, pp. 273 – 90.

[17] Azuma, A. and Okamoto, M., "Theoretical Study of the Two-dimensional Aerodynamic Charecteristics of Unsteady Wings," *Journal of Theoretical Biology*, Vol. 234, No. 1, May 2005, pp. 67–78.

[18] Patil, M. J., "From fluttering wings to flapping flight: The energy connection," *Journal of Aircraft*, Vol. 40, No. 2, 2003, pp. 270 – 276.

[19] Ansari, S. A., Zbikowski, R., and Knowles, K., "Non-linear unsteady aerodynamic model for insect-like flapping wings in hover. Part 1: methodology and analysis," *Journal of Aerospace Engineering*, Vol. 220, 2006, pp. 61–83.

[20] Ansari, S. A., Zbikowski, R., and Knowles, K., "Non-linear unsteady aerodynamic model for insect-like flapping wings in hover. Part 2: implementation and validation," *Journal of Aerospace Engineering*, Vol. 220, 2006, pp. 169–186.

[21] Peters, D. A., Karunamoorthy, S., and Cao, W., "Finite state induced flow models. I - Two-dimensional thin airfoil," *Journal of Aircraft*, Vol. 32, No. 2, 1995, pp. 313–322.

[22] Peters, D. A. and He, C. J., "Finite state induced flow models. II - Three-dimensional rotor disk," *Journal of Aircraft*, Vol. 32, No. 2, 1995, pp. 323–333.

[23] Johnston, C. O., Mason, W. H., and Han, C., "Unsteady thin airfoil theory revisited for a general deforming airfoil," *Journal of Mechanical Science and Technology*, Vol. 24, No. 12, 2010, pp. 2451–2460.

[24] Mateescu, D. and Abdo, M., "Theoretical Solutions for Unsteady Flows Past Oscillating Flexible Airfoils Using Velocity Singularities," *Journal of Aircraft*, Vol. 40, 2003, pp. 153–163.

[25] Glegg, S. and Devenport, W., "Unsteady loading on an airfoil of arbitrary thickness," *Journal of Sound and Vibration*, Vol. 319, No. 3-5, 2009, pp. 1252 – 70.

[26] Jones, R. T., "The Unsteady Lift of a Wing of Finite Aspect Ratio," NACA TR No. 681, June 1939.

[27] Hernandes, F. and Soviero, P. A. D. O., "A numerical model for thin airfoils in unsteady compressible arbitrary motion," *Journal of the Brazilian Society of Mechanical Sciences and Engineering*, Vol. 29, No. 3, 2007, pp. 253 – 261.

[28] Anderson, J. M., Streitlien, K., Barrett, D. S., and Triantafyllou, M. S., "Oscillating foils of high propulsive efficiency," *Journal of Fluid Mechanics*, Vol. 360, 1998, pp. 41–72.

[29] Heathcote, S. and Gursul, I., "Flexible Flapping Airfoil Propulsion at Low Reynolds Numbers," *AIAA Journal*, Vol. 45, No. 5, May 2007, pp. 1066–1079.

[30] Tuncer, I. H. and Kaya, M., "Optimization of Flapping Airfoils for Maximum Thrust and Propulsive Efficiency," *AIAA Journal*, Vol. 43, No. 11, November 2005, pp. 2329–2336.

[31] Lee, B. J. and Liou, M. S., "Shape and Trajectory Optimization of Flapping Airfoil," No. AIAA 2010-2760, 51st AIAA/ASME/ASCE/AHS/ASC Structures, Structural Dynamics, and Materials Conference, Orlando, Florida, April 12 - 15 2010.

[32] Lee, B. J., Padulo, M., and Liou, M.-S., "Non-sinusoidal Trajectory Optimization of Flapping Airfoil using Unsteady Adjoint Approach," No. AIAA 2011-1312, 49th AIAA Aerospace Sciences Meeting Including the New Horizons Forum and Aerospace Exposition, Orlando, Florida, 2011.

[33] Murua, J., Palacios, R., and Peiró, J., "Camber Effects in the Dynamic Aeroelasticity of Compliant Airfoils," *Journal of Fluids and Structures*, Vol. 26, 2010, pp. 527–543.

[34] Knight, J., Lucey, A., and Shaw, C., "Fluid-Structure Interaction of a Two-Dimensional Membrane in a Flow with a Pressure Gradient with Application to Convertible Car Roofs," *Journal of Wing Engineering and Industrial Aerodynamics*, Vol. 98, 2010, pp. 65–72.

[35] LaBryer, A. R. and Attar, P. J., "Modeling of the Nonlinear Structural Dynamics of a Plunging Membrane Airfoil Using a High Dimensional Balance Approach," No. AIAA 2009-2474, 50th AIAA/ASME/ASCE/AHS/ASC Structures, Structural Dynamics, and Materials Conference, Palm Springs, CA, April 2009.

[36] Gaunaa, M., "Unsteady 2D Potential-flow Forces on a Thin Variable Geometry Airfoil Undergoing Arbitrary Motion," Tech. rep., Risø National Laboratory, 2006.

[37] Sears, W. R., "Some Aspects of Non-Stationary Airfoil Theory and Its Practical Application," *Journal of the Aeronautical Sciences*, Vol. 8, No. 3, 1941, pp. 104–108.

[38] Lian, Y. and Shyy, W., "Numerical Simulations of Membrane Wing Aerodynamics for Micro Air Vehicle Applications," *Journal of Aircraft*, Vol. 42, No. 4, 2005, pp. 865–873.

[39] Banerjee, S. P. and Patil, M. J., "Aeroelastic Analysis of Membrane Wings," No. AIAA 2008-1812, 49th AIAA/ASME/ASCE/AHS/ASC Structures, Structural Dynamics, and Materials Conference, Schaumburg, IL, April 7-10 2008.

[40] Grishanina, T. V. and Shklyarchuk, F. N., "Unsteady Oscillation of a Deformable Airfoil Section in Incompressible Flow," *Russian Aeronautics*, Vol. 52, No. 2, 2009, pp. 129–137.

[41] Berci, M., Toropov, V. V., Hewson, R. W., and Gaskell, P. H., "Aeroelastic Analysis and Gust Response of a Flexible Airfoil," No. AIAA 2010-3119, 51st AIAA/ASME/ASCE/AHS/ASC Structures, Structural Dynamics, and Materials Conference, Orlando, Florida, April 12-15 2010.

[42] Greenhalgh, S., Curtiss, H. C. J., and Smith, B., "Aerodynamic Properties of a Two-Dimensional Inextensible Flexible Airfoil," *AIAA Journal*, Vol. 22, No. 7, 1984.

[43] Gulcat, U., "Propulsive Force of a Flexible Flapping Thin Airfoil," *Journal of Aircraft*, Vol. 46, No. 2, 2009, pp. 465–473.

[44] Smith, R. and Shyy, W., "Computational Model of Flexible Membrane Wings in Steady Laminar Flow," *AIAA Journal*, Vol. 33, No. 10, 1995, pp. 1769–1777.

[45] Pederzani, J. and Haj-Hariri, H., "Numerical Analysis of Heaving Flexible Airfoils in a Viscous Flow," *AIAA Journal*, Vol. 44, No. 11, 2006, pp. 2773–2779.

[46] Shyy, W., Klevebring, F., Nilsson, M., Sloan, J., Carroll, B., and Fuentes, C., "Rigid and Flexible Low Reynolds Number Airfoils," *Journal of Aircraft*, Vol. 36, No. 3, 1999, pp. 523–529.

[47] Shyy, W. and Smith, R., "A Study of Flexible Airfoil Aerodynamics with Application to Micro Aerial Vehicles," No. AIAA-97-1933, 1997.

[48] Kaya, M., Tuncer, I. H., Jones, K. D., and Platzer, M. F., "Optimization of Aeroelastic Flapping Motion of Thin Airfoils in a Biplane Configuration for Maximum Thrust," Vol. AIAA 2007-4340, 37th AIAA Fluid Dynamics Conference and Exhibit, Miami, Florida, June 25-28 2007.

[49] Kaya, M., Tuncer, I. H., Jones, K. D., and Platzer, M. F., "Optimization of Flapping Motion of Airfoils in Biplane Configuration for Maximum Thrust and/or Efficiency," Vol. AIAA 2007-434, 37th AIAA Fluid Dynamics Conference and Exhibit, Miami, FL, June 25 - 28 2007.

[50] Stanford, B. and Beran, P., "Formulation of Analytical Design Derivatives for Nonlinear Unsteady Aeroelasticity," *AIAA Journal*, Vol. 49, No. 3, 2011, pp. 598–610.

[51] Maute, K., Nikbay, M., and Farhat, C., "Coupled Analytical Sensitivity Analysis and Optimization of Three-Dimensional Nonlinear Aeroelastic Systems," *AIAA Journal*, Vol. 39, No. 11, 2001, pp. 2051–2061.

[52] Lian, Y., Shyy, W., and Haftka, R., "Shape Optimization of a Membrane Wing for Micro Air Vehicles," Vol. AIAA 2003-106, 41st Aerospace Sciences Meeting and Exhibit, January 6-9 2003.

[53] Nikbay, M., Levent, O., and Aysan, A., "Multidisciplinary Code Coupling for Analysis and Optimization of Aeroelasic Systems," *Journal of Aircraft*, Vol. 46, No. 6, 2009, pp. 1938–19444.

[54] Bisplinghoff, R., A. H. and Halfman, R., *Aeroelasticity*, Addison-Wesley, 1955.

[55] Katz, J. and Plotkin, A., *Low-Speed Aerodynamics*, Cambridge University Press, 2002.

[56] Shyy, W., Lian, Y., Tang, J., Viieru, D., and Liu, H., *Aerodynamics of Low Reynolds Number Flyers*, Cambridge University Press, 2008.

[57] Haftka, R. T. and Gürdal, Z., *Elements of Structural Optimization*, Kluwer Academic Publishers, 1992.

[58] Van Den Berg, C. and Rayner, J. M., "The Moment of Inertia of Bird Wings and the Insertial Power Requirement for Flapping Flight," *Journal of Experimental Biology*, Vol. 198, 1993, pp. 1655–1664.